DEVELOPING OF INERTIAL-MEASUREMENT-UNIT-BASED TRAJECTORY RECONSTRUCTION ALGORITHM FOR STUDYING PNEUMATIC CONVEYING

by

Zibo Wang

B.S. in Mechanical Engineering, East China University of Science and Technology, China, 2016

Submitted to the Graduate Faculty of

Swanson School of Engineering in partial fulfillment

of the requirements for the degree of

Master of Science in Mechanical Engineering

University of Pittsburgh

2018

UNIVERSITY OF PITTSBURGH

SWANSON SCHOOL OF ENGINEERING

This thesis was presented

by

Zibo Wang

It was defended on

July 13, 2018

and approved by

George E. Klinzing, Ph.D., Professor
Department of Chemical &Petroleum Engineering

Jeffrey S. Vipperman, Ph.D., Assistant Professor
Department of Mechanical Engineering & Materials Science

Thesis Advisor: William W. Clark, Ph.D., Professor
Department of Mechanical Engineering & Materials Science

DEVELOPING OF INERTIAL-MEASUREMENT-UNIT-BASED TRAJECTORY RECONSTRUCTION ALGORITHM FOR STUDYING PNEUMATIC CONVEYING

Zibo Wang, M.S.

University of Pittsburgh, 2018

Numerically simulating granular materials' dynamics during pneumatic conveying is a great challenge for today's researchers. Existing mathematical models of granular flow have limitations that make it difficult to obtain good agreement between simulations and experimental results. In this thesis, a portable sensor, known as an inertial-measurement-unit (IMU), is used as a new tool to study pneumatic conveying particle dynamics at a relatively low conveying velocity (or dense-phase flow) in horizontal gas-solid two-phase pipe flow. In order to get useful information, an IMU-based trajectory reconstruction algorithm has been developed. The algorithm uses the quaternion method to realize coordinate transfer between local and IMU frames, and an extended Kalman filter to filter the Gaussian white noise. The sensor's dynamics information, such as global acceleration, is obtained by analysis of IMU data and is available for future research. The IMU-based trajectory reconstruction algorithm is verified by an experiment that imitates the motion of the IMU inside the pipe during pneumatic conveying. The IMU-based trajectory reconstruction algorithm shows accuracy on trajectory reconstruction results. The techniques that have been developed in this work are shown to provide a new inexpensive and straight-forward method with which to study particle dynamics.

TABLE OF CONTENTS

LIST OF TABLES

LIST OF FIGURES

PREFACE

This thesis has been written to fulfill the graduation requirement of Swanson School of Engineering.

I would like to thank my supervisor Dr. Clark and Dr. Klinzing for his excellent guidance and support during my research. I would also like to thank PhD students Marcus Allen, without whose tutoring and helping at the early stage I would not have been able to conduct my research. And also, I wish to thank another Ph.D. Student Mingming Zhang for his help in this project.

1.0 INTRODUCTION

Pneumatic conveying is one of the most popular methods of handling bulk powdered and granular materials in mining, chemical and agricultural industries. The process of pneumatic conveying has existed for more than 100 years. The first documentary record appears from 1856 to 1876 in the ports of London, where people took advantage of pneumatic conveying technology to unload grain from ships (Klinzing, 2018). Pneumatic conveying shows great value in current daily life and industry. For example, an Ishinomaki Redcross Hospital in Japan uses a pneumatic tube system to achieve high speed transportation of chemicals and samples. The system saves time and human resources for logistics and transportation, which indirectly improves patient care. Providing nurses the ability to focus more on taking care of patients will lower the mortality risk (Patterson, 2007).

In industry, pneumatic conveying is widely used to transport many types of materials. Vacuum conveyors are designed to transport powder and particles in an enclosed environment. This machine protects people from airborne pollution, and also shields materials from the influences of the surroundings.

Even though pneumatic conveying has been used for over 150 years, it is still an open subject for study because there is still interest in making improvements in efficiency and energy consumption. The first study on record of pneumatic conveying was carried out in Germany by

Gasterstadt in 1924 (Klinzing, 2018). He studied the linear behavior of pressure drops in straight sections of pipe with solids flow.

Today the motion of particles during pneumatic conveying is studied by numerous researchers. For example, a lot of researchers used numerical simulation to study particle dynamics (Matsumoto & Saito, 1970) (Tsuji, Tanaka, & Ishida, 1992) (Xiang & McGlinchey, 2004). They use theoretical models and solve the motion mathematically. Meanwhile, other scholars study the particle dynamics experimentally. Zheng et al. used a camera system to capture the motion of particles and analyzing the fluctuating velocity (Zheng & Rinoshika, 2017), and Wang et al. used electrostatic sensor to detect the velocity of particles in a flow (C. Wang, Zhang, Zheng, Gao, & Jia, 2017).

In this paper, we are trying to create a new way to study particle dynamics by using an inertial measurement unit (IMU). An IMU is a small device that can record acceleration, angular velocity and fluctuating magnetic field while it's moving. The idea behind this project is to put the IMU inside the pipe, embedded with the particles, such that it will move with the particles. By analyzing the acceleration, angular velocity, and magnetic field measurements of the IMU, we can infer information about the forces acting on it and can calculate its trajectory, thereby obtaining better understanding of the associated particle dynamics and trajectory of the particles.

In this thesis, a new algorithm is developed to reconstruct the particle (i.e. sensor unit) trajectory from IMU data and to optimize the result through a Kalman filter. The framework of the algorithm is shown in Figure 1.1. The IMU deployment involves placing the IMU into the particle bed in the pipe. The test is then run by causing the flow to occur in the pipe and simultaneously collecting motion data with the IMU. The data from the IMU is then transformed to the global frame, and then the trajectory of the IMU's motion is reconstructed though the algorithm to be

described in this thesis. The Kalman filter is used to optimize the result. Finally, the kinetics information of interest may be obtained.

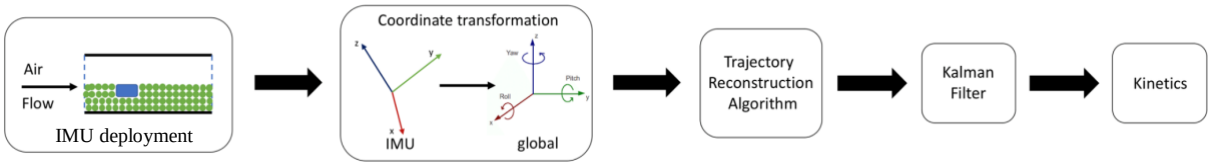

Figure 1.1 Framework of the particle dynamics analysis algorithm: IMU deployment (the green circles represent particles, and blue block represents IMU); coordinate transformation, trajectory reconstruction, Kalman filter, and kinetics analysis.

The structure of this thesis is based on the framework of the algorithm, and is organized as follows: Chapter 2 will focus on background knowledge, such as previous methods of studying pneumatic conveying and techniques used in this paper; Chapter 3 will introduce the experimental equipment and methods of pneumatic conveying experiment; Chapter 4 will introduce the step of obtaining rotation matrices to transfer the data to the global frame (by using quaternion method); Chapter 5 will show the trajectory reconstruction algorithm result of IMU moving in the pipe and discussions about the results; Chapter 6 will introduce an imitation experiment and discussion about the trajectory reconstruction algorithm results; Chapter 7 will provide information of Kalman filter development; and Chapter 8 will present conclusions and discussion of the algorithm.

2.0 BACKGROUND AND LITERATURE REVIEW

Pneumatic conveying has been studied for about a century. There are many published works in the literature on the subject, some of which will be briefly reviewed in this chapter.

In this paper, we focus on an algorithm to study the motion of particles by using an IMU as a tool. The background knowledge of IMUs will be reviewed. Accelerometers, gyroscopes and magnetometers will be studied, respectively.

2.1 MOTIVATION FOR STUDYING PNEUMATIC CONVEYING

Pneumatic conveying is popularly used because it offers the user the following seven advantages (Klinzing, Rizk, Marcus, & Leung, 2010):

1. A variety of products can be transported while being isolated from environmental effects (e.g. dust).
2. The transportation route is flexible and easily adjusted by pipeline.
3. Distribution can be to many different areas in a plant and pick-up can be from several areas.
4. Low maintenance and low manpower costs.
5. One pipeline can be used for a variety of products.
6. Pipelines provide a secure way to convey high-valued products.

7. Ease of automation and control.

However, there are still some disadvantages with pneumatic conveying that need to be overcome. For example, complex flow phenomena take place during pneumatic conveying (Klinzing et al., 2010), such as suspension flow, slug flow, plug flow; and fluidized dense-phase flow phenomena may occur as gas and solid flow through horizontal pipes. The suspension destroys the ability of conveying and is not uncommon in pneumatic conveying systems. The drag force is pointed out to be the main contributor to the conveying line pressure drop for dilute phase (Mills, Jones, & Agarwal, 2004). When a particle experiences drag force, the particle shows acceleration or deceleration, whose effect of acceleration is not understand yet (Klinzing et al., 2010). The acceleration effect was addressed by treating it as an added mass. This concept is inaccurate and misleading when applied above the intermediate Reynolds number regime, thought it works well for describing low Reynolds number motion. According to Klinzing et al., no clear pattern of the effect of acceleration under intermediate Reynolds number regime can be found from published results.

The particular pneumatic conveying flow that is studied in this paper is called dense phase flow. The property of dense phase flow is variant depending on the properties of material being conveyed, the solid loading ratio and the conveying air velocity. However, the generality of dense phase flow is that the flow is over a deposited layer, while makes it move slowly in discrete or separate plugs of material. The dense phase flow is effective for transport and worthy of study because it has multiple benefits to the pneumatic conveying system, such as minimizing the influence on the pipe's wall, protecting the conveying materials, saving energy and having less system installation cost.

2.1.1 Methods of Studying Pneumatic Conveying

Some researchers used high-speed cameras to analyze particle dynamics (F. Yan & Rinoshika, 2011; Zheng & Rinoshika, 2017). A schematic of their set-up is shown in Figure 2.1. The sheet of light is generated by the light source and lights up particles, shown in green. The high-speed-camera scanned the interrogation area and recorded video. The video was analyzed by particle image velocimetry (PIV) software. As a conclusion, they found the fluctuating velocity patterns and features of energy distribution. The advantage of this method was that it provides a visible and intuitive way to study the dynamics. However, the equipment of this study, for example, the high-speed camera is expensive. Moreover, the effort of calibrating the camera, applying wavelet to filter the noise, and analyzing the images to obtain results, is complicated and time consuming.

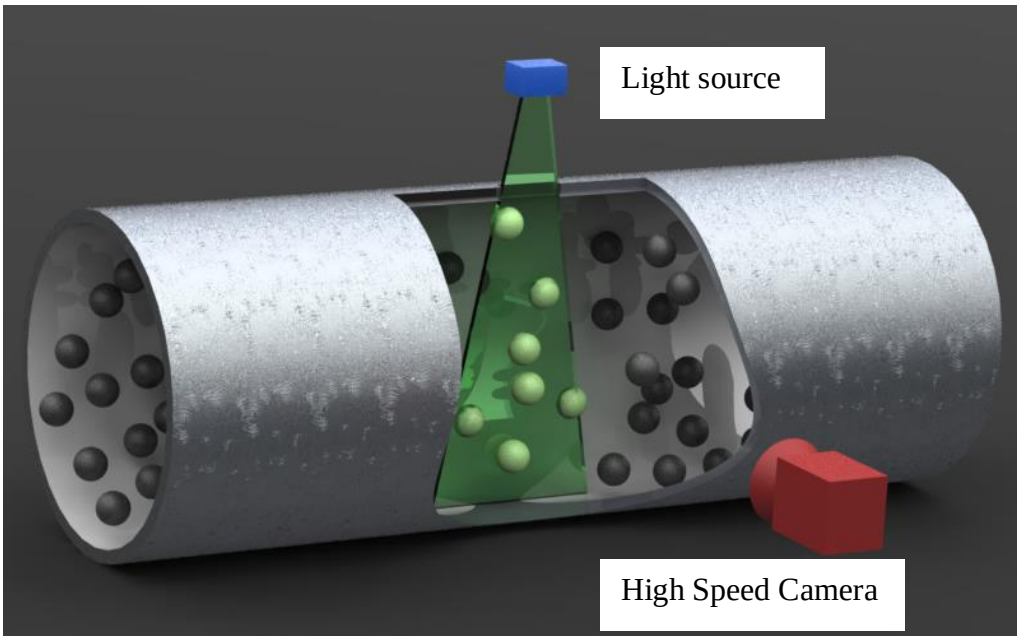

Figure 2.1 Schematic of the high-speed PIV measurement system. (Re-draw from Zheng & Rinoshika, 2017)

Recently, Wang et al. reported that the electrostatic method is one of the most promising methods for measurement of pneumatic particle conveying (Miller, Baimbridge, & Eyre, 2000)(C. Wang et al., 2017). They mounted electrodes on the inner and outer surfaces of the pipe to find particle velocities.

In that study, the charge signal from the electrostatic sensor was analyzed, then a harmonic wavelet transform was applied to decouple the signal. They found the velocity of particles and studied the relationship between particle velocity, the particle concentration distribution, and the particle flow rate. With this method, only the velocity of particles can be determined, and the set-up is very complicated, requiring holes to be drilled into the pipes.

Another technique to measure flow rate is presented by Yan (1996). The measurement relies on the detection of a rise in fluid temperature as a result of a constant heat input.. The mass flow rate is calculated by the following equation:

$$M_s = \frac{H}{C_p \cdot \Delta T} \tag{2-1}$$

where M_s is the flow rate; H is the rate of heat input; C_p is the specific heat of the fluid at constant pressure and ΔT the change in temperature measured upstream and downstream of the heated sensing section, which is $\Delta T_{c1} - \Delta T_{c2}$. This method is more applicable to dense phase solids flow because the requirement of heat conduction. Yan also mentioned the major disadvantage of this flow rate meter is its poor repeatability.

After studying pneumatic conveying by experimental methods, the information (such as air pressure and flow rate, etc.) is collected and used to develop a mathematical model for numerical simulation. Numerical simulation to study particle dynamics has been widely applied since the 1950's. The discrete element method (DEM) is used to model small scale particles'

behavior (Luding, 2008). The spring-damper system is accepted as the best way to model the contact force between particles and between particles and the wall as shown in Figure 2.2 (Tsuji et al., 1992; Xiang & McGlinchey, 2004). Xiang & McGlinchey studied the force between particles by solving equation of motion of impacting particles:

$$\frac{d^2\hat{x}(\hat{t})}{d\hat{t}^2} + a\hat{x}(\hat{t})^{1/4}\frac{d\hat{x}(\hat{t})}{d\hat{t}} + \hat{x}(\hat{t})^{3/2} = 0 \qquad \textbf{(2-2)}$$

Where $a = \frac{k}{2(mq)^{1/2}}, \hat{t} = \frac{1}{(mq)^{1/2}}, \hat{x} = xq,$ k is the spring stiffness of the model, q is the damping coefficient, m is the particle mass and x is the displacement.

In that work particle motion was simulated and the result matched the plug motion that was captured by video. Xiang et al. successfully simulated plug formation, plug collapse, and plug movement but only in two dimensions.

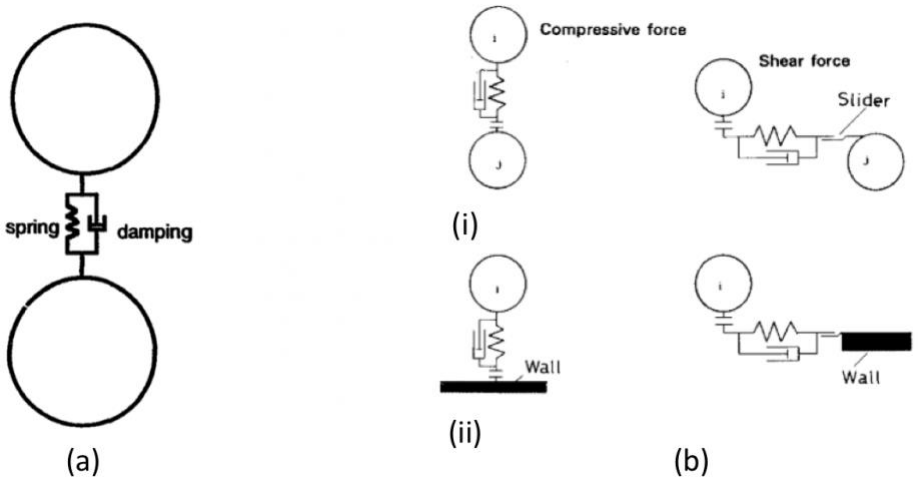

Figure 2.2 The particle contact model for numerical simulation.

(a.) the model used by Xiang & McGlinchey; (b). the model used by Tsuji et al.

The previous methods are not only very sophisticated and expensive to set up and operate, but also measure force indirectly. Moreover, the experimental methods require obtaining acceleration through velocity differentials, and the acceleration is only two-dimensional. IMUs,

on the other hand, offer a new and relatively simple possibility with which to study particle dynamics in flows by measuring acceleration directly. Because IMUs measure motion in three dimensions, the particle dynamics can be understood in three dimensional views.

2.2 INERTIAL MEASUREMENT UNIT (IMU)

An inertial measurement unit is an electronic device which is composed of an accelerometer and gyroscope. It is used to measure acceleration and angular velocity in its own frame. Some IMUs also have a magnetometer, thermometer and piezometer, which can be used to measure environmental magnetic field strength, temperature and surface pressure. IMUs are popular devices for use in sports motion analysis and navigation. For example, Zhang placed two IMUs on a human arm to study the pitching motion (M. Zhang, 2015). The system he introduced can record body segment kinematics information, which can be used to help coaches quantitatively monitoring the athlete's motion. In Zhang's work, he attached two IMUs on upper arm and forearm, respectively. The motion of pitching was recorded by those IMUs. Then he used a kinematics reconstruction method to get arm trajectory, joint angle and velocity. Finally, he applied inverse dynamics to find joint force and moment of the arm. In that work the IMU was shown to be useful for monitoring throwing kinetics.

Another extensive application of IMUs is in the navigation field. For example, quadcopters can be equipped with IMUs to help with navigation (Sa & Corke, 2012; Achtelik, Kuhnlenz, & Buss, 2009). According to Achtelik et al., an IMU was mounted on the quadcopter and used to measure attitude angle. The quadcopter was controlled and stablized based on attitude angle information from the IMU by Proportional-Derivative control. IMUs can commonly be found in

navigation systems where their data are fused with that of a Global Position System (GPS) (Lotters, Schipper, Veltink, Olthuis, & Bergveld, 1998; P. Zhang, Gu, Milios, & Huynh, 2005). Based on Lotters et al.'s work, the error model of the IMU was found. The error was caused by bias and this error accumulates with time in the integrations. This is because the IMU is a so-called dead-reckoning sensor. The process of dead-reckoning is performed by taking the last known position and the time at which it was obtained, and noting the average speed and heading since that time to the current time. To address these errors, the Kalman filter was employed to get more accurate estimation of position and velocity. This was accomplished by utilizing the GPS observations in order to determine these errors which are then used to correct the IMU.

IMUs have also been used as a tool to record motion trajectories. Wang et al. mounted an IMU on a pen (J. S. Wang, Hsu, & Liu, 2010). By calculating the trajectory of the pen, the authors were able to recognize the word that was written by the pen. They used quaternions to estimate the pen's orientation. Because the working period for writing a letter is not long (about 4 sec), they handled the IMU's drift by an orientation error compensation method. They believed the orientation error accumulation to be a linear function in the quaternion space. They modeled a linear function to eliminate error caused by the drift as follows:

$$\boldsymbol{q}(k) = \boldsymbol{q}(k) - \boldsymbol{m}k \tag{2-3}$$

where $\boldsymbol{q}(k)$ is k^{th} quaternion; m is the slope of their linear function.

2.2.1 Accelerometer

Microelectromechanical systems (MEMS) accelerometers are widely applied in acceleration measurement because of their low-cost, easy installation and simple detection

electronics. Just as its name implies, the function of an accelerometer is acceleration measurement. The working principle of an accelerometer is measuring the displacement of a proof mass, which is caused by inertia of the mass itself – when the base moves, the proof mass resists motion, and a relative displacement ensues that is proportional to the base acceleration. The displacement is usually measured by potential difference.

There are four kinds of mechanical acceleration sensing element designs in the low price market which are popular (Acar & Shkel, 2003), and they are introduced with four examples.

The first type, for example the Endevco Model 7290A Microtron Z-axis accelerometer, is based on a suspension-beam array as shown in Figure 2.3. The design is made up of three layers. The proof mass structure in the middle layer is created using wet-etching techniques. The other two layers contain fixed capacitors. The model of this kind of device can be treated as a spring-damper system. The suspension-beam array can be regarded as the spring and the gas in the interval is the damper. Inertia force causes displacement of the proof mass, which unbalances the capacitors. The capacitor unbalance can be measured to detect the displacement and therefore the acceleration. The gas in the interval is the damping fluid, so this kind of accelerometer has a small temperature influence.

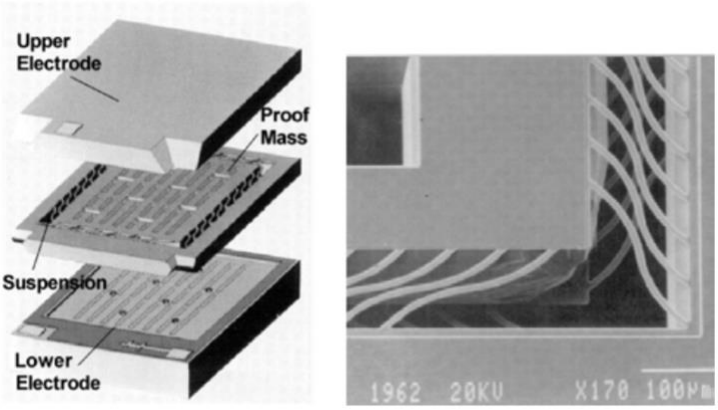

Figure 2.3 Endevco 7290A-10 accelerometer. (a) Structural design;

(b) SEM micrograph of the suspension-beam array (Acar & Shkel, 2003).

The second kind of low-cost accelerometer is a dual-axis accelerometer built using surface micromaching techniques. A picture is shown in Figure 2.4. The deflection of this structure is measured using a differential capacitor. Central electrodes are attached to the proof mass and some others are fixed to the substrate. When the proof mass moves, the differential capacitor will be unbalanced, and again this unbalance is measured to infer the causal acceleration.

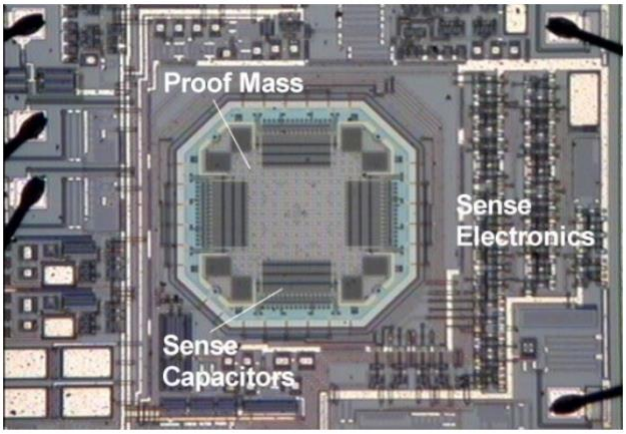

Figure 2.4 The micrograph of the integrated chip of a surface-machined accelerometer (Acar & Shkel, 2003).

The third kind of design, for example Silicon Designs SD2012-10, is a Z-axis accelerometer. An example schematic is shown in Figure 2.5. As shown in Figure 2.5, the proof

mass is held by a torsion bar. Beneath the sense element on the substrate, there are two conductive capacitors. The acceleration along the Z-axis will create a moment around the torsion axis and the capacitor will be unbalanced. Similar to the second method, the imbalance of the capacitor is proportional to acceleration.

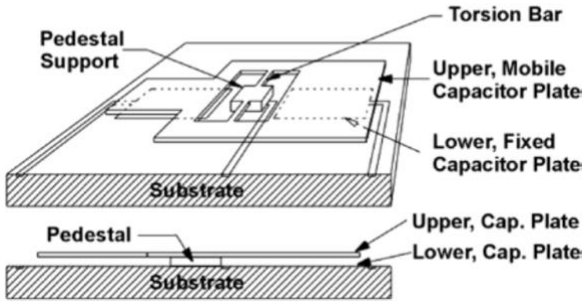

Figure 2.5 Schematic illustration of the sensing element of a Z-axis accelerometer (Acar & Shkel, 2003).

The fourth technique, for example Motorola M1220D, is also a Z-axis accelerometer. As shown in Figure 2.6, the proof mass is placed on the geometric center. The center plate can be defected when there is acceleration. The change of distance of the mass to its original place will be measured by the changing of the capacitor's value. Similar to the previous two designs, the capacitance change is proportional to acceleration.

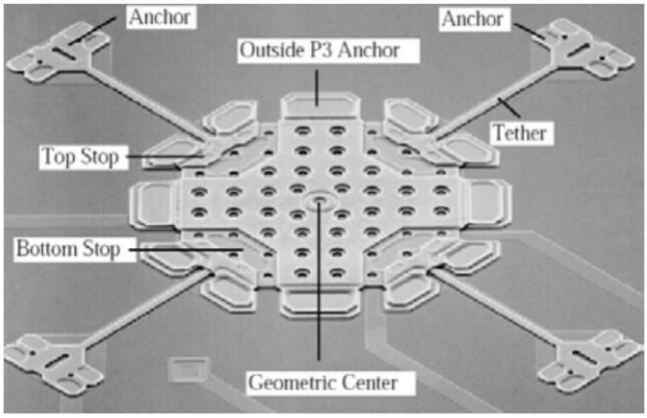

Figure 2.6 Micrograph of the sensing unit in Motorola Z-axis accelerometer (Acar & Shkel, 2003).

A triple-axis accelerometer is a combination of three single-axis accelerometers or a single-axis accelerometer and a dual-axis accelerometer. For example, Figure 2.7 shows two kinds of such combinations. Figure 2.7a shows the triple-axis accelerometer, which is composed of three single-axis accelerometers. Those three single accelerometers have similar mechanisms to Endevco Model 7290A. Figure 2.7b shows the triple-axis accelerometer, which is composed of one single-axis accelerometer and one dual-axis accelerometer. The single-axis accelerometer has similar mechanism to Endevco Model 7290A and the dual-axis accelerometer has similar mechanism to Silicon Designs SD2012-10.

The accelerometer used in this thesis is from BOSCH BMI160 sensor fusion. The detail of structural design is not found.

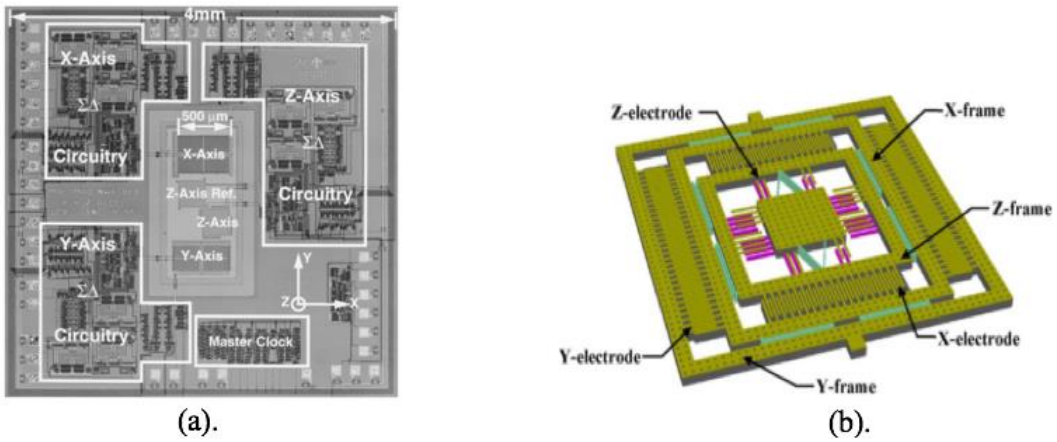

Figure 2.7 a. photograph of three-axis accelerometer (Lemkin & Boser, 1999);

b. Planar integration of three-axis sensing electrode design (Tsai, Liu, & Fang, 2012).

2.2.2 Gyroscope

The MEMS gyroscope is another important sensor in IMUs. The function of a MEMS gyroscope is angular velocity measurement. The working principle of a gyroscope is similar to

that of a MEMS accelerometer in that they both take advantage of the changing of capacitor's value due to changing distance. The topology structure of the gyroscope is shown in Figure 2.8. The proof mass in the gyroscope is constantly moving at a certain frequency. When the whole gyroscope rotates at some velocity, perpendicular relative displacement of the proof mass and the substrate will occur as a consequence of the spring (or flexible parts) deformation. This displacement is driven by Coriolis force, and the displacement causes potential difference in the capacitor, which can be measured to infer the rotation velocity by following equation:

$$\frac{\Delta V}{\Delta \Omega} = \frac{2m\omega_d y_d}{k} \cdot \frac{\varepsilon_0 l_0}{g} \cdot N \cdot V_m \tag{2-4}$$

where ΔV is changed voltage; $\Delta\Omega$ is rotation angle; m is the proof mass; ω_d and y_d respectively represent the resonant frequency and vibration amplitude of the drive mode; k is the spring constant; l_0 is overlap of comb fingers; ε_0 is dielectric property of dielectric; g is the nominal gap of the fingers; N is the number of drive comb fingers and V_m is amplitude of the input voltage.

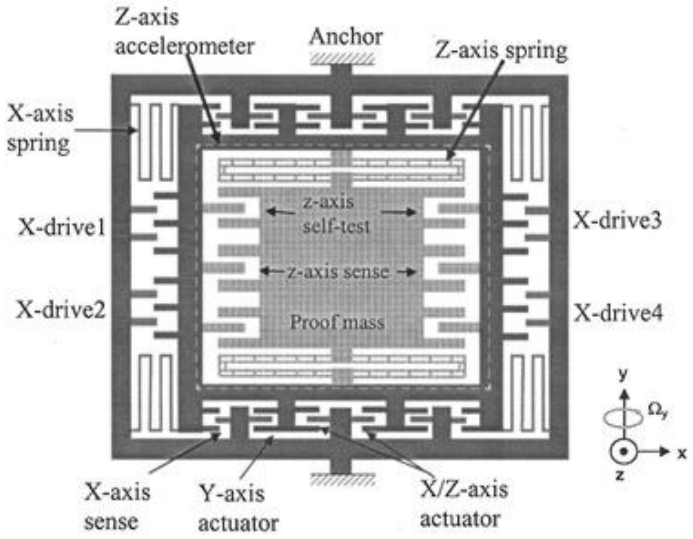

Figure 2.8 The topology graphic of the lateral-axis DRIE gyroscope (Xie & Fedder, 2002).

A drawback to this gyroscope design is that a relatively large defection of the gyroscope can be caused by thermal effects (Leland, 2005; Chong et al., 2016). Because the gyroscope is fabricated with silicon, which is a high-temperature-sensitive material and its physical properties change dramatically with environmental temperature, the measurement will be affected by temperature. In this study, we don't need to compensate for the temperature effect. The environmental temperature changes are negligible in our scenario, so the error produced by varying temperature can be ignored. However, calibration and turning on the gyroscope before doing the experiment to preheat the chip are required for each experiment.

The gyroscope used in this thesis is from BOSCH BMI160 sensor fusion. The detail of structural design is not found.

2.2.3 Magnetometer

Some IMUs are also equipped with magnetometers to help with navigation. Magnetometers are usually used to determinate the heading angle and direction. Magnetometers can be classified in accordance with their sensitivities, their physical size and their power consumption. In this section, three major types of MEMS magnetometers that are found in the market, which use different working principles, will be reviewed.

The first kind of MEMS magnetometer uses the hall effect. A schematic diagram of this kind of magnetometer is shown in Figure 2.9. If magnetic flux B is present as shown in Figure 2.9, the current I will be affected by Lorentz force. This force changes the charge distribution on the plate, inducing another current. As a result, a potential difference can be measured as V_H. The voltage exhibits a proportional relationship to the strength of the magnetic field, which is shown as follows:

$$V_H = (K_H \cdot \frac{I}{t}) \cdot B \quad \textbf{(2-5)}$$

where V_H is the output voltage in volts; K_H is the Hall effect co-efficient; I is the current flow through the plate in amps; t is the thickness of plate in mm; B is the magnetic flux density in T.

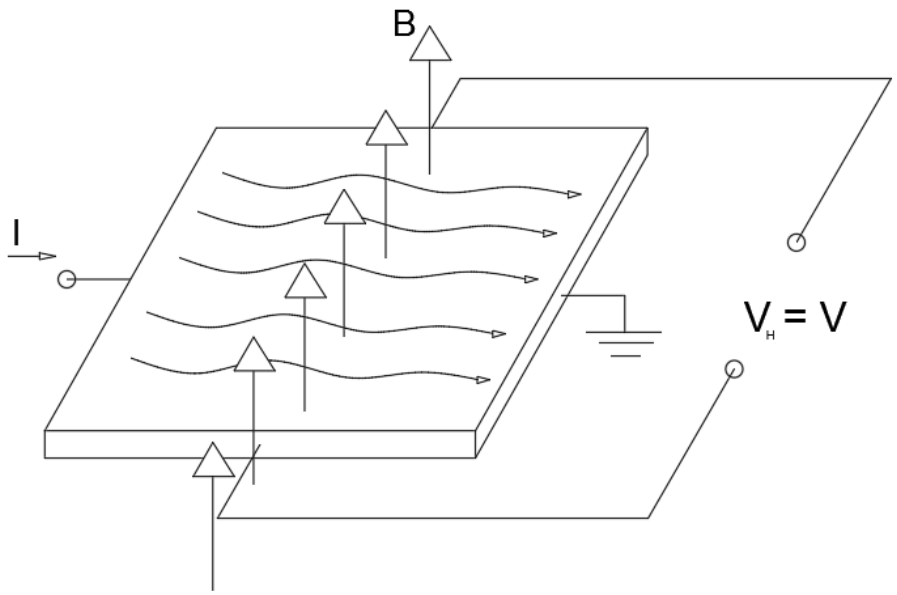

Figure 2.9 The schematic diagram of Hall-effect magnetometer.

The second working principle of magnetometer is demonstrated in Figure 2.10. As shown in the figure, the torsion beam will rotate in the presence of an ambient magnetic flux. The rotation angle of the torsion beam can be measured by another system, and the angle has relationship to the strength of magnetic field in the environment. The relationship is shown as follows (Yang et al., 2002):

$$\vec{\phi} = \frac{(\vec{M} \times \vec{H})V_{mag}}{k_\phi} \quad \textbf{(2-6)}$$

where $\vec{\phi}$ is the angular deflection; $\vec{M}$ is magnetization of the bar; volume V_{mag} is mechanically driven to align the magnetization with the external field $\vec{H}$; k_{ϕ} is the torsional beam stiffness.

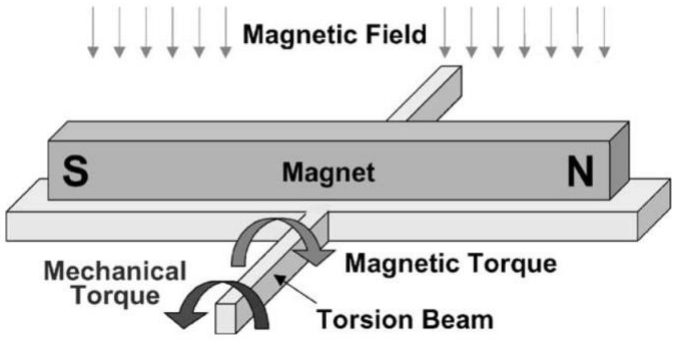

Figure 2.10 The schematic representation of micromechanical torsion beam magnetometer operation (Yang et al., 2002).

The third kind of magnetometer takes advantage of the magneto-resistive effect. A schematic diagram of this principle is shown below in Figure 2.11. The Wheatstone bridge arrangement is used to form a circuit, which exhibits an anisotropic feature. The resistance in each leg of the bridge will produce varied responses to different magnetic field strength. The output voltage can be used to calculate magnetic field using the equation:

$$\Delta M = \frac{\Delta V}{V_s} \cdot R \cdot S_M \tag{2-7}$$

where ΔM is the change of magnetic field strength; ΔV is the change of output voltage; R is original resistance of each resistor; S_M is a constant, which $S_M = -{}^{\Delta R}/_{\Delta M}$.

In this study, the magnetometer used is the third kind presented here.

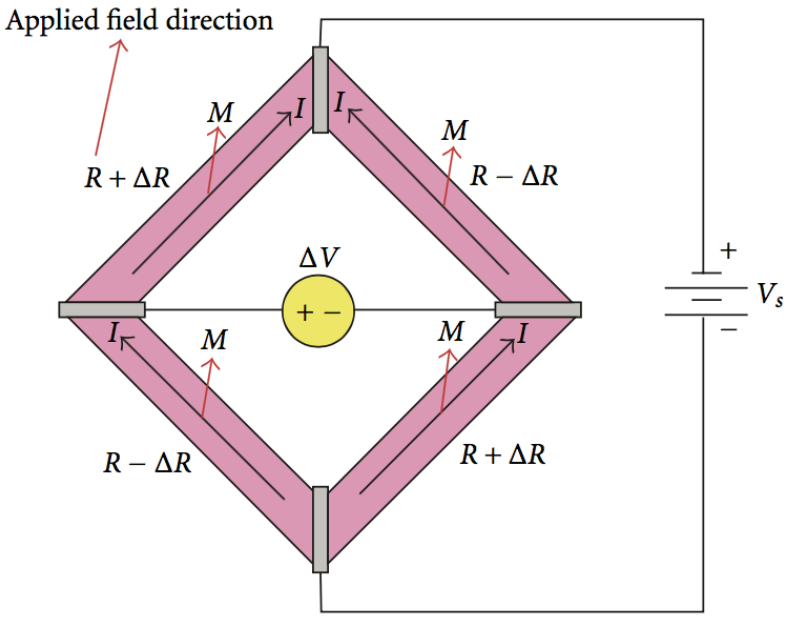

Figure 2.11 Wheatstone bridge arrangement for sensing the applied magnetic field.

3.0 EXPERIMENT EQUIPMENT AND METHODS

In this chapter, the equipment and methods of two experiments will be introduced, which are a pneumatic conveying experiment and an imitation experiment.

3.1 PNEUMATIC EXPERIEMENT

The pneumatic conveying experimental tests were conducted at the University of Pittsburgh. The schematic diagram of the pneumatic conveying experiments rig is shown in Figure 3.1. Figure 3.2 is a photo of the pipe segment of the test rig. This pneumatic conveying system is a positive-pressure system. It's comprised of the air compressor, air storage tank, standard flow meters, regulating valves, vacuum sucker, conveying pipe, receiving tank, and hopper. The end section of the pipe (about 3 meters) is made of transparent acryllic while the remaining sections of the pipe are made of stainless steel. The inner diameter of the pipe is 20mm. The pipe is installed horizontally, supported by a steel frame.

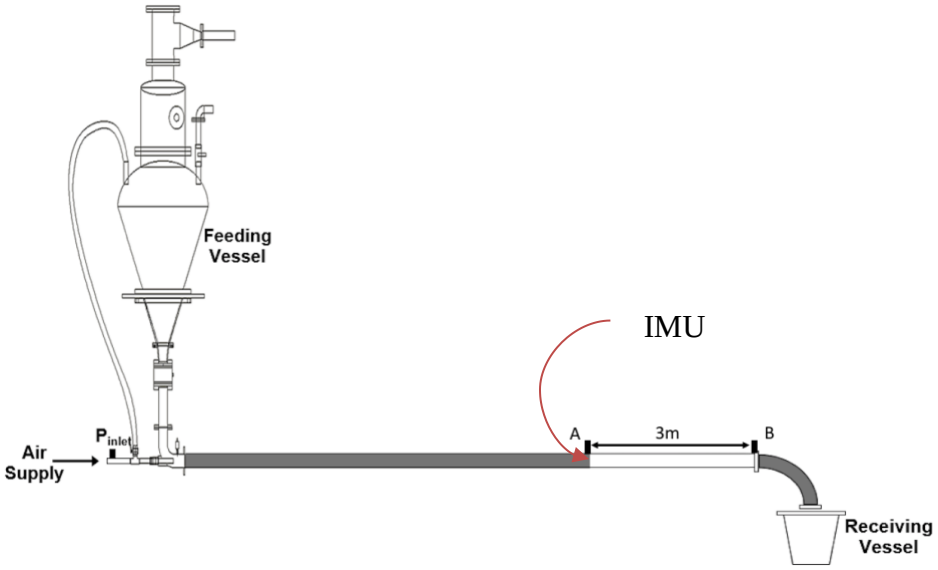

Figure 3.1 The rig of pneumatic conveying system. The part from A to B is a transparent plastic pipe, which allows easy observation of the particles' and the IMU's movement. The IMU is set at point A before every trial.

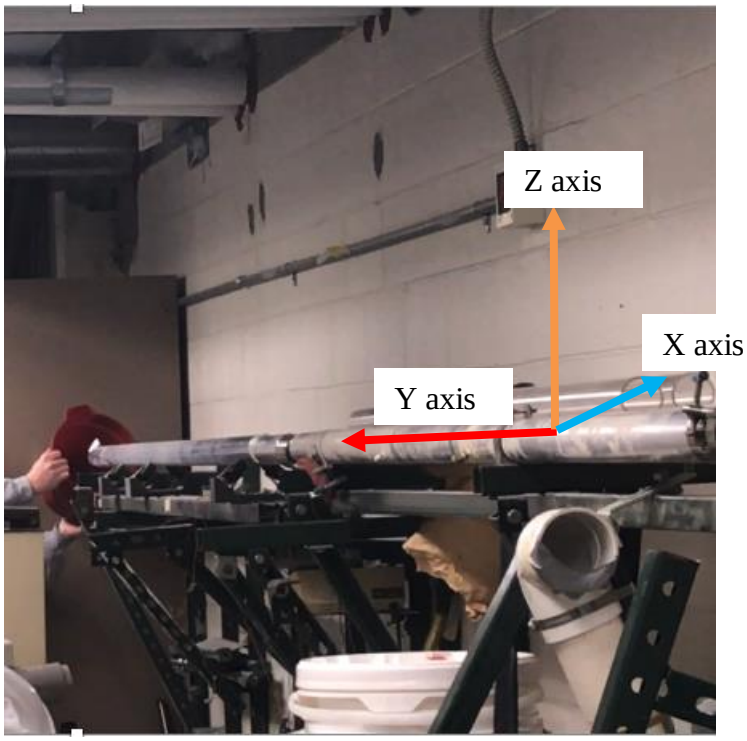

Figure 3.2 IMU moves through the transparent part and falls into the red bucket. Y axis of global frame is along the pipe, horizontal; Z axis is straight up.

The conveyed particle is Kodak PET (polyethylene terephthalate), with density of 1.3905g/cm^3, and the average particle size is 8mm^3. The velocity of air flow is from 4 m/s to 20 m/s. By controlling the air velocity and feeding mass, the mass flow rate of the particle is 2.8 kg/h.

The IMU measurement data flow is shown in Figure **3.3**. The IMU we use is an mlientlab *MetaWearC Board*. This is one of the smallest IMUs that can be found in the market, as shown in Figure **3.4**. The manufacturer specification of the IMU is shown in Table **3.1**. A small IMU is preferred so that it is close in size to the particles. It is equipped with 10-axis motion sensing, which includes 3-axis accelerometer, 3-axis gyroscope, 3-axis magnetometer and pressure sensor. It is powered by a CR2032 coin cell battery. The IMU is connected with a tablet by Bluetooth, the data is recorded in real time on the tablet using a software called MetaWear. After the data recording is finished, the data files are transmitted to the PC, where it they are analyzed by Matlab software.

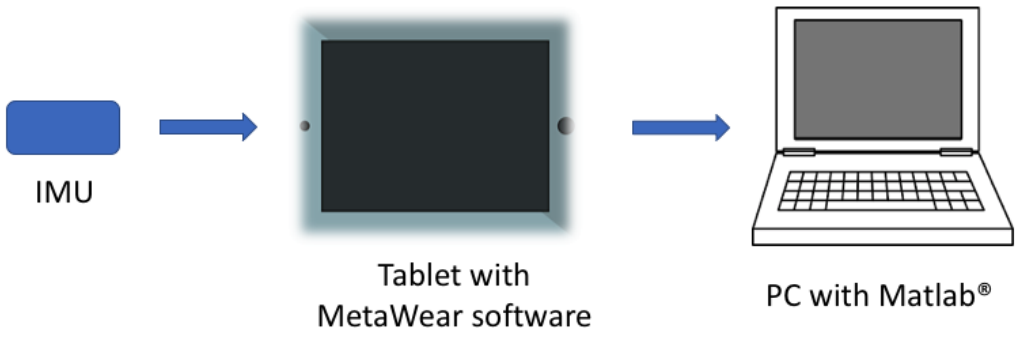

Figure 3.3 Structure of trajectory measurement data flow. The IMU is connected with tablet by Bluetooth and is then transmitted to the PC.

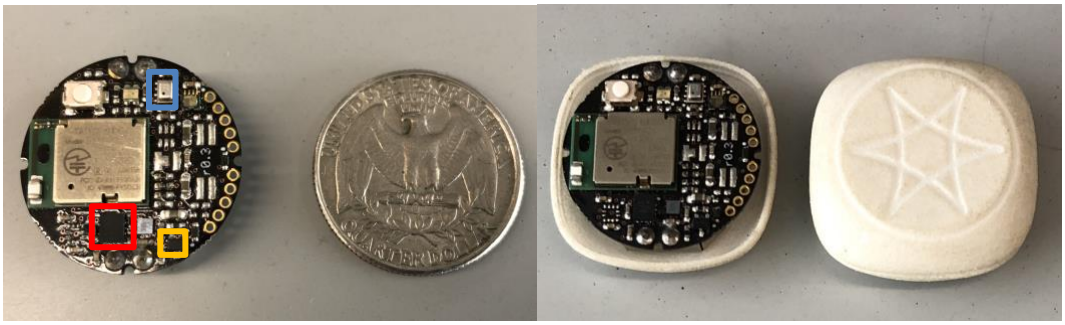

Figure 3.4 The size of IMU compared with a quarter coin and inside its plastic case. The accelerometer is shown in red box; the gyroscope is shown in blue box, and magnetometer is shown in orange box.

Table 3.1Final position error of three experiments

	Range	Sensitivity	Noise
Accelerometer (16bit)	±4g	8192LSB/g	180 μg/√Hz
Gyroscope (16 bit)	±1000°/s	32.8 LSB/°/s	0.008 °/s/√Hz
Magnetometer (16bit)	±1300μT	0.018 (0.001)	N/A

The experiment is conducted by the following steps:

1. Turn on the power supply to the vacuum, and ensure the air supply valve is fully open. The different air pressure can be achieved by tightening or loosening the air pressurizer.
2. Turn on the vacuum and suck up 0.8 kilograms of particles into the hopper.
3. After pressurizing the chamber, release the pressure and air flow pushes the particles through the pipe. At the end of the pipe the particles fall into the bucket.
4. Turn off the valve and stop the air flow.
5. Weigh the particles in the bucket.
6. If the weight is not 0.8 kilograms, the steps above are repeated until the weight is 0.8 kilogram. It is worth mentioning that after repeating several times, a stable deposit

layer is formed in the pipe. The moveable particles are set on the deposit layer, which are required to be equidistributional to reach a steady state. When the captured weight is 0.8 kilograms, the particles in the pipe are considered to be equidistributional.

7. After the particles are equidistributional, turn the IMU on and start logging data. The sample frequencies of accelerometer and gyroscope are both set at 100Hz.
8. Put the IMU into the pipe at the point shown in Figure 3.1. The direction of Y axis of IMU frame is carefully aligned with global frame.
9. Turn on the vacuum and suck up 8 kilograms of particles into the hopper.
10. After pressurizing the chamber, release the pressure so that air flow pushes the particles and the IMU through the pipe. At the end of the pipe the particles and IMU will fall into the bucket. Then turn off the valve and stop the air flow.
11. Stop logging data and transfer data files to PC.

4.0 KINEMATIC ANALYSIS

The basic idea behind this study, involving use of an IMU to infer information about particle flows, is to use local frame linear acceleration and angular velocity to extract information about the IMU kinetics and kinematics in the global frame. Once the global frame data is obtained, it can be used to learn about forces between IMU and particles by using an inverse dynamics method. A trajectory reconstruction algorithm can be used to learn the IMU path. In the pipe flow problem, the only two definitive pieces of known information are the path of the pipe and run time. Errors in the trajectory reconstruction algorithm can be assessed by comparing them with the pipe's path.

At any point in the motion, a rotation matrix is needed to transform acceleration and angular velocity between two frames, namely from the local frame (IMU frame F^{imu}) to the global frame (F^{global}). The ideal mathematical correlation between IMU accelerometer's digital reading (not considering bias, noise and other interference factors) and linear acceleration in the global frame is written as:

$$\vec{a}^{g} = R_i^g \cdot \vec{a}^{i} \tag{4-1}$$

where $\vec{a}^{g}$ is the acceleration in the global frame, R_i^g is the rotation matrix from F^{imu} to F^{g}, and $\vec{a}^{i}$ is the acceleration in the IMU frame.

To get the rotation matrix, Euler method is not considered to be used because of its disadvantages, such as gimbal lock and ambiguous correspondence to rotations (Dam, Koch, & Lillholm, 1998). The quaternion method is used for calculating frame rotations.

The quaternion based rotation matrix construction technique is better because it does not have gimbal lock, and it is geometrically intuitive (Dam et al., 1998). Moreover, the quaternion-based rotation matrix is coordinate system independent and has a simple composition method (which will be expounded in ensuing paragraphs), which gives advantage when calculating a series of rotations and programming.

4.1 QUATERNION METHOD

The quaternion method is invented by W R Hamilton in 1843 (Krishnaswami & Sachdev, 2016). Hamilton found an ingenious way to multiply triplets. He defined quaternions as a package of four dimensional vectors from vector space $\mathbb{H}$ (named after Hamilton). The quaternion $\mathbf{q}$ can be written as complex form (Eq. ((4-2)):

$$\mathbf{q} = \alpha + \beta\boldsymbol{i} + \gamma\boldsymbol{j} + \delta\boldsymbol{k} \tag{4-2}$$

while: $\boldsymbol{i} = (1,0,0)$, $\boldsymbol{j} = (0,1,0)$, $\boldsymbol{k} = (0,0,1)$ in the local reference frame (IMU frame); α, β, γ and δ are scalar terms. $\boldsymbol{i}, \boldsymbol{j}$ and $\boldsymbol{k}$ components that define the rotation axis vectors in the reference frame, meanwhile α, β, γ and δ are the angles of rotation of the frame about the vector.

Eq. (4-2) can be rewritten as Eq. (4-3):

$$\mathbf{q} = [q_0 \quad \boldsymbol{q}_1 \quad \boldsymbol{q}_2 \quad \boldsymbol{q}_3]^{\mathrm{T}} = \begin{bmatrix} q_0 \\ \boldsymbol{q} \end{bmatrix} \tag{4-3}$$

where:

$$q_0 = \alpha, \boldsymbol{q}_1 = \beta \boldsymbol{i}, \boldsymbol{q}_2 = \gamma \boldsymbol{j}, \boldsymbol{q}_3 = \delta \boldsymbol{k}, \boldsymbol{q} = [\boldsymbol{q}_1 \quad \boldsymbol{q}_2 \quad \boldsymbol{q}_3]^{\mathrm{T}} \tag{4-4}$$

According to quaternion's definition, the 2-norm of the quaternion should equal to 1, or rotation will not be pure rotation, but will have some scale factor (Kuipers, 1999). In other words, each quaternion must satisfy Eq. (4-5).

$$\sqrt{{q_0}^2 + {\boldsymbol{q}_1}^2 + {\boldsymbol{q}_2}^2 + {\boldsymbol{q}_3}^2} = 1 \tag{4-5}$$

According to the definition of quaternion rotation operator $L_q(\mathbf{v})$ (Kuipers, 1999), acting on a unit vector **v**, the coordinate fixed rotation can be expressed by follow equation:

$$L_q(\mathbf{v}) = \mathbf{q} \times \mathbf{v} \times \mathbf{q}^* \tag{4-6}$$

In Eq. (4-6), **v** is the 3-by-1 rotated vector; and $\mathbf{q}^*$ is the complex conjugate of **q**.

Another two important properties of quaternion are (Kuipers, 1999):

$$\mathbf{q}^* \times \mathbf{p}^* = (\mathbf{p} \times \mathbf{q})^* \tag{4-7}$$

$$\mathbf{p} \times \mathbf{q} = p_0 q_0 - \boldsymbol{p} \cdot \boldsymbol{q} + p_0 \boldsymbol{q} + q_0 \boldsymbol{p} + \boldsymbol{p} \times \boldsymbol{q} \tag{4-8}$$

Assuming

$$\mathbf{u} = L_q(\mathbf{v}) = \mathbf{q} \times \mathbf{v} \times \mathbf{q}^*, L_p(\mathbf{u}) = \mathbf{p} \times \mathbf{u} \times \mathbf{p}^* \tag{4-9}$$

and we can obtain:

$$L_p(\mathbf{u}) = (\mathbf{pq})^* \times \mathbf{u} \times (\mathbf{pq})^* = L_{pq}(\mathbf{v}) \tag{4-10}$$

The order subscript of $L_{pq}(\mathbf{v})$ in Eq. (4-10) means the sequence of operator which is relevant with time order:

$$\mathbf{q}(t+\Delta t) = \mathbf{q}(\Delta t) \times \mathbf{q}(t) \tag{4-11}$$

Based on Eq. (4-5), the expression can be written as a function about $\phi(t)$ and $\mathbf{v}$, which can be shown as

$$\mathbf{q} = \mathrm{r}(\phi(t), \boldsymbol{u}) = \cos(\phi(t)) + \boldsymbol{u} \cdot \sin(\phi(t)) \tag{4-12}$$

where $\boldsymbol{u}$ is the unit vector of the rotation axis, which comes from:

$$\boldsymbol{u} = \frac{\mathbf{w}(t)}{\|\mathbf{w}(t)\|} \tag{4-13}$$

where $\mathbf{w}(t)$ is the angular velocity vector, more specifically, $(w_1\boldsymbol{i}, w_2\boldsymbol{j}, w_3\boldsymbol{k})$.

Then $L_q(\mathbf{v})$ can be rewritten as follows:

$$\boldsymbol{L_q}(\mathbf{v}) = \mathbf{R}(\boldsymbol{\phi}(t), \boldsymbol{u}) = \boldsymbol{u} \times \mathbf{v} \cdot \sin\big(2\phi(t)\big) + \mathbf{v} \cdot \cos(2\phi(t)). \tag{4-14}$$

which, by replacing $2\phi(t)$ with rotation angle $\theta(t)$ can be written as:

$$\boldsymbol{L_q}(\mathbf{v}) = \mathbf{R}(\boldsymbol{\theta(t)}, \boldsymbol{u}) = \boldsymbol{u} \times \mathbf{v} \cdot \sin\big(\theta(t)\big) + \mathbf{v} \cdot \cos(\theta(t)). \tag{4-15}$$

The quaternion's expression becomes:

$$\mathbf{q} = \mathrm{r}(\theta(t), \boldsymbol{u}) = \cos\frac{\theta(t)}{2} + \boldsymbol{u} \cdot \sin\frac{\theta(t)}{2} \tag{4-16}$$

Applying Eq. (4-8) and Eq. (4-16), the derivative of $\mathbf{q}(\mathrm{t})$ can be written as:

$$\lim_{\Delta t\to 0}\left(\frac{\mathbf{q}(t+\Delta t)-\mathbf{q}(t)}{\Delta t}\right)$$

$$\begin{aligned}&=\lim_{\Delta t\to 0}[\left(\cos\frac{\theta(\Delta t)}{2}-1\right)\cos\frac{\theta(t)}{2}-\boldsymbol{u}_{\Delta}\cdot\boldsymbol{u}\sin\frac{\theta(t)}{2}\sin\frac{\theta(\Delta t)}{2}+\\&\cdot\sin\frac{\theta(t)}{2}(\cos\frac{\theta(\Delta t)}{2}-1)+\boldsymbol{u}_{\Delta}\cdot\cos\frac{\theta(t)}{2}\sin\frac{\theta(\Delta t)}{2}\\&+\boldsymbol{u}_{\Delta}\times\boldsymbol{u}\sin\frac{\theta(t)}{2}\sin\frac{\theta(\Delta t)}{2}]/\Delta t\end{aligned}\tag{4-17}$$

where $\mathbf{q}(\Delta t)=\cos\frac{\theta(\Delta t)}{2}+\boldsymbol{u}_{\Delta}\cdot\sin\frac{\theta(\Delta t)}{2}$, $\mathbf{q}(t)=\cos\frac{\theta(t)}{2}+\boldsymbol{u}\cdot\sin\frac{\theta(t)}{2}$.

When Δt tends to be zero, two approximations are made. The two approximations are:

$$\theta(\Delta t)=\|\boldsymbol{\omega}(t)\|\Delta t,\boldsymbol{\omega}(t)=\|\boldsymbol{\omega}(t)\|\boldsymbol{u}_{\Delta}\tag{4-18}$$

Then this limit problem can be solved by taking advantage of L'Hôpital's rule, which will give us the result:

$$\dot{\mathbf{q}}(t)=\lim_{\Delta t\to 0}(\frac{\mathbf{q}(t+\Delta t)-\mathbf{q}(t)}{\Delta t})=\frac{1}{2}\|\mathbf{w}(t)\|\boldsymbol{u}_{\Delta}\times\mathbf{q}(t)=\frac{1}{2}\mathbf{w}(t)\times\mathbf{q}(t)\tag{4-19}$$

One step further, Eq. (4-19) can be written as:

$$\dot{\mathbf{q}}(t)=\frac{1}{2}\begin{bmatrix}0&w_1&w_2&w_3\\-w_1&0&-w_3&w_2\\-w_2&w_3&0&-w_1\\-w_3&-w_2&w_1&0\end{bmatrix}\begin{bmatrix}q_0\\q_1\\q_2\\q_3\end{bmatrix}\tag{4-20}$$

For convenience, Eq. (4-20) is rewritten as

$$\dot{\mathbf{q}}(t)=\frac{1}{2}\Omega\cdot\vec{\boldsymbol{q}}(t)\tag{4-21}$$

where $\Omega = \begin{bmatrix} 0 & w_1 & w_2 & w_3 \\ -w_1 & 0 & -w_3 & w_2 \\ -w_2 & w_3 & 0 & -w_1 \\ -w_3 & -w_2 & w_1 & 0 \end{bmatrix}, \vec{\boldsymbol{q}}(t) = \begin{bmatrix} q_0 \\ q_1 \\ q_2 \\ q_3 \end{bmatrix}$.

Eq. (4-21) can be solved by second order integration or higher order integration (for example, fourth order integration by applying Runge Kutta method). For example, solving Eq. (4-21) by second order integration, the result will be:

$$\mathbf{q}(t) = e^{\frac{1}{2}\Omega \cdot t}\mathbf{q}(0), \mathbf{q}(t + \Delta t) = e^{\frac{1}{2}\Omega \cdot \Delta t}\mathbf{q}(t) \tag{4-22}$$

where $\mathbf{q}(0)$ is the initial quaternion which represents the initial status of the IMU. The procedure to find the initial quaternion will be explained later.

The quaternion to rotation matrix relationship is derived by Eq. (4-6) and Eq. (4-8).

$$\begin{aligned} \mathbf{r} = \mathbf{q}^* \times \mathbf{v} \times \mathbf{q} &= (2{q_0}^2 - |\boldsymbol{q}|^2)\mathbf{v} + 2(\boldsymbol{q} \cdot \mathbf{v})\boldsymbol{q} + 2q_0(\boldsymbol{q} \times \mathbf{v}) = \mathrm{R}_v^r \mathbf{v} \\ &= \begin{bmatrix} 2{q_0}^2 + 2{q_1}^2 - 1 & 2(q_1q_2 - q_0q_3) & 2(q_1q_3 + q_0q_2) \\ 2(q_1q_2 + q_0q_3) & 2{q_0}^2 + 2{q_2}^2 - 1 & 2(q_2q_3 - q_0q_1) \\ 2(q_1q_3 - q_0q_2) & 2(q_2q_3 - q_0q_1) & 2{q_0}^2 + 2{q_3}^2 - 1 \end{bmatrix} \begin{bmatrix} v_1 \\ v_2 \\ v_3 \end{bmatrix} \end{aligned} \tag{4-23}$$

R_v^r is a 3-by-3 rotation matrix based on coordinate fixed rotation, which transfers the frame from coordinate v to coordinate r.

4.2 QUATERNION APPLICATION IN IMU FRAME TRANSFER

While the IMU is moving inside the pipe, being pushed by particles, rotation of the IMU occurs as it exhibits six degree-of-freedom motion. The measurements from accelerometers, angular rate gyros, and magnetometers are in the IMU (body) frame. In order to get these quantities in the global frame, a coordinate transfer must take place.

First, in order to find the initial attitude angle, the global frame should be defined, as shown in Figure 4.1. In this step zero yaw angle ψ is assumed to simplify the calculation process, which will lead to an intermediate frame. The intermediate frame can be transformed to global frame by solving the real ψ, which will be discussed in Chapter 5. Then the process assumes that the global frame is fixed and that the IMU frame is rotated to a certain posture. Because there is no rotation acting on the *Z* axis, any posture can be made by the product of $R_x(\phi)$ and $R_y(\theta)$. Supposed that the rotation about *Y*-axis is followed by the rotation about *X*-axis. The sequence of rotation matrix is:

$$\boldsymbol{F}^{global} = R_y(\theta)R_x(\phi)\boldsymbol{F}^{imu} \tag{4-24}$$

where $\boldsymbol{F}^{global}$ is the global frame and $\boldsymbol{F}^{imu}$ is the IMU frame, as mentioned before.

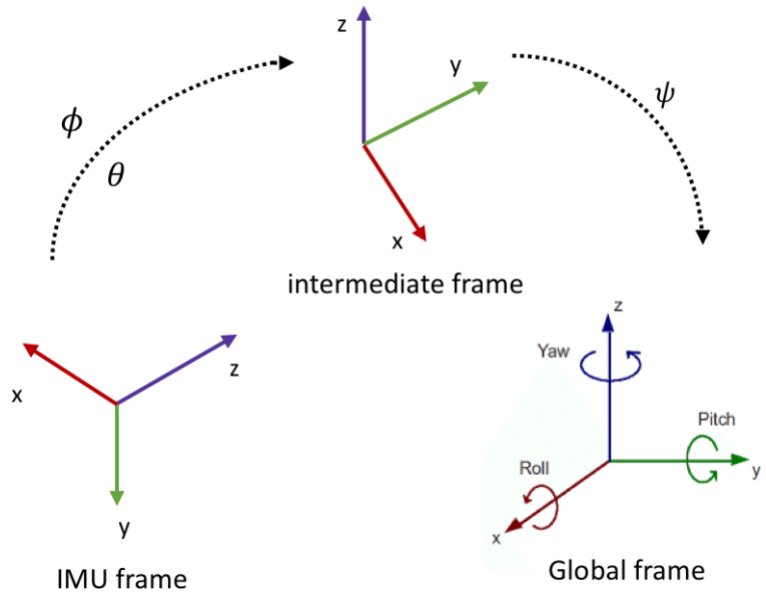

Figure 4.1 Frame transform

By the Euler method, the rotation matrix is shown below:

$$R_x(\phi) = \begin{bmatrix} 1 & 0 & 0 \\ 0 & \cos(\phi) & \sin(\phi) \\ 0 & -\sin(\phi) & \cos(\phi) \end{bmatrix}, R_y(\theta) = \begin{bmatrix} \cos(\theta) & 0 & -\sin(\theta) \\ 0 & 1 & 0 \\ \sin(\theta) & 0 & \cos(\theta) \end{bmatrix} \quad \textbf{(4-25)}$$

Eq. (4-24) can be rearranged as:

$$\boldsymbol{F}^{imu} = (R_y(\theta)R_x(\phi))^{-1}\boldsymbol{F}^{global} \quad \textbf{(4-26)}$$

Since the gravity is the only force applied on IMU when it is motionless, the acceleration in global frame is $[0 \quad 0 \quad g]^{\mathrm{T}}$. The relationship between acceleration in IMU frame and global frame when IMU is motionless can be written as Eq. (4-27).

$$\begin{bmatrix} a_x \\ a_y \\ a_z \end{bmatrix} = \begin{bmatrix} 1 & 0 & 0 \\ 0 & \cos(\phi) & -\sin(\phi) \\ 0 & \sin(\phi) & \cos(\phi) \end{bmatrix} \begin{bmatrix} \cos(\theta) & 0 & \sin(\theta) \\ 0 & 1 & 0 \\ -\sin(\theta) & 0 & \cos(\theta) \end{bmatrix} \begin{bmatrix} 0 \\ 0 \\ g \end{bmatrix} \quad \textbf{(4-27)}$$

By solving Eq. (4-27), the roll angle θ and the pitch angle ϕ are derived from the filtered acceleration signal.

$$\theta = \tan^{-1}\frac{a_x}{\sqrt{{a_y}^2 + {a_z}^2}}, \phi = \tan^{-1}(-\frac{a_y}{a_z}) \quad \textbf{(4-28)}$$

The parameter of quaternion representation is computed by following equations (Kuipers, 1999):

$$\begin{aligned} q_0 &= \cos\left(\frac{\psi}{2}\right)\cos\left(\frac{\theta}{2}\right)\cos\left(\frac{\phi}{2}\right) + \sin(\frac{\psi}{2})\sin(\frac{\theta}{2})\sin(\frac{\phi}{2}) \\ q_1 &= \cos\left(\frac{\psi}{2}\right)\cos\left(\frac{\theta}{2}\right)\sin\left(\frac{\phi}{2}\right) - \sin(\frac{\psi}{2})\sin(\frac{\theta}{2})\cos(\frac{\phi}{2}) \\ q_2 &= \cos\left(\frac{\psi}{2}\right)\sin\left(\frac{\theta}{2}\right)\cos\left(\frac{\phi}{2}\right) + \sin(\frac{\psi}{2})\cos(\frac{\theta}{2})\sin(\frac{\phi}{2}) \\ q_3 &= \sin\left(\frac{\psi}{2}\right)\cos\left(\frac{\theta}{2}\right)\cos\left(\frac{\phi}{2}\right) - \cos(\frac{\psi}{2})\sin(\frac{\theta}{2})\sin(\frac{\phi}{2}) \end{aligned} \quad \textbf{(4-29)}$$

By applying Eq. (4-29), the initial quaternion $\mathbf{q}(0)$ is found:

$$\mathbf{q}(0) = [\cos\left(\frac{\theta}{2}\right)\cos\left(\frac{\phi}{2}\right), \cos\left(\frac{\theta}{2}\right)\sin\left(\frac{\phi}{2}\right), \sin\left(\frac{\theta}{2}\right)\cos\left(\frac{\phi}{2}\right), -\sin(\frac{\theta}{2})\sin(\frac{\phi}{2})]^{\mathrm{T}} \quad \textbf{(4-30)}$$

The sample rate of the gyroscope is 100Hz that time interval of each data is regarded as Δt in Eq. (4-22). The Eq. (4-22) can be written as:

$$\mathbf{q}(k+1) = e^{\frac{1}{2}\Omega\cdot\Delta t}\mathbf{q}(k), k = 0,1,\cdots \quad \textbf{(4-31)}$$

where $\mathbf{q}(k)$ is the k[th] quaternions.

As Eq. (4-23) indicated:

$$\boldsymbol{F}^{global} = \mathbf{R}_{imu}^{global}\boldsymbol{F}^{imu} \quad \textbf{(4-32)}$$

where $\mathbf{R}_{imu}^{global} = \begin{bmatrix} 2{q_0}^2 + 2{q_1}^2 - 1 & 2(q_1q_2 - q_0q_3) & 2(q_1q_3 + q_0q_2) \\ 2(q_1q_2 + q_0q_3) & 2{q_0}^2 + 2{q_2}^2 - 1 & 2(q_2q_3 - q_0q_1) \\ 2(q_1q_3 - q_0q_2) & 2(q_2q_3 - q_0q_1) & 2{q_0}^2 + 2{q_3}^2 - 1 \end{bmatrix}$.

Now we are able to transfer acceleration from the IMU frame to the global frame at each time step of the data.

4.3 TRAJECTORY CALCULATION

After getting acceleration in the global frame, the effect of gravity must be subtracted so that the acceleration can be integrated to obtain velocities and positions of the IMU vs time. The 'real acceleration' in global frame $\boldsymbol{A}_r$ is calculated by equation of the subtraction as shown in Eq. (4-33):

$$\boldsymbol{A}_r = (\mathbf{R}_{imu}^{global}\boldsymbol{A}_{imu} - [0 \quad 0 \quad 1]^{\mathrm{T}}) \cdot g \tag{4-33}$$

The velocity can be derived by integrating acceleration

$$\boldsymbol{V} = \int_o^t (\boldsymbol{A}_r)dt \tag{4-34}$$

where $\boldsymbol{V}$ is velocity and t is motion duration.

The trajectory can then be derived by integrating again

$$\boldsymbol{P} = \iint_0^t (\boldsymbol{A}_r)dt \tag{4-35}$$

where $\boldsymbol{P}$ is the position of the IMU.

5.0 EXPERIMENT RESULTS AND DISCUSSION

The pneumatic conveying experiment introduced in Chapter 3 has been done twenty times, each producing similar results. An example case is shown here for discussion.

5.1 EXPERIMENT RESULT

The raw data from the IMU in the experiment is shown in Figure 5.1. The gyroscope's data is used to detect the start of motion of the IMU and the accelerometer's data is used to detect the end of motion. The part before point A in Figure 5.1 is defined as prior static phase, which is covered by blue. The part between point A and B is defined as the dynamic phase, which continues for 1.68 seconds in this example. During this phase the IMU is moving with the particles inside the pipe. The dynamic phase is zoomed in Figure 5.2 for a better look. The point B is when the IMU starts to fall into the bucket at the end of the pipe. The IMU is doing free-fall between point B and B'. The period between point B and C is defined as the posterior static phase. The IMU sits inside the bucket during this time period. Between points C and D the IMU is taken out of the bucket and is placed on a flat table after point D.

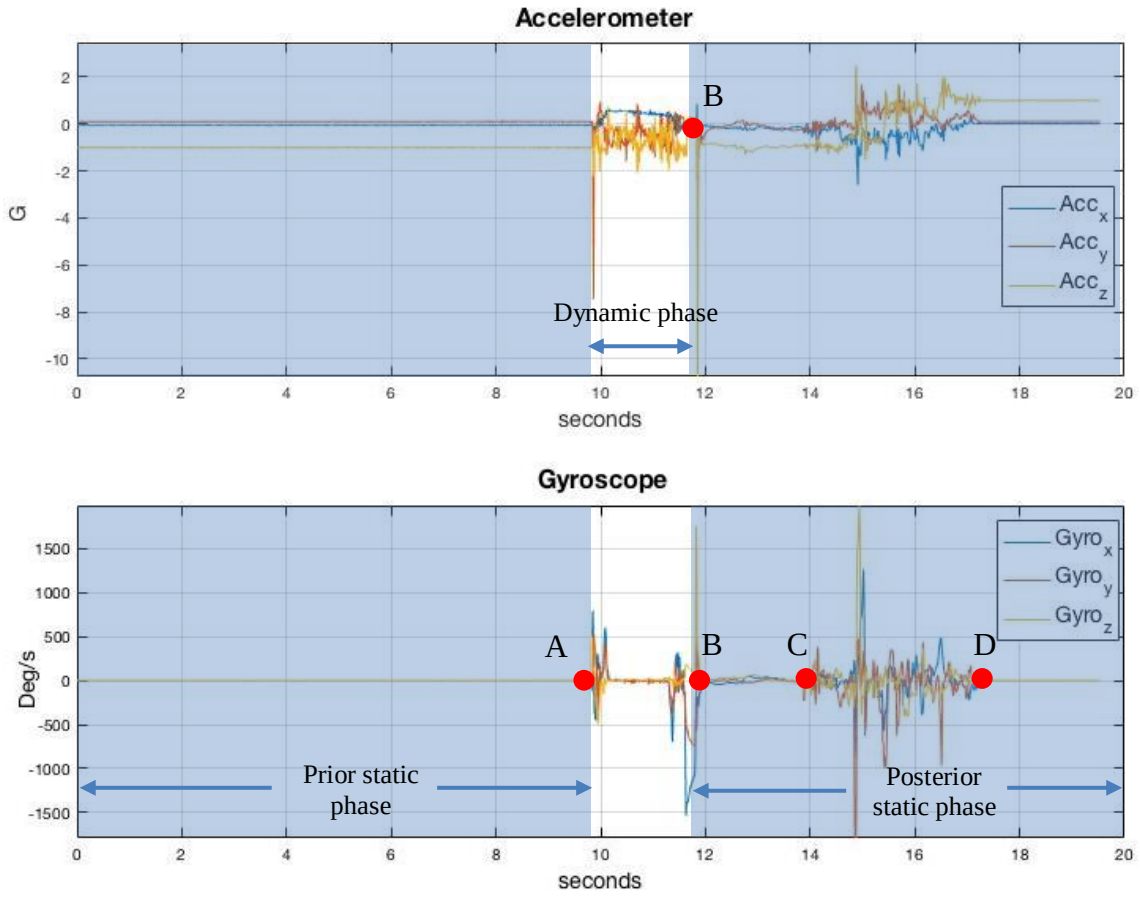

Figure 5.1 Example raw data from IMU in an experiment, (top) accelerometer data, (bottom) angular rate gyro data. A is the motion start point; B is the motion end point of pneumatic conveying process; the section between C and D is the process of finding the IMU and taking it out of the bucket.

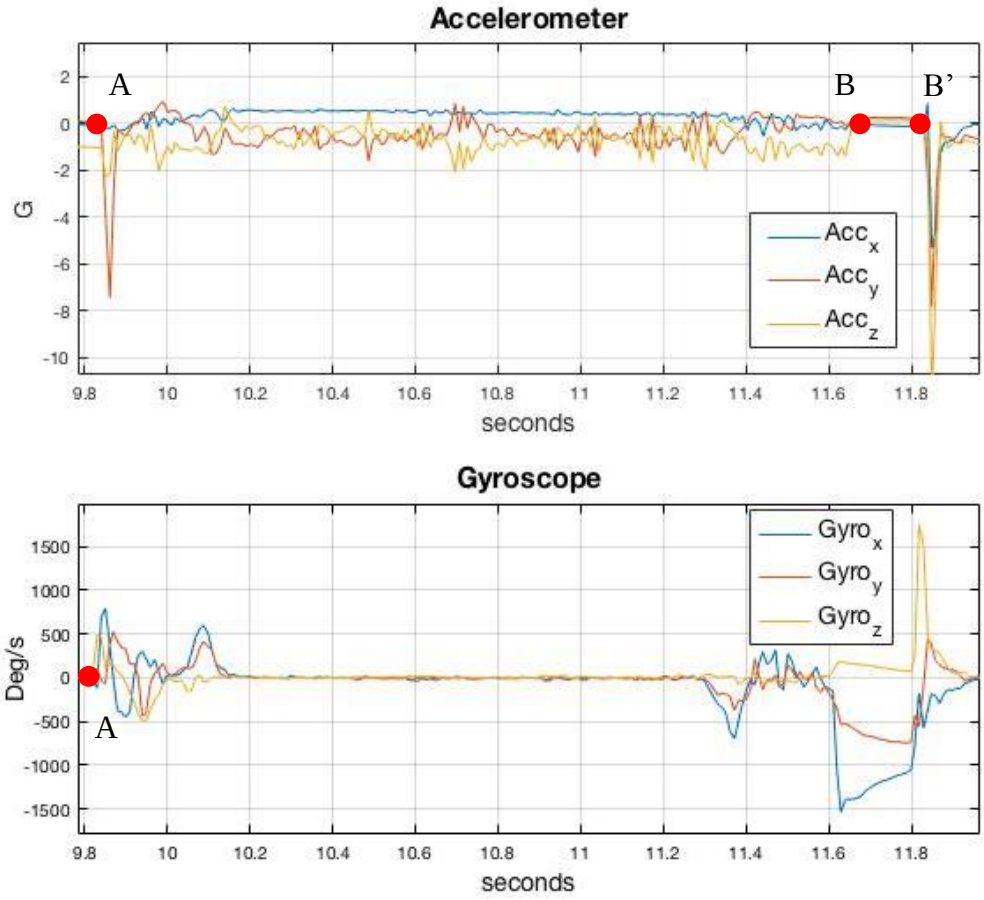

Figure 5.2 Zoomed-in example raw data of dynamic phase from IMU

By studying the raw gyroscope data, in this example the IMU rotates fast from 9.82s to 10.15s, for about 0.33s. After that the IMU barely rotates for about 1.15s. Then it starts rotation again when it approaches the pipe exit.

The initial roll angle (ϕ) and the initial pitch angle (θ) of the IMU are derived from prior static acceleration data by using Eq. (4-28) in Chapter 4, which is restated below.

$$\theta = \tan^{-1}\frac{a_x}{\sqrt{{a_y}^2 + {a_z}^2}}, \phi = \tan^{-1}(-\frac{a_y}{a_z}) \quad \textbf{(5-1)}$$

Considering the limitation of arctangent, Eq. (5-1) is rewritten as Eq. (5-2) (J. S. Wang et al., 2010).

$$\phi = \tan^{-1}\left(\frac{a_y}{a_z}\right), \text{for } a_z < 0$$

$$\phi = \tan^{-1}\left(\frac{a_y}{a_z}\right), \text{for } a_z > 0 \text{ and } a_y > 0 \qquad \textbf{(5-2)}$$

$$\phi = \tan^{-1}\left(\frac{a_y}{a_z}\right), \text{for } a_z < 0 \text{ and } a_y < 0$$

Then by using the algorithm which is derived in Chapter 4, we are able to transfer acceleration at all points in time in the IMU frame to the intermediate frame. Since the IMU is a dead-reckoning sensor, the data for an initial period is reliable. The first 1 second's trajectory result is yawed ψ degree to make the motion direction aligned with Y axis, and by doing this, the intermediate frame is transported to the global frame. The result has been plotted in Figure 5.3. The E point is an impact point where moving particles collide with or begin initial acceleration of the static IMU. After that point the acceleration primarily changes in the Y axis. In other words, the IMU is under an acceleration and deceleration process in Y, while it experiences little motion in the other two directions. The result of velocity is shown in Figure 5.4, the magnitude of average velocity is about 3m/s.

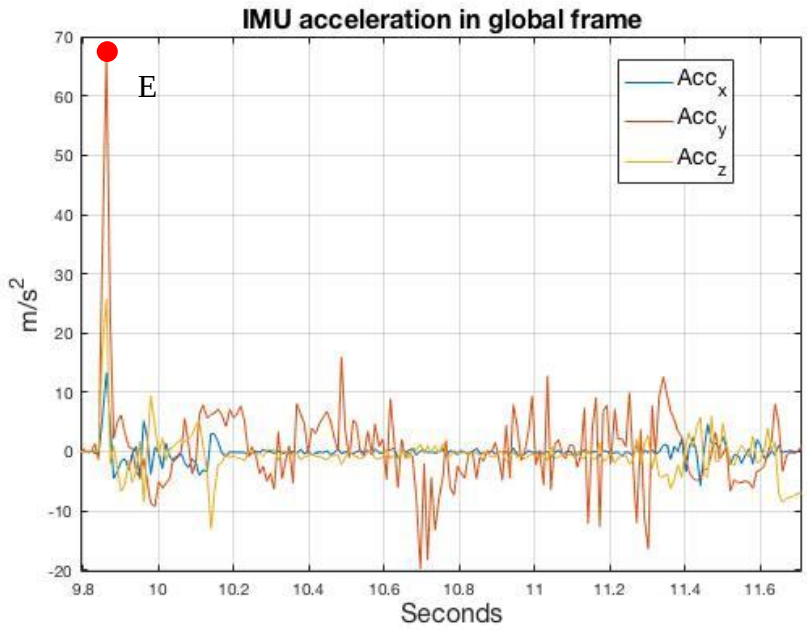

Figure 5.3 IMU Acceleration in global frame

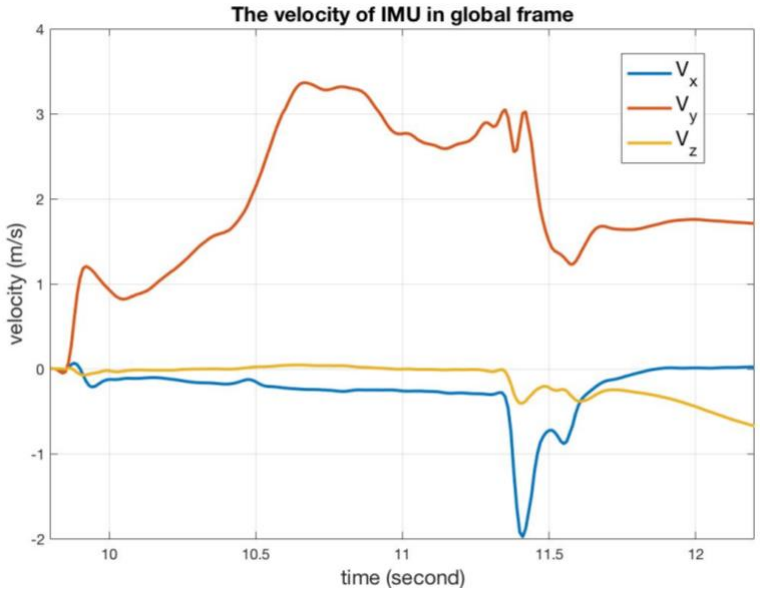

Figure 5.4 IMU Velocity in global frame

A single and double integration, respectively, is applied to the acceleration signal to get the IMU velocities and positions along the trajectory. The resulting trajectory for the data set in this example is shown in Figure 5.5. The start point is shown at the red star, whose coordinates are [0,

0, 0]. The end point is shown at the blue star, whose coordinates are [-0.283, 3.059, -0.465]. The trajectory is shown as a black line. For comparison, a pipe is overlaid as a reddish transparent cylinder. As shown in Figure 5.5a and Figure 5.5b, the IMU is moving forward along Y axis. The IMU appears to be uplifted and then it moves down slightly in the Z direction as shown in Figure 5.5c. This kind of feature matches with what we have observed in the experiment.

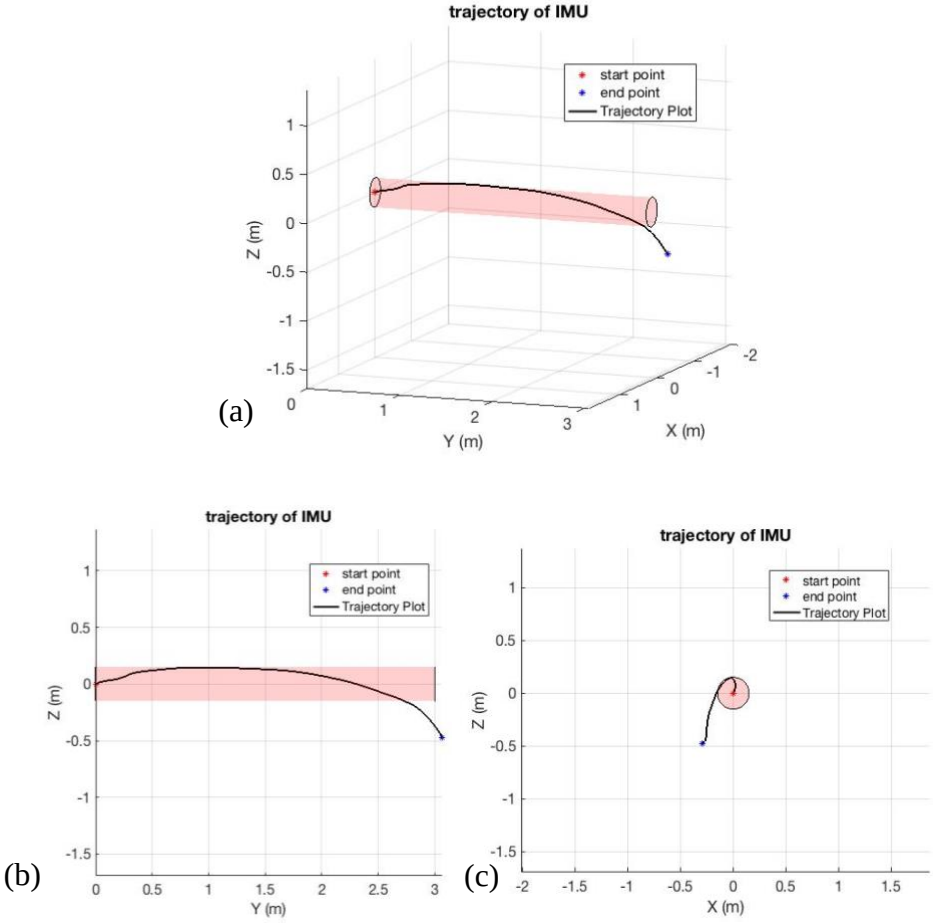

Figure 5.5 Plot of the IMU trajectory. (a) is an oblique view, (b) is lateral view and (c) is the front view. The black solid line is the IMU's trajectory and the reddish transparent cylinder represents the pipe.

However, the end portion of the trajectory of the IMU goes outside of the limitation of the pipe. The intuitive conclusion is that the acceleration and/or gyro data are not equal to the true value.

This is because the accelerometer's and gyroscope's signals are composed of noise and drift. The mathematic model of each signal is defined as:

$$\boldsymbol{a}_{accelerometer} = \boldsymbol{a}_{truth} + f_d^a(t) + noise^a; \boldsymbol{w}_{gyroscope} = \boldsymbol{w}_{truth} + f_d^w(t) + noise^w \quad \textbf{(5-3)}$$

where $\boldsymbol{a}_{accelerometer}$ and $\boldsymbol{w}_{gyroscope}$ are the raw data received from the IMU, $\boldsymbol{a}_{truth}$ and $\boldsymbol{w}_{truth}$ are the true values of the motion, $f_d^a(t)$ and $f_d^w(t)$ are drift functions for the accelerometer and gyroscope with respect to time, and $noise^a$ and $noise^w$ are the white Gaussian measurement noise. In order to get accurate acceleration and angular velocity data for motion, we have to find $\boldsymbol{a}_{truth}$ and $\boldsymbol{w}_{truth}$.

$$\boldsymbol{a}_{truth} = \boldsymbol{a}_{accelerometer} - f_d^a(t) - noise^a; \boldsymbol{w}_{truth} = \boldsymbol{w}_{gyroscope} - f_d^w(t) - noise^w \quad \textbf{(5-4)}$$

5.2 CHAPTER CONCLUSION

In this chapter, we introduced the pneumatic conveying experiment equipment, method and IMU trajectory result. The trajectory reconstruction algorithm works, but because of the error in raw data, we can't get an accurate trajectory result. In order to get an accurate trajectory, we have to address errors in the measurement, described in Eq. (5-1). As mentioned in Chapter 2, the IMU is a dead-reckoning sensor, which accumulates error with time.

6.0 IMITATION EXPERIMENT

Some researchers reported Allan Variance is a good tool for characterization of an IMU accelerometer and gyroscope in stationary state (Variance, El-sheimy, Hou, & Niu, 2015; Hou & El-Sheimy, 2004). In this paper, because our interest is IMU's behavior in dynamic state, a novel way to study IMU is applied. we designed a linear actuator to study the relationship between IMU's state of motion and IMU's output (mainly studied accelerometer and gyroscope's output). The imitation experiment will be explained below.

The IMU movement inside the pipe system is invisible, as it is buried among the particles, and is generally uncontrollable for testing purposes. In order to study the IMU's performance and find a baseline for Kalman filter design, we constructed a device to operate an imitation experiment, which imitates the IMU's motion during pneumatic conveying. The IMU's motion is controlled by actuators, such as steppers and DC motors in our device. A 3D CAD model is shown in Figure 6.1.

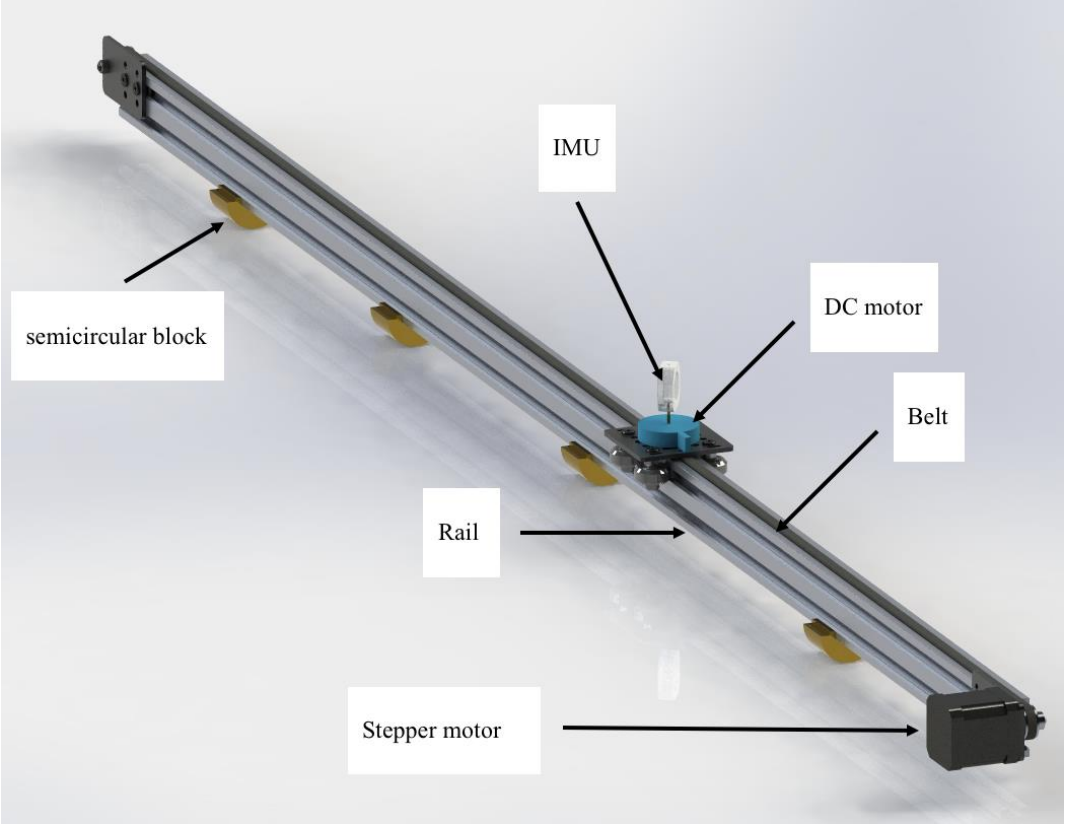

Figure 6.1 The assembly diagram of imitation experiment

This is a two-degree-freedom device. It realizes yaw by the semicircular block under the rail; and it achieves forward and backward movement by a motor-driven belt along the rail. An Arduino board is used to control stepper motor's speed. With the speed control, the commanded velocity, accepted to be the true value, can be determined and used as reference.

6.1 EQUIPMENT

The linear rail we use is a V-Slot® 20×40×1500 (mm) from Openbuilds®. The stepper motor is a NEMA 17 high torque motor that moves 1.8 deg/step and has a gear ratio of 18:1. The stepper motor driver is EasyDriver from Sparkfun®. The control board is Arduino Uno Rev3 from

Arduino®. The output of the power supply is set to 10V to drive the stepper motor. A photo of the test setup is show in Figure 6.2.

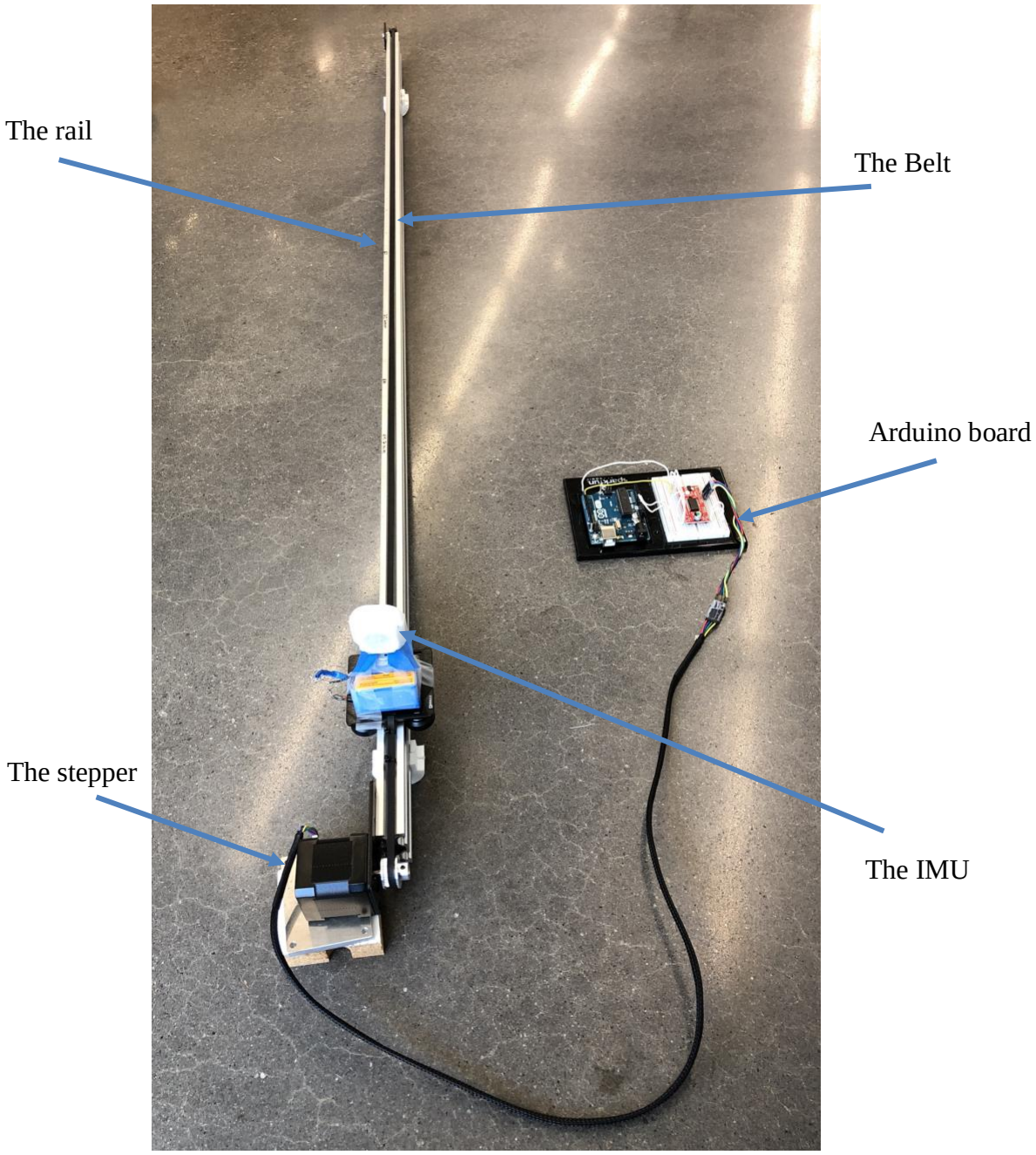

Figure 6.2 Photo of the imitation experiment test setup.

6.1.1 Control method

In the imitation experiment the motor is controlled by an Arduino Uno. The electrical wiring is shown in Figure 6.3.

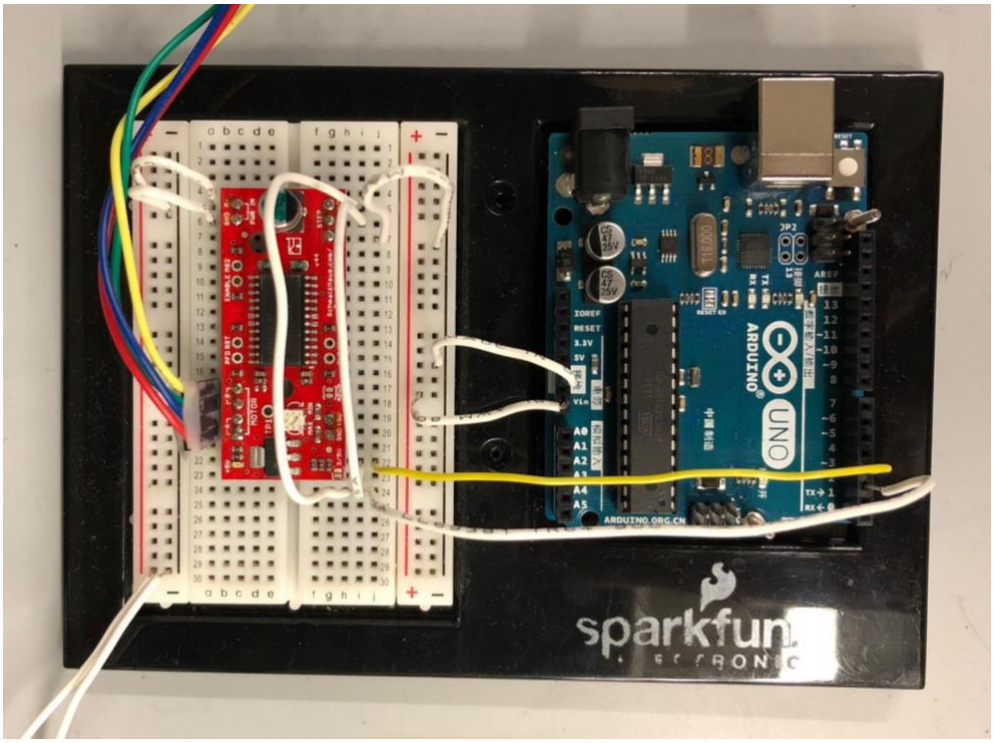

Figure 6.3 The electrical wiring for control system

The controller enables moving IMU at known speeds and directions.

6.2 EXPERIMENTAL METHODS

In order to study the IMU's behavior and performance under different motions, several different groups of experiments are conducted.

Experiment 1: The speed of the IMU plate is set to be 0.125m/s and it is prescribed to move forward 1.25m from point A to point B (as shown in Figure 6.4a); then the IMU plate stays at point B for 2 seconds; then the plate travels back to point A at a speed of 0.125m/s and it stops at point A.

It's worth mentioning that in pipe tests the IMU travels at about 3m/s as shown in Figure 5.3. The commanded velocity in the imitation experiment is not 3m/s because of the following reason. As mentioned in Chapter 2, the IMU is a dead-reckoning sensor and the error accumulates with time. In order to test our trajectory reconstruction algorithm, because we were constrained on the distance that could be traveled, we intentionally increased the traveling time to exacerbate the errors. Therefore, the velocity is set to be 0.125m/s. The backward trajectory is not a part of motion imitation, but brings convenience for conducting experiment repeatedly to make sure the result has generality.

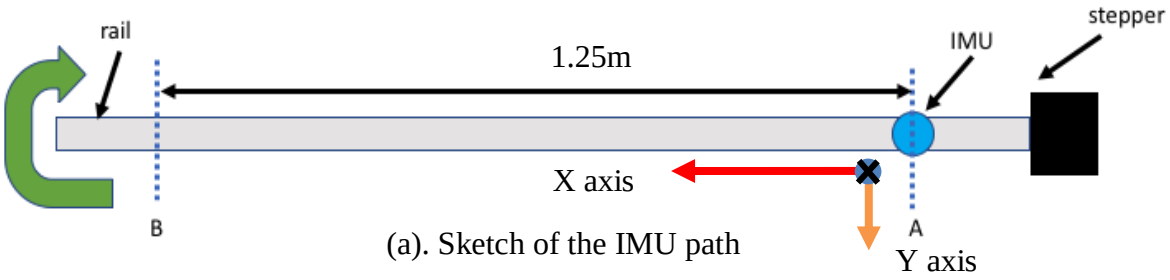

(a). Sketch of the IMU path

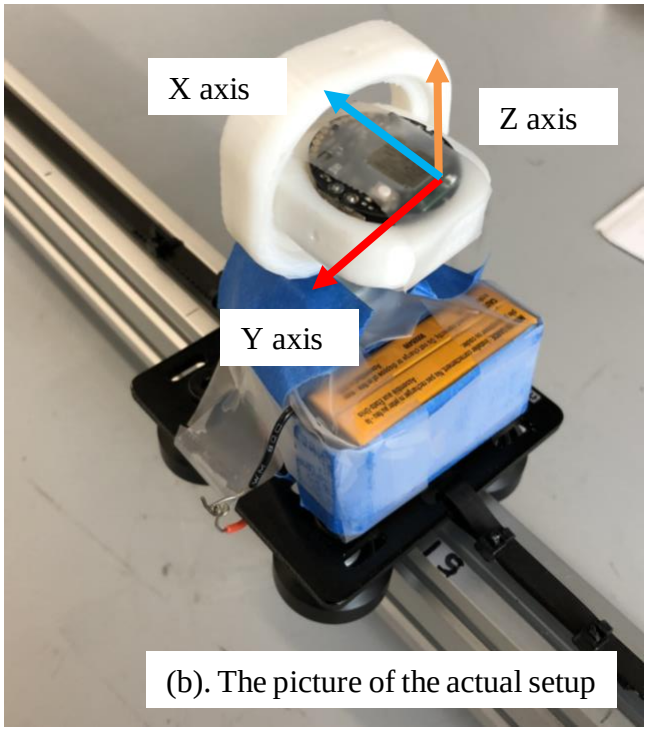

(b). The picture of the actual setup

Figure 6.4 Experiment 1 setup. a). Sketch of the IMU path in the imitation experiment (top view). The IMU moves from point A to point B at constant speed of 0.125m/s, and goes back to point A after staying at point B for about 2 seconds; b). The picture of the actual setup with IMU body frame.

A sample of raw accelerometer data (with only the bias removed) from the IMU is shown in Figure 6.5a. It shows that the whole motion, moving from A to B and then B to A, takes 23.35 seconds (9.82s to 33.18s). Before the 9.82s point in Figure 6.5, the IMU is static. The initial quaternion is solved using information in this period of time. And as highlighted by red circles, a positive peak will follow with a negative peak, vice versa. The reason for this phenomenon might be explained by a spring-damper model of the accelerometer. After applying a force, the spring-

damper system will oscillate. This does not show influence on trajectory by comparing the result of noise and bias model in Chapter 5. However, the inverse peak is unrealistic and creates difficulty for force analysis.

It's worth mentioning that the data shown here is from point A to point B and back to point A. This is because the velocity and trajectory result are used to compare with the noise and bias model's simulation results shown in Chapter 7. As time increases, the characteristic of the error will be emphasized, which will show great similarity to the simulation result.

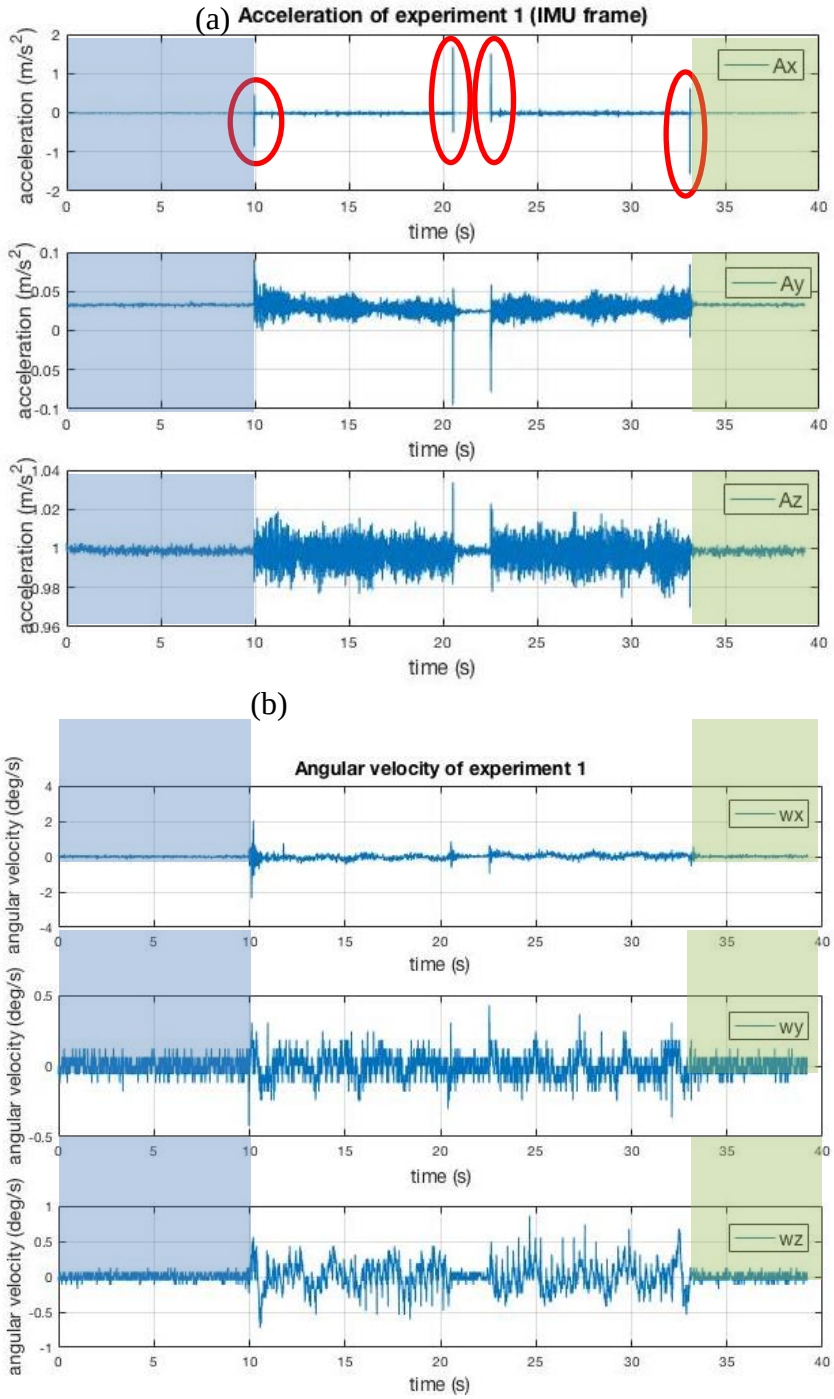

Figure 6.5 Results of experiment one (a). Acceleration result in three axes in experiment 1. (b). Gyro result in three axes in experiment 1. The transparent blue area is Prior static phase, the green area is Posterior static phase, and the uncovered area is dynamic phase.

The acceleration is transferred from the IMU frame to the global frame by using the algorithm described in Chapter 4, the result is shown in Figure 6.6. In Figure 6.6, only the motion

part (dynamic phase) is plotted, and the time stamp starts from zero. Because the IMU is set to move along the X axis, the data in Figure 6.6 shows significant acceleration change only along the X axis. But there are small fluctuations at 10.65s and 12.66s in the Y axis, highlighted with a red oval in the figure.

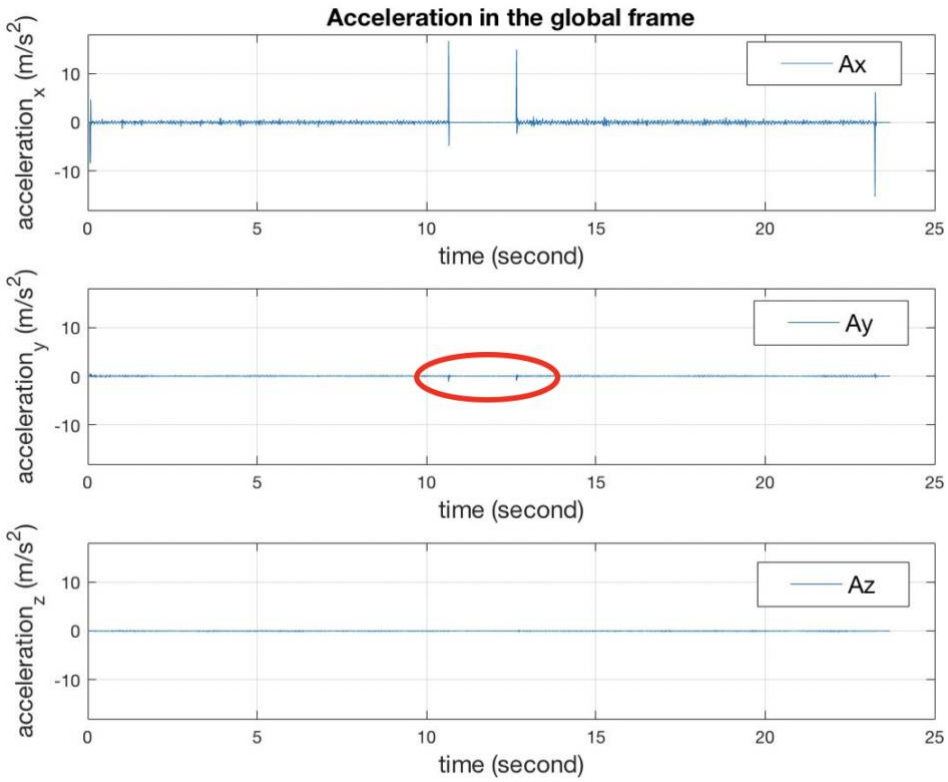

Figure 6.6 the acceleration of experiment 1 in the global frame

By integration, we are able to get the velocity and trajectory, which are plotted in Figure 6.7a and b, respectively. As shown in Figure 6.7, for a short time, the velocity obtained by processing the IMU's data is close to the designed velocity, and the calculated position is close to the true position. However, as time increases, the difference between the calculated value and the designed (true) value increases.

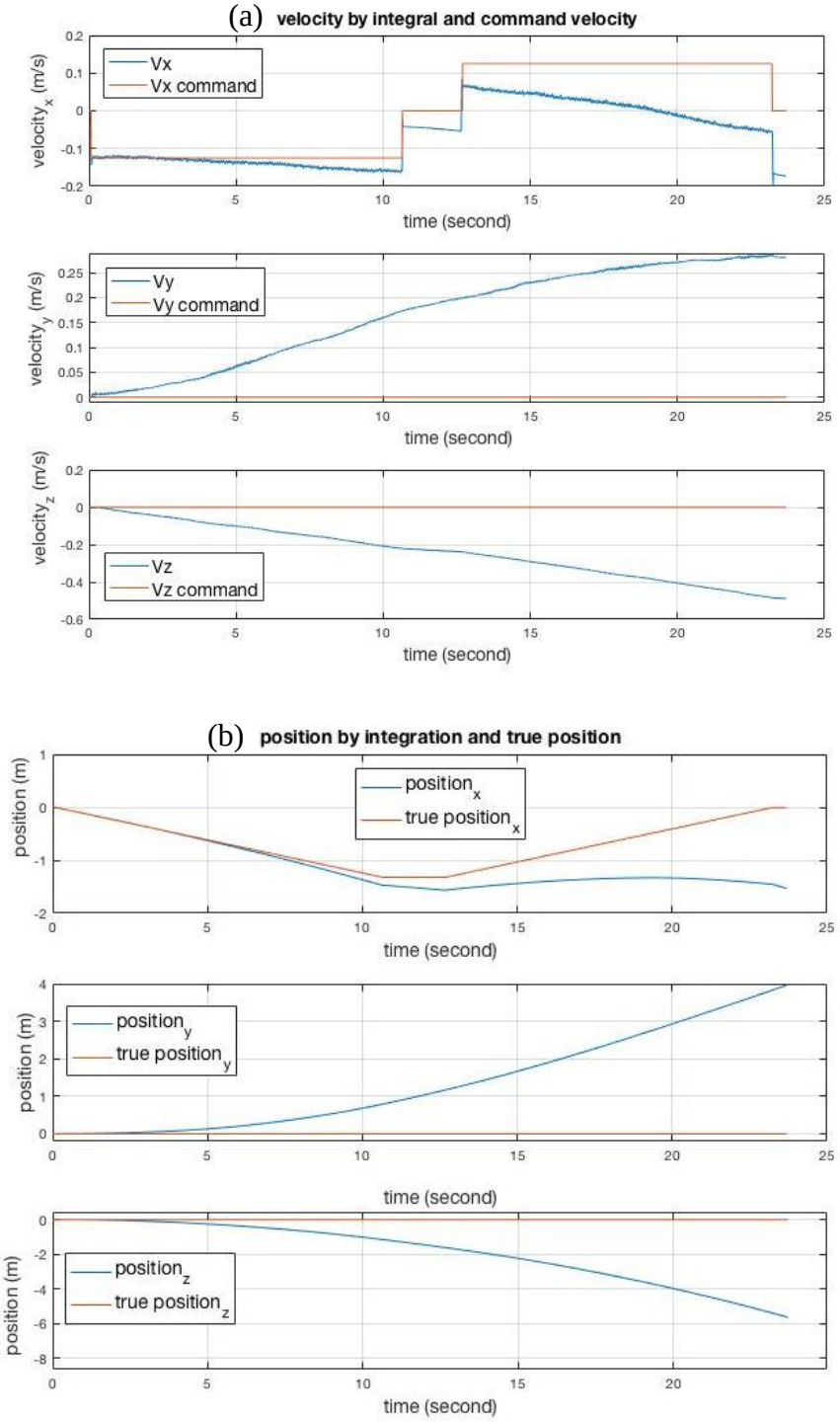

Figure 6.7 The comparsion of true values and experiment results (a). Comparison of the velocity calculated by acceleration in the global frame and the velocity calculated by stepper motor's command speed of experiment 1; (b). comparison of the position calculated by velocity in the global frame and the true position calculated by stepper motor's command speed

Experiment 2: This experiment is similar to Experiment 1 but now a global rotation of the path (about its longitudinal axis) is introduced during the motion. The speed of the IMU plate is set to be 0.125m/s and the plate moves forward 1.25m from point A to point B (as in Experiment 1 and as shown in Figure 6.4); while moving forward, the rail rotates about its center axis from 0 ° to 30°, and then back to 0° (as shown in Figure 6.8b and Figure 6.9) ; then the plate will stay at point B for 2 seconds; then the plate will travel back to point A at 0.125m/s and stop at point A with no further rotation of the rail.

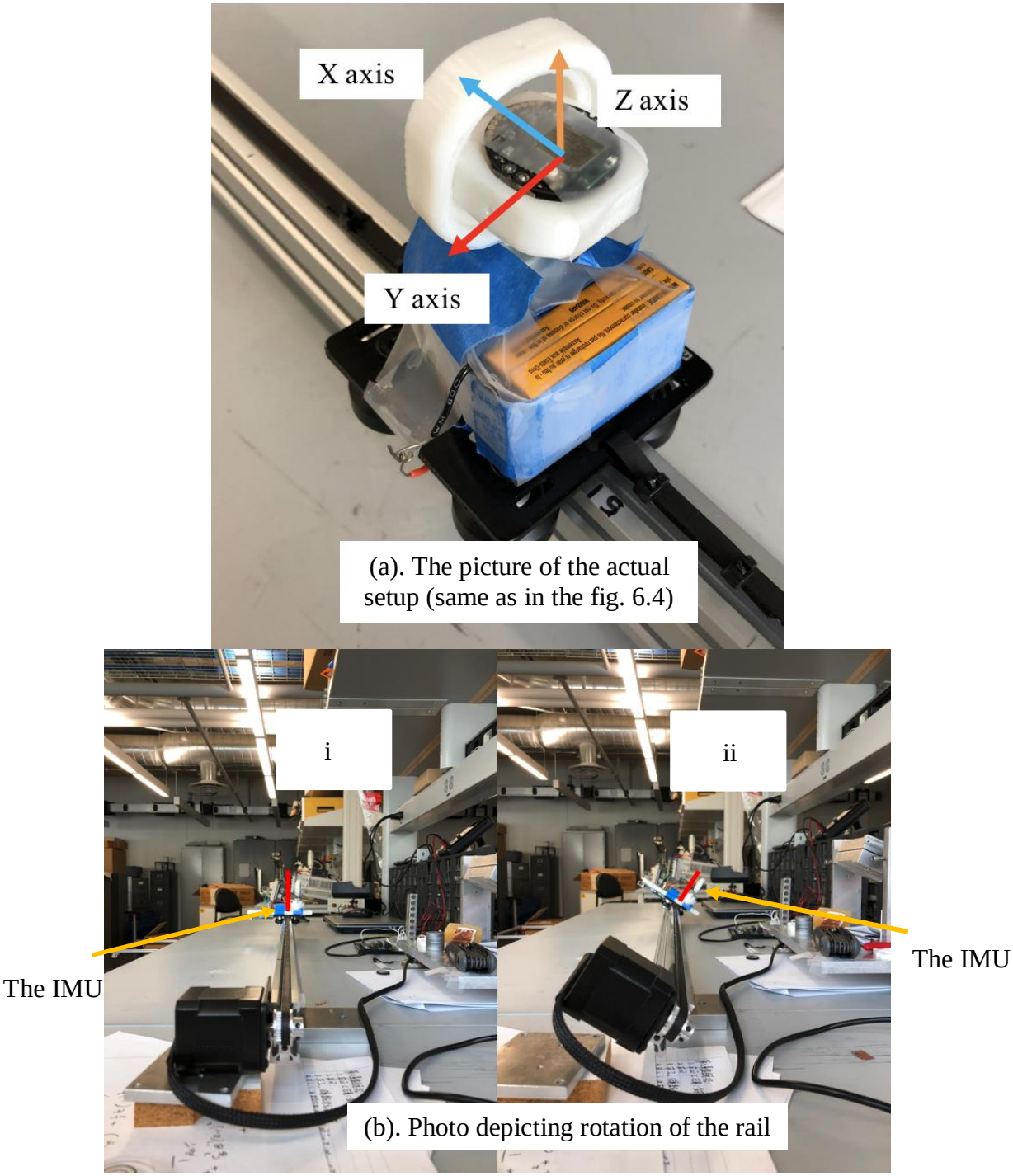

Figure 6.8 Photo of experiment 2 setup. a). The picture of actual setup with IMU body frame; b). Photo depicting rotation of the rail: (i) rotated 0 degree; (ii) rotated 30 degrees.

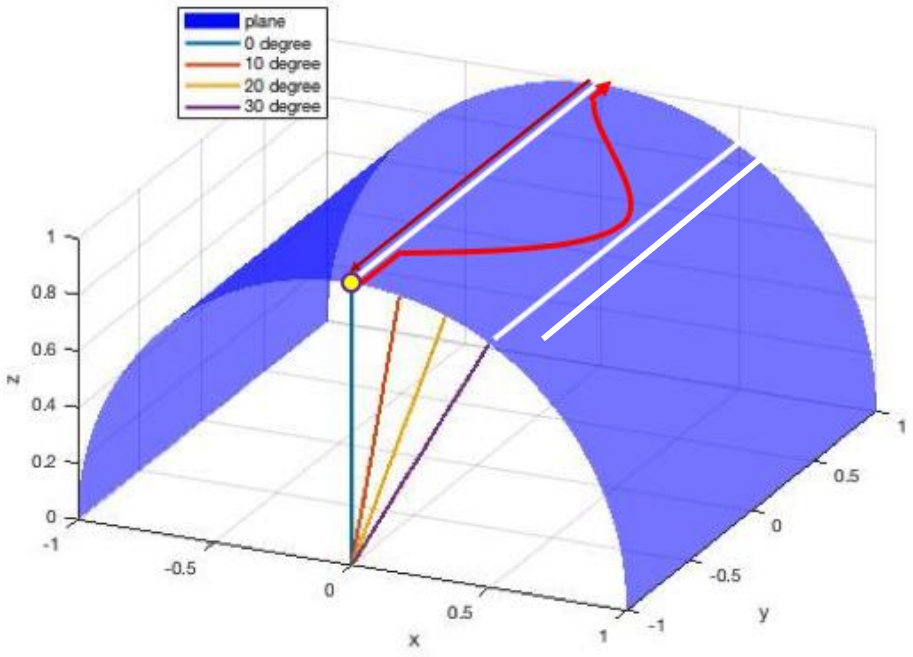

Figure 6.9 Sketch of the rotated trajectory of experiment 2. The original point is marked in yellow, trajectory is shown in red line.

The measured acceleration in three axes in the global frame is shown in Figure 6.10. As shown in Figure 6.11, the velocity result is similar to Experiment 1, where, as time increases, the error between calculated value and the designed (true) value increases. Command speed is only shown in X axis because the speed of Y and Z axis are manually controlled. The calculated trajectory is shown in Figure 6.12.

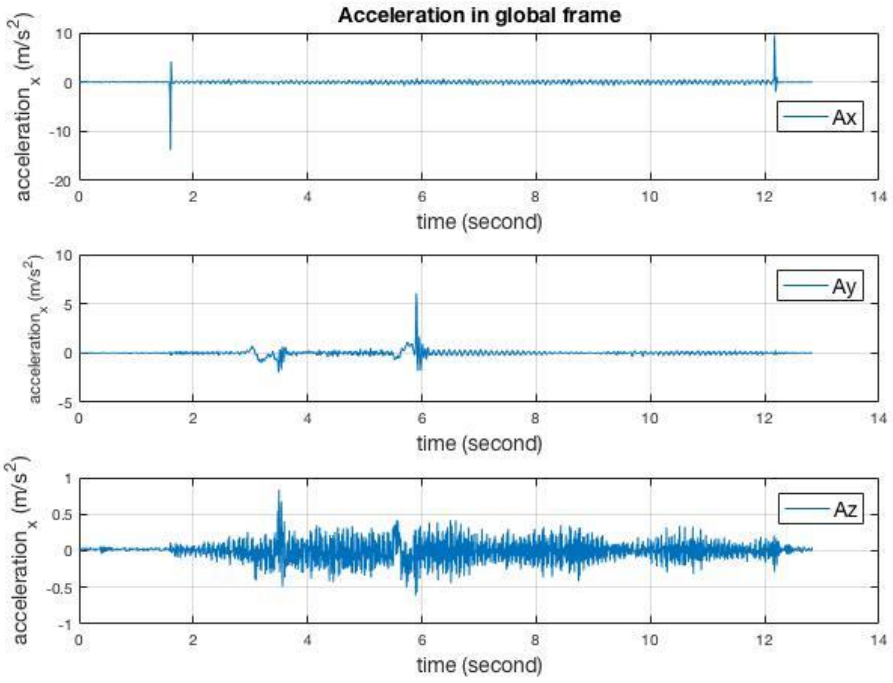

Figure 6.10 The acceleration of experiment 2 in global frame

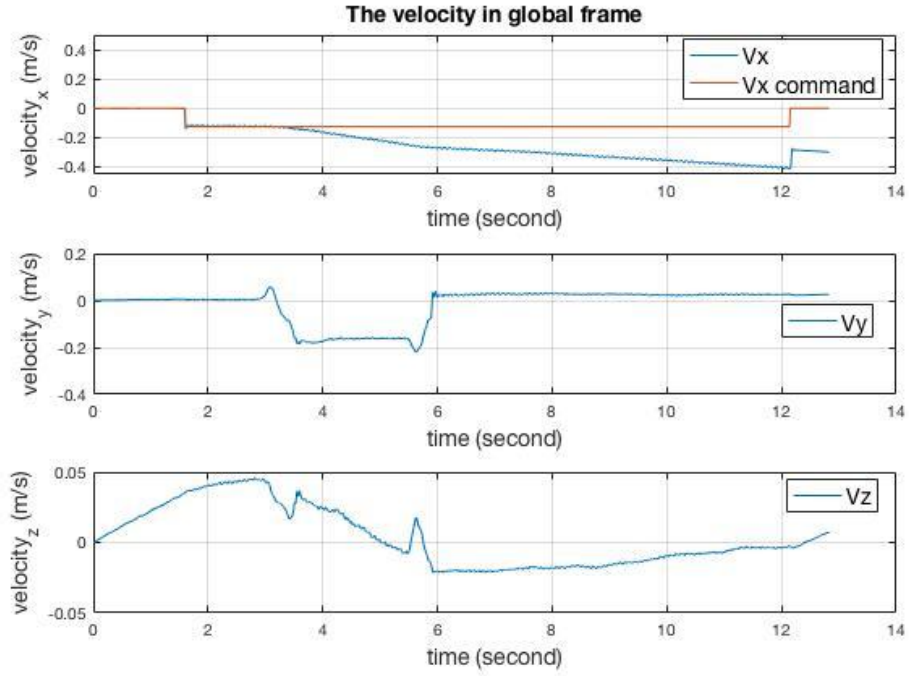

Figure 6.11 The velocity of experiment 2 in global frame

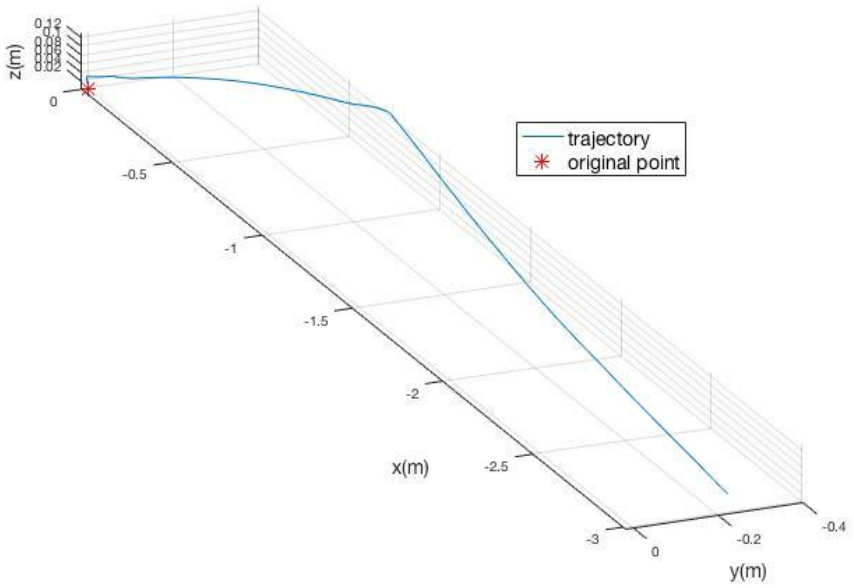

Figure 6.12 The oblique drawing of calculated trajectory of experiment 2

Experiment 3: This experiment is similar to Experiment 2 but now a body-fixed rotation is added to the IMU during the motion. The speed of the IMU plate is set to be 0.125m/s as it moves forward 1.25m from point A to point B (as in Experiment 1 and as shown in Figure 6.4); while moving forward, the rail rotates about its center axis from 0 ° to 30°, and then back to 0° (as in Experiment 2 and as shown in Figure 6.8 and Figure 6.9) ; then the plate will stay at point B for 2 seconds; then the plate will travel back to point A at 0.125m/s and stop at point A. As shown in Figure 6.13, during the whole motion, the IMU rotates about the X axis in the body frame at constant speed 2 rasd/s. Figure 6.14 shows a sketch of the trajectory. Because the rotation axis passes though the IMU's center, Figure 6.14 is actually the same as Figure 6.9.

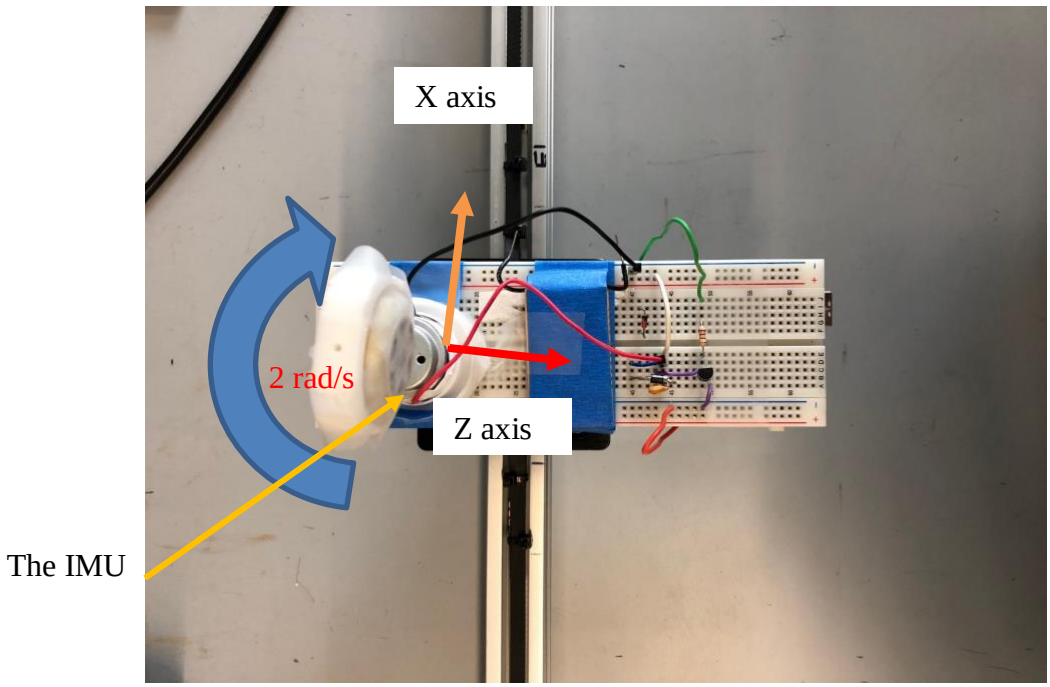

Figure 6.13 Photo of IMU mounted on motor-equipped plate to enable rotation about Z axis. The X and Z axis of IMU body frame is shown by orange and red arrow, respectively.

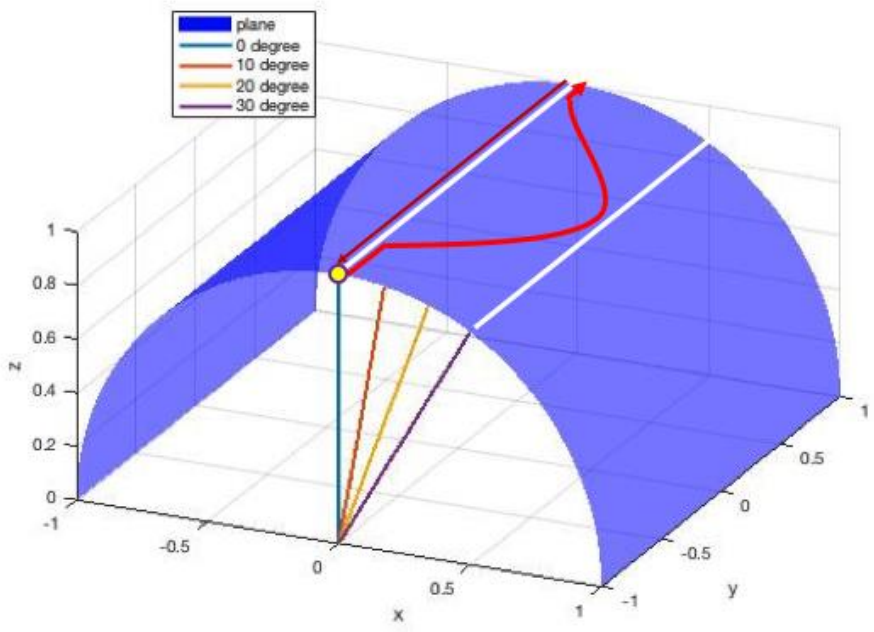

Figure 6.14 Sketch of the rotated trajectory of experiment 3. The original point is marked in yellow, trajectory is shown in red line

The measured acceleration in three axes in the global frame is shown in Figure 6.15. The results show that acceleration in X axis has a lot of noise, acceleration in Y and Z oscillate around 0. The oscillation might be because the IMU is not rotated about Z axis ideally, the rotation is actually decentered. The eccentric motion could cause IMU fluttering while moving.

By taking first-order integration, the velocity is shown in Figure 6.16. And the trajectory is shown in Figure 6.17. The trajectory drifts a lot. The displacement in the X-axis is almost 10m and 3m in the Z-axis, which shows great error.

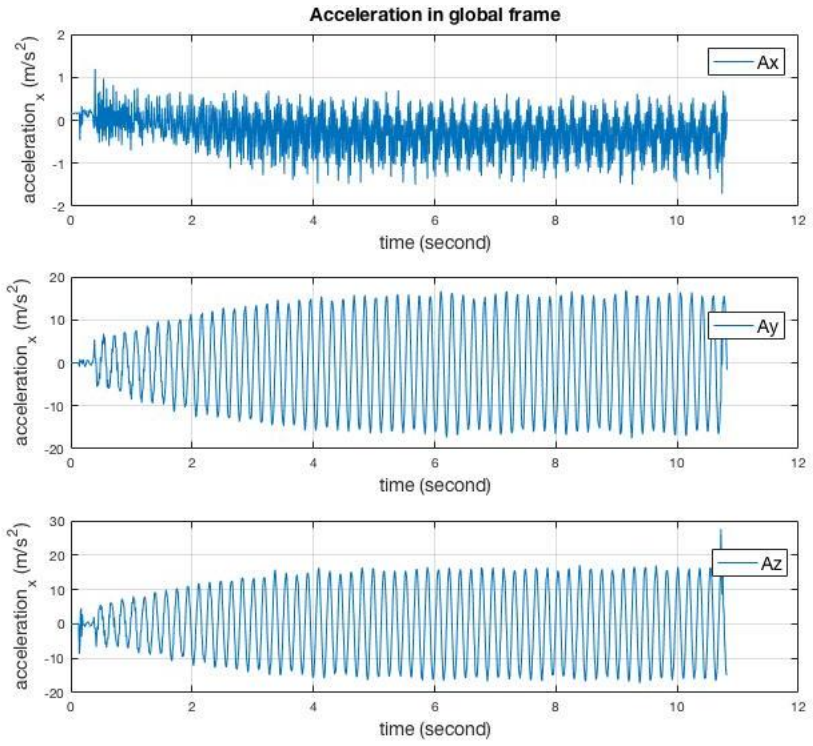

Figure 6.15 The acceleration of experiment 3 in global frame

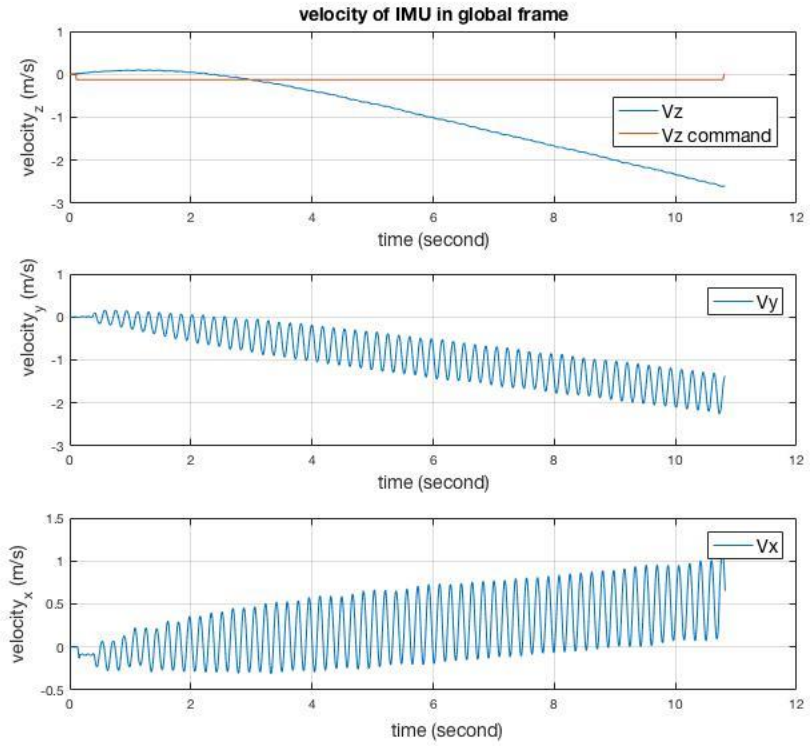

Figure 6.16 The velocity of experiment 3 in global frame

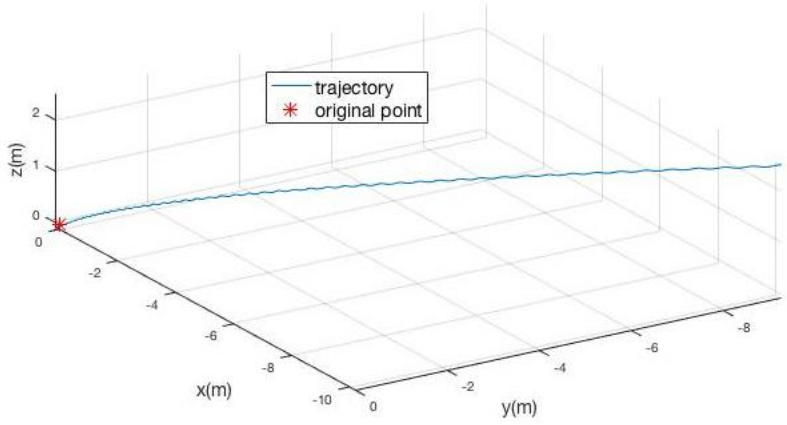

Figure 6.17 The oblique drawing of trajectory of experiment 3

6.3 CHAPTER CONCLUSIONS

In this chapter, the experimental methods of the simulated experiment were introduced. The brief summary of three scenarios is shown in Table 6.1.

Table 6.1 Summary of imitation experiment method

	Experiment 1	Experiment 2	Experiment 3
DOF	1	2	3
Description	IMU is moving straight along global X axis	IMU is yawing about global Y while moving straight along global X axis	IMU is rotating around global Z axis, yawing about global Y and moving straight along global X axis

Each experiment was conducted ten times and the average error of final position is listed in Table 6.2, and standard deviations are shown in parentheses. Those errors exist because the IMU is composed of dead-reckoning sensors, the error will accumulate with time. A close-loop feedback control system is needed to optimize the output, which is the ultimate purpose of this study.

Table 6.2 Final position error of three experiments

	X axis (m)	Y axis (m)	Z axis (m)
Experiment 1	0.002 (0.004)	0.010 (0.016)	0.086 (0.096)
Experiment 2	0.177 (0.087)	0.007 (0.003)	0.012 (0.540)
Experiment 3	0.102 (0.1435)	0.018 (0.001)	0.041 (0.011)

In the next chapter, a Bayes filter will be studied, and applied to optimize our trajectory algorithm.

7.0 BAYES FILTER

An IMU is composed of multiple dead-reckoning sensors, such as accelerometer and gyroscope. As mentioned in Chapter 2, the dead-reckoning sensors accumulate errors with time. The error will be magnified when integral operation is involved. For example, assuming the error is a constant signal, after first-order integration, the error of the result is a linear function of time; after second-order integration, the error of the result is a quadratic function of time, and so on.

In our case, acceleration data is used to calculate a trajectory by doing double integration, which will cause a large error for events that last more than a second. To better understand how Gaussian white noise and drift influence the result, a simulation was created. To conduct the simulation, a noise and drift model of acceleration is defined as:

$$\boldsymbol{a}_{simulation} = \boldsymbol{a}_{truth} + f_d(t) + noise \quad \textbf{(7-1)}$$

where a_{truth} is true acceleration; $f_d(t)$ is a drift function with respect to time (we treat it as a linear function: $f_d(t) = const \cdot t$); and *noise* is Gaussian white noise. First and second order integrals are applied to calculate velocity and position, respectively. The result is compared with the true acceleration.

Figure 6.7 shows how noise and drift affect the velocity and trajectory calculations. The ideal acceleration (assumed to be acceleration in the global frame) is drawn in red and is made up to be the acceleration that causes the sensor to move in a step-wise velocity pattern. The blue line is the simulated data, with noise included. Figure 7.1b shows the resulting calculated velocity,

which is the first integral of Figure 7.1a's data. Figure 7.1c is the trajectory, which is the result of second integral of Figure 7.1a's data. Figure 7.2 and Figure 7.3 show the influence of the result by noise and drift, respectively. It's noteworthy that the shape of result in Figure 7.1 is similar to Figure 6.7, which suggests that the cause of error in Figure 6.7 is noise and drift (or only noise) of the IMU measured acceleration. The error caused by drift cannot be reduced or eliminated by a filter in the frequency domain, such as a low-pass filter. Therefore, dead-reckoning sensors must be periodically reset by using extra information.

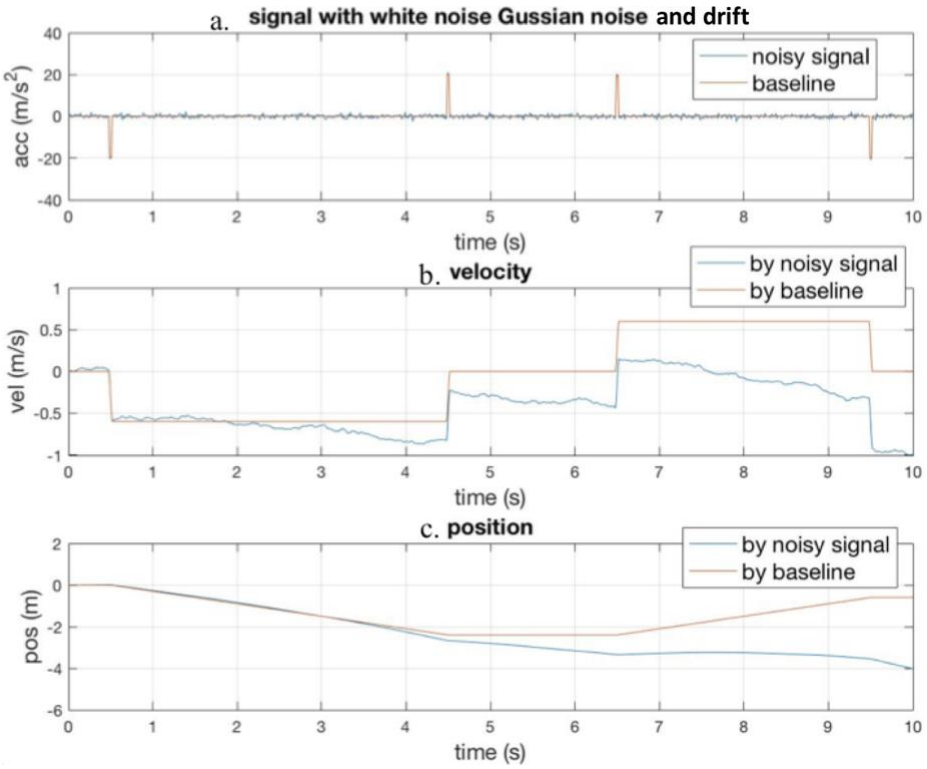

Figure 7.1 Noise and drift effects to trajectory reconstruction result

a. the red line is designed acceleration, the blue line is designed acceleration composed with noise and drift; b. red line is velocity from designed acceleration, blue line is velocity from noisy acceleration; c. red line is position from designed acceleration, blue line is position of noisy acceleration

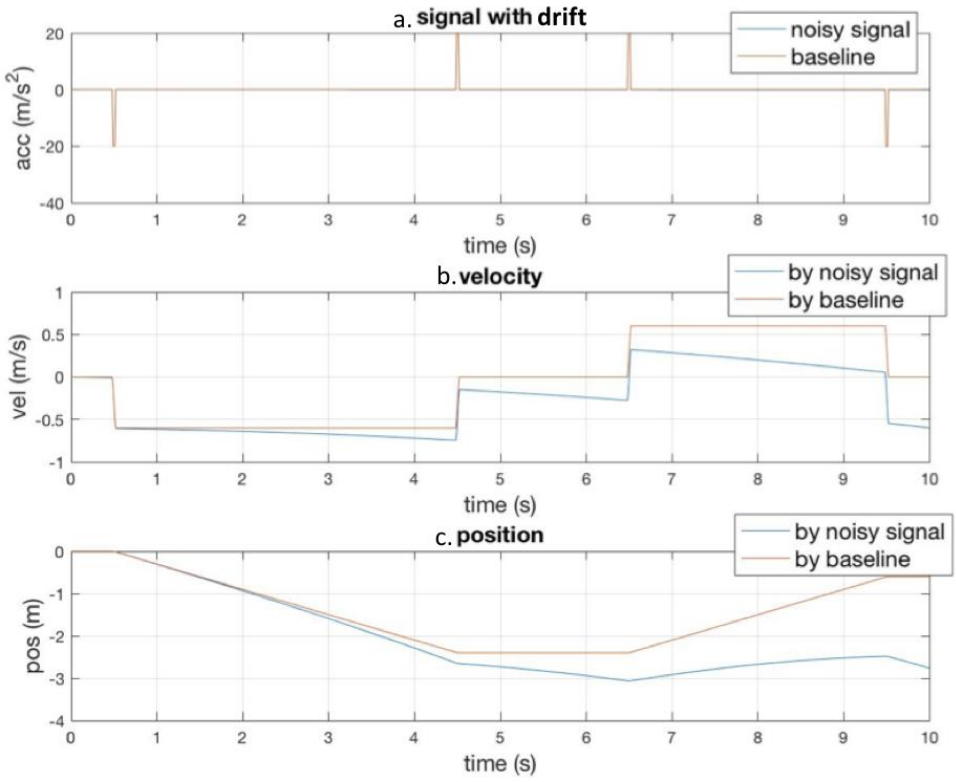

Figure 7.2 Drift effects on trajectory reconstruction result

a. the red line is designed acceleration, the blue line is designed acceleration composed with drift; b. red line is velocity from designed acceleration, blue line is velocity from drifted acceleration; c. red line is position from designed acceleration, blue line is position of drifted acceleration

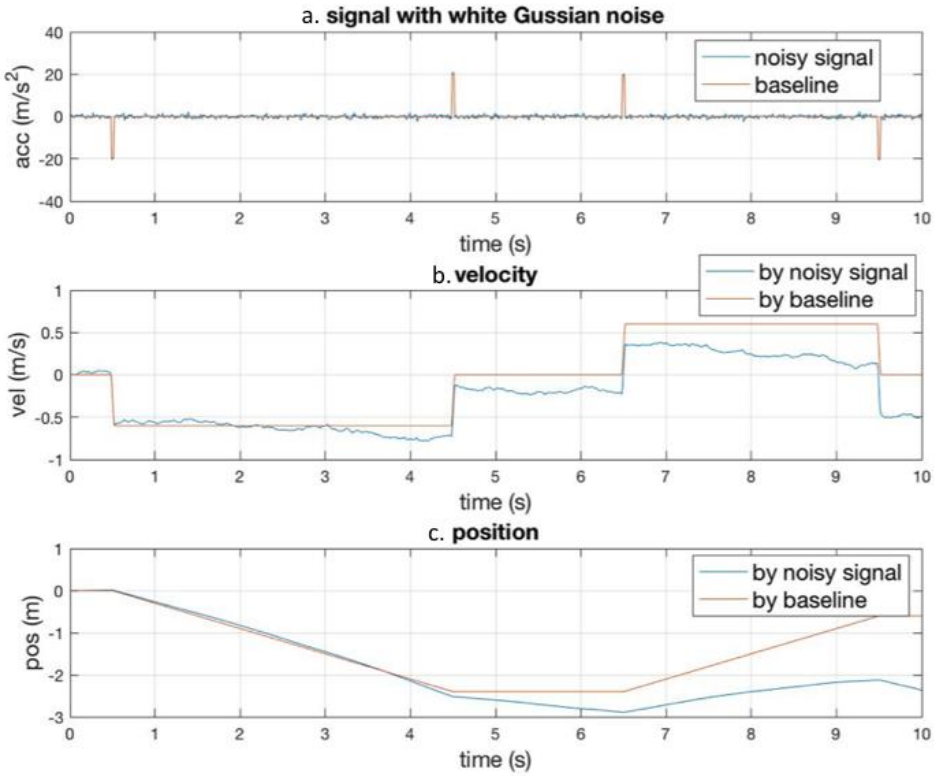

Figure 7.3 Noise effects on trajectory reconstruction result

a. the red line is designed acceleration, the blue line is designed acceleration composed with noise;

b. red line is velocity with designed acceleration, blue line is velocity with noisy acceleration;

c. red line is position with designed acceleration, blue line is position of noisy acceleration

According to other references, external sensors such as Global Positioning System (GPS) are widely used as correction data for dead reckoning systems (Zhang, Gu, Milios, & Huynh, 2005; Fakharian, Gustafsson, & Mehrfam, 2011). For example, Zhang et al. used position measurement as reference and compared with position calculated by IMU to calculate Kalman filter gain of the system. The trajectory result showed high accuracy when the Kalman filter was applied. Those works suggest that closed-loop feedback is able to compensate the result, which requires external information provided by another sensor. With extra information, the drawbacks of each sensor in the IMU are compensated, which provides more accurate state estimation. The next step of our work is to build a close-loop control system to compensate state vector and output results. Bayes

filters, such as the Kalman filter (KF) (S. H. P. Won, Golnaraghi, & Melek, 2009; Caron, Duflos, Pomorski, & Vanheeghe, 2006) and particle filters (PF) (S. Won, Melek, & Golnaraghi, 2010; Touil, Zribi, Choquel, & Benjelloun, 2007), are widely used as close-loop feedback systems according to previous works.

Therefore, in this paper, we take advantage of the Kalman filter (KF) algorithm to improve our trajectory algorithm.

7.1 EXTENDED KALMAN FILTER

The Kalman filter, also known as linear quadratic estimation, has long been used as an algorithm to find the best estimate of states by combining measurements from various sensors in the presence of noise. It is used as a filter in many cases since the states usually are noisy signals. The Kalman filter algorithm is popularly applied to IMUs (S. Won et al., 2010; Mirzaei & Roumeliotis, 2008). With Kalman filters, the noise and drift can be attenuated. The whole process can be demonstrated as KF structure shown in Figure 7.4. The Kalman filter can be divide into two parts: prediction step and correction step. In the prediction step, the state equation is used. The next state is predicted by the previous state. Then the predicted state is substituted into the measurement model and the gain is derived by comparing the output with the result measured by the sensor. The state is compensated by adjusting the gain.

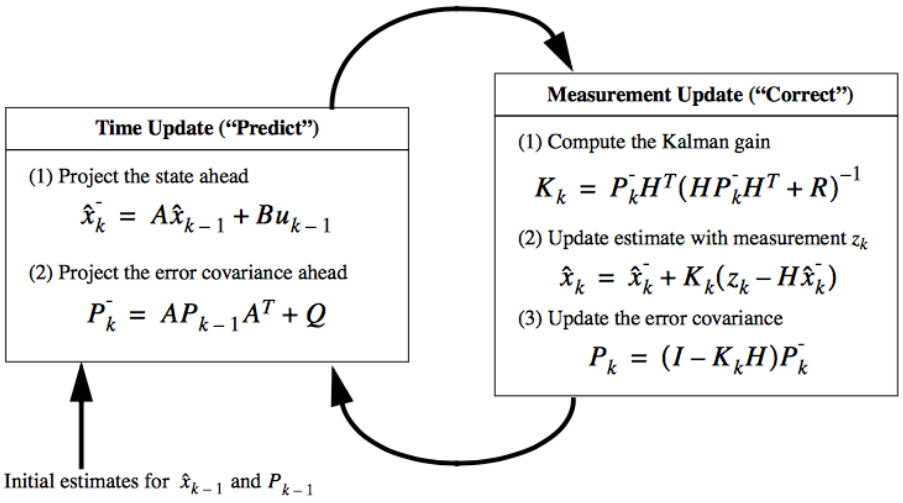

Figure 7.4 A complete picture of the operation of the Kalman filter (Welch & Bishop, 2006)

In this study, we introduce a new method to build a Kalman filter system. Because the IMU is moving inside a pipe system with particles undergoing pneumatic conveying, GPS signals are too weak to be used as they cannot penetrate the pipe and reach the IMU, and cameras can't be reliably used to locate the IMU's position. Furthermore, magnetic field is heavily perturbed (or disturbed) by surroundings, such as metal materials and electronic devices, so using magnetometers to correct the quaternions is not available for our case.

To do that, we present a novel way to detect position by magnetic field distribution, which will be introduced in the following section. Since the strength of magnetic field at certain points is a constant when the environment is stable, the strength of magnetic field could be used to detect the IMU's position. That position information can be detected by the IMU's magnetometer and compared with the trajectory result calculated by the algorithm we developed in Chapter 3. Then the correction step can be applied. However, because the measurement model is no longer linear, and the error distribution is no longer Gaussian, adjustments to the Kalman filter approach must be made. The state transition and observation models of the Kalman filter are required to be linear

functions. In order to make the Kalman filter valid for this non-linear system, extended Kalman filter is implemented.

Extended Kalman filter (EKF) is designed for non-linear state estimation. EKF linearizes the non-linear state function and measurement function locally by obtaining Jacobian matrices, which are used to predict and update the state.

7.1.1 The system model

For a recap (as mentioned in Chapter 3), there are two reference frames relative to IMU motion, which are the IMU frame and the observation frame. The observation frame is also called the global frame. All the sensors in an IMU make measurements in the IMU frame. The X axis of the global frame is aligned with the direction tangent to the primary section of pipe. The Z axis of the global frame is in the opposite direction to the gravity force. Both the IMU frame and global frame use a right-handed coordinate system.

7.1.1.1 Process State

We define a state vector x as follows:

$$\boldsymbol{x} = [\boldsymbol{q} \quad \boldsymbol{p} \quad \boldsymbol{v} \quad \boldsymbol{b}^{\boldsymbol{a}} \quad \boldsymbol{b}^{\boldsymbol{g}}]^{\mathbf{T}} \tag{7-2}$$

which is composed of the rotation quaternion $\boldsymbol{q}$, position $\boldsymbol{p}$, velocity $\boldsymbol{v}$, tri-axis accelerometer and gyroscope bias vectors $\boldsymbol{b}^{a}$ and $\boldsymbol{b}^{g}$, respectively. In our model, IMU biases are modeled as random walk processes driven by the zero-mean white Gaussian noise processes from acceleration and quaternion, n^a and n^q, respectively. The covariance matrix of n^a is ${}^{a}\Sigma_k = \Delta t^a \sigma_\omega^2$, where Δt^a is

the system sampling interval of accelerometer, σ_ω^2 is the covariance of Gaussian noise. The n^q is modeled as follows (Sabatini & Member, 2006):

$$n^q = -\frac{\Delta t}{2}\Xi^q v^q = -\frac{\Delta t^a}{2}\begin{bmatrix}[\vec{e}\times] + q_0\mathrm{I} \\ \vec{e}^{\mathrm{T}}\end{bmatrix} v^q \tag{7-3}$$

where v^q is white Gaussian measurement noise.

The state equation is:

$$\dot{x} = \begin{bmatrix}\dot{\boldsymbol{q}} \\ \dot{\boldsymbol{p}} \\ \dot{\boldsymbol{v}} \\ \dot{\boldsymbol{b}}^a \\ \dot{\boldsymbol{b}}^q\end{bmatrix} = \begin{pmatrix}\Omega(t)\cdot\boldsymbol{q} + \boldsymbol{n}^q \\ \boldsymbol{v} \\ R_{imu}^{global}\tilde{\boldsymbol{a}}^b - \boldsymbol{g} + \boldsymbol{n}^a \\ \boldsymbol{n}^a \\ \boldsymbol{n}^q\end{pmatrix} \tag{7-4}$$

In Eq. (7-4), $\Omega(t)$ is the same as in Eq. (4-21); R_{imu}^{global} is the rotation matrix which transfers coordinates from the IMU frame to the global frame; $\tilde{a}^b$ is the acceleration in the IMU frame, which is defined as:

$$\tilde{a}^b = a^m - b^a \tag{7-5}$$

where a^m is acceleration measurement from IMU, and b^a is the bias of the accelerometer.

The state transition vector equation is:

$$\begin{bmatrix}\boldsymbol{q}(k+1) \\ \boldsymbol{p}(k+1) \\ \boldsymbol{v}(k+1) \\ \boldsymbol{b}^a \\ \boldsymbol{b}^q\end{bmatrix} = \Phi(\Omega(t),\Delta t)\begin{bmatrix}\boldsymbol{q} \\ \boldsymbol{p} \\ \boldsymbol{v} \\ \boldsymbol{b}^a \\ \boldsymbol{b}^q\end{bmatrix} + G\begin{bmatrix}\boldsymbol{a} \\ \boldsymbol{g} \\ \boldsymbol{n}^a \\ \boldsymbol{n}^q\end{bmatrix} \tag{7-6}$$

where $\Phi(\Omega(t),\Delta t) = \begin{pmatrix} e^{\frac{1}{2}\Omega\cdot\Delta t} & 0 & 0 & 0 & e^{\frac{1}{2}\Omega\cdot\Delta t} \\ 0 & \mathrm{I} & \mathrm{I}\cdot\Delta t & R_{imu}^{global}\cdot\frac{\Delta t^2}{2} & 0 \\ 0 & 0 & \mathrm{I} & R_{imu}^{global}\cdot\Delta t & 0 \\ 0 & 0 & 0 & \mathrm{I} & 0 \\ 0 & 0 & 0 & 0 & \mathrm{I} \end{pmatrix}$,

$$G_c = \begin{pmatrix} 0 & 0 & 0 & e^{\frac{1}{2}\Omega\cdot\Delta t} \\ R_{imu}^{global}\cdot\frac{\Delta t^2}{4} & -\mathrm{I}\cdot\frac{\Delta t^2}{2} & R_{imu}^{global}\cdot\frac{\Delta t^2}{2} & 0 \\ R_{imu}^{global}\cdot\frac{\Delta t}{2} & -\mathrm{I}\cdot\Delta t & R_{imu}^{global}\cdot\mathrm{I}\cdot\Delta t & 0 \\ 0 & 0 & \mathrm{I} & 0 \\ 0 & 0 & 0 & \mathrm{I} \end{pmatrix}.$$

Then the *a priori state estimate* is expressed as:

$$\vec{x}_{k+1}^{-} = \Phi(\Omega(t), \Delta t)\vec{x}_k + G_c u \tag{7-7}$$

where $u = [a\ g\ n^a\ n^q]^{\mathrm{T}}$.

The process noise covariance matrix Q_d will have the following expression:

$$Q_d = \Phi(\Omega(t), \Delta t)G_c Q_c {G_c}^{\mathrm{T}}\Phi(\Omega(t), \Delta t)^{\mathrm{T}} \tag{7-8}$$

where Q_c is the covariance of system noise and depends on IMU noise characteristics.

The *a priori error covariance* matrix is then expressed as shown in Eq. (7-9):

$$P_{k+1|k}^{-} = \Phi(\Omega(t), \Delta t)P_{k|k}\Phi(\Omega(t), \Delta t)^{\mathrm{T}} + Q_d \tag{7-9}$$

7.1.1.2 Measurement State

Measurement method

In order to find the reference information, we developed a new method to detect position of the IMU. The magnetometer calibration is conducted by the method shown in Appendix A.3.

As shown in Figure 7.5, a series of magnets are placed under the belt and inside the slot.

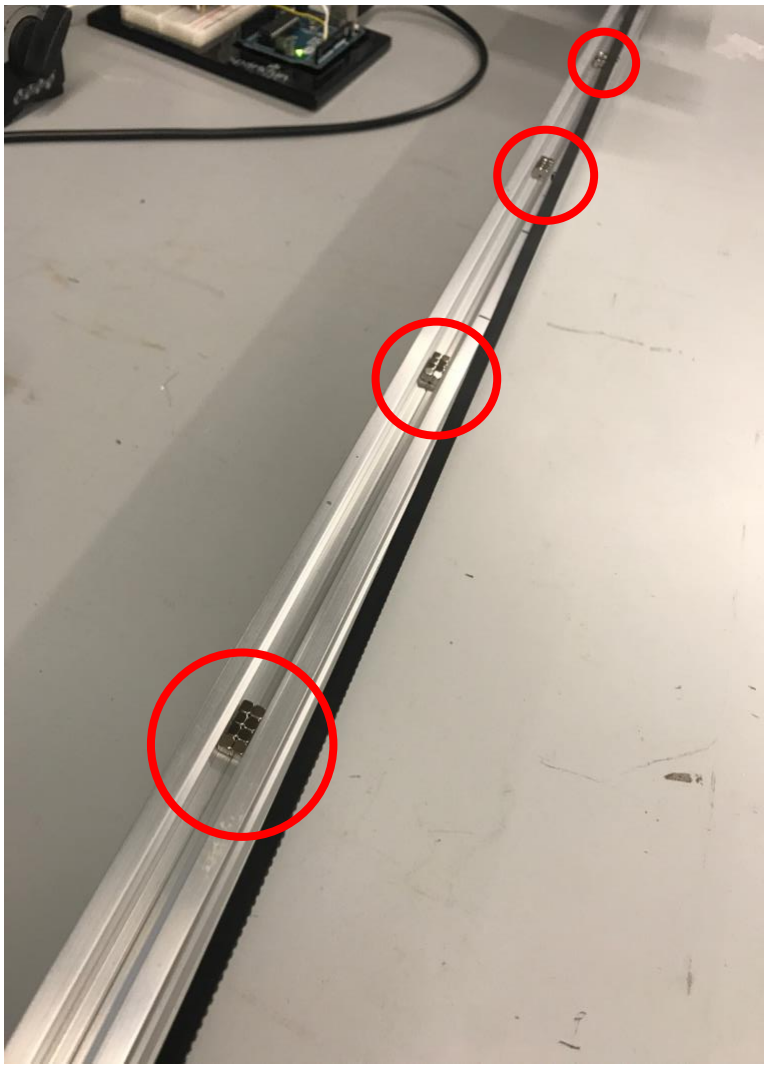

Figure 7.5 Magnets are placed along the rail, marked with red circles. There are 8 magnets at each location and they are installed evenly inside the slot, the distance between each of them is 0.16m.

As the IMU is moved past the magnets, the strength of magnetic field is obtained by the magnetometer. An example result is shown in Figure 7.6. Intuitively we know that when the magnetometer passes a pole of a magnet, there will be a peak appearing in the measured magnetic field magnitude. In the experiment, two separates IMU motions are captured: 1. the IMU moves in constant speed controlled by the stepper motor; 2. the IMU moves at variable speed controlled manually (in each case the IMU is moved only in one direction). The magnetic field strength of

constant speed motion (blue) is shown in Figure 7.6a, while the variable speed case is shown in red. Since the sample frequency is higher than the frequency of the passing peaks, the number of peaks captured is the same in each case (Figure 7.6a). The captured peaks are used to divide the magnetic field into multiple sections, which provide a lot of insight for the next step.

As shown in Figure 7.6a, the characteristic of the blue line is captured and matched with the characteristic of red line. For example, the peak point α in the blue line is considered matching with the peak point α' in red; the bottom point β in blue is considered to be matching with the bottom point β' in red. In 1476 sample points, 82 of them can be paired, which indicates that there are 41 pairs of matching points. The position of the red line can be synchronized in time and position, since the sensor is moved at constant speed in this case. Therefore, every point of stepper-controlled position is defined in both time and space. The position of the 41 paired points from the variable speed motion (red) have the same position as their stepper-controlled counterparts (blue). The remaining positions are obtained by linear interpolation method. As a result, the positions can be plotted as shown in Figure 7.6a, where the red line is a result of manual control, and the blue line is controlled by stepper motor.

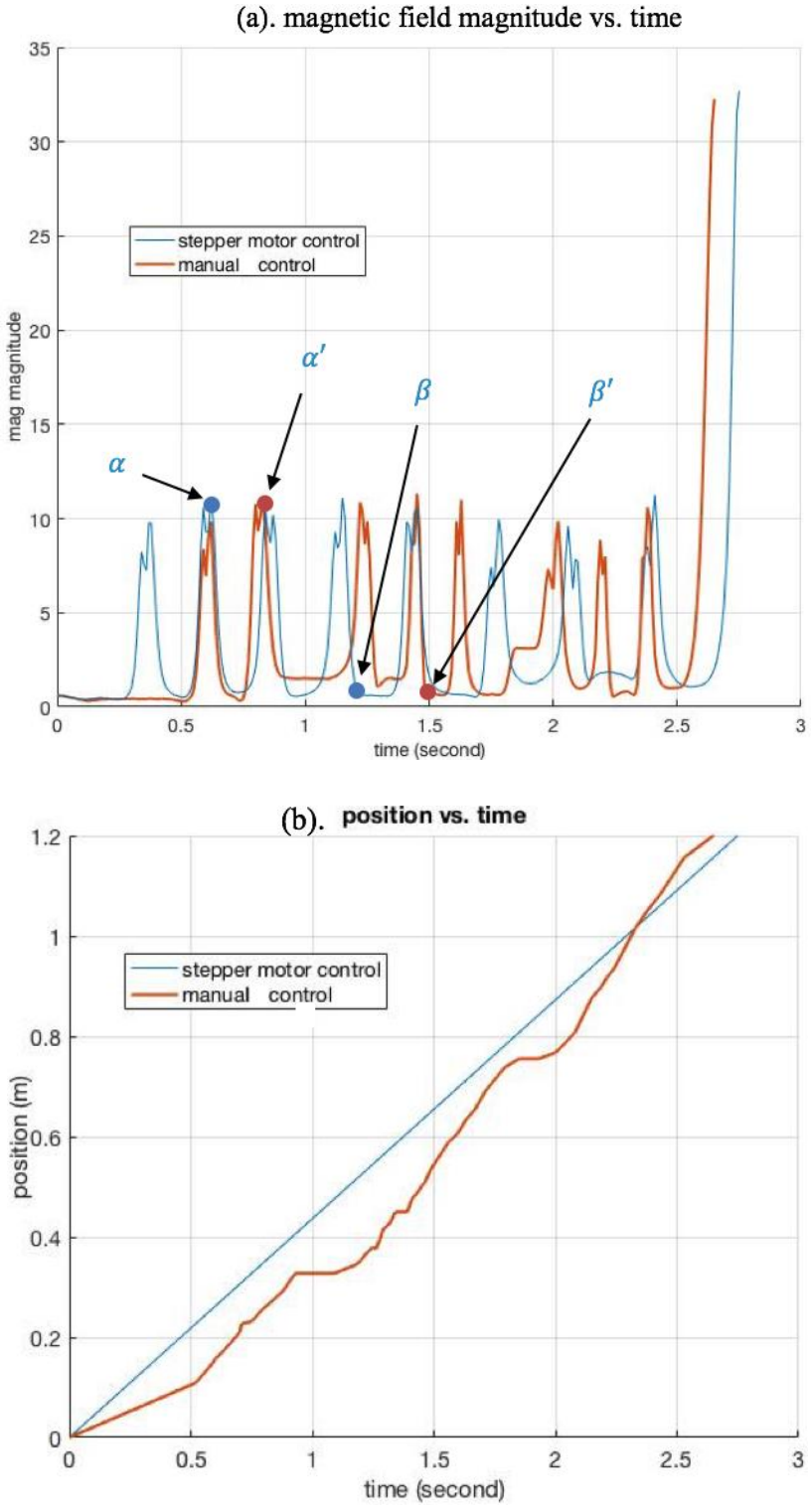

Figure 7.6 position detection method (a). magnetic field magnitude vs. time, the red line is manually controlled, and the blue line is controlled by stepper;

(b). position vs. time, the red line is manually controlled, and the blue line is controlled by stepper.

Measurement model:

The position and magnetic disturbance can be written as the function:

$$p_m = f(m) + \Psi \tag{7-10}$$

where $f(m)$ is a piecewise function; and Ψ is the error of estimating position by applying function $f(m)$. From Eq. (7-10) the measurement model z is described as:

$$z_k = p_m \tag{7-11}$$

The Jacobian matrix for the measurement vector is then computed as:

$$F_{k+1} = \frac{\partial}{\partial \vec{x}_{k+1}} z_{k+1}|_{\vec{x}_{k+1}=\vec{x}_{k+1}^-} = [0_{4\times3}\ \mathrm{I}_{3\times3}\ 0_{10\times3}]^{\mathrm{T}} \tag{7-12}$$

The covariance matrix of the measurement model R_{k+1} is:

$$R_{k+1} = \sigma_p^2 \mathbf{I} \tag{7-13}$$

The Kalman gain is computed as:

$$K_{K+1} = \frac{P_{k+1}^- F_{k+1}^{\mathrm{T}}}{F_{k+1} P_{k+1}^- F_{k+1}^{\mathrm{T}} + R_{k+1}} \tag{7-14}$$

The *a posteriori error state* is written as:

$$\vec{x}_{k+1} = \vec{x}_{k+1}^- + K_{K+1}[z_{k+1} - F_{k+1} x_k] \tag{7-15}$$

The *a posteriori error* covariance matrix is then computed as:

$$P_{k+1} = P_{k+1}^- - K_{K+1} F_{k+1} P_{k+1}^- \tag{7-16}$$

7.1.2 Computer simulation

For the purpose of algorithm testing, the motion data is collected from the IMU when it is moved by the linear actuator. The sampling frequencies of the accelerometer, gyroscope and magnetometer are 100Hz, 100Hz and 25Hz, respectively. The sensed gravitational field $\boldsymbol{g} = [0\ 0\ g]^{\mathrm{T}}$, in which g is assumed to be 9.81 m/s. The magnetometer is calibrated and normalized using the method introduced in Appendix A.3. The filter parameters are listed in Table 7.1. The covariance has been optimized by experimentation. The result of Q_c is computed offline.

Table 7.1 Parameters for the Kalman filter.

σ_ω	σ_a	σ_{ba}	$\sigma_{b\omega}$	σ_p	σ_g
0.001m/s^2	0.01m/s^2	0.001m/s^2	0.001rad/s	0.1mm	0.01rad/s

The outline of the complete algorithm is shown in Figure 7.7. First all sensors are calibrated, then the prior static attitude is estimated from static accelerometer's data. The prior static attitude is then used with gyroscope to get initial rotation matrices. The quaternion is applied here. The acceleration in the IMU frame is transferred to the global frame for all data points and gravity is subtracted to determine the dynamic acceleration, which is integrated to find IMU velocity and position. The information of acceleration in the global frame, as well as the calculated velocity and position results are used as inputs to the Kalman filter. The location detected by using the magnetometer is applied as a comparison signal. The output of the Kalman filter is the compensated position, velocity and acceleration.

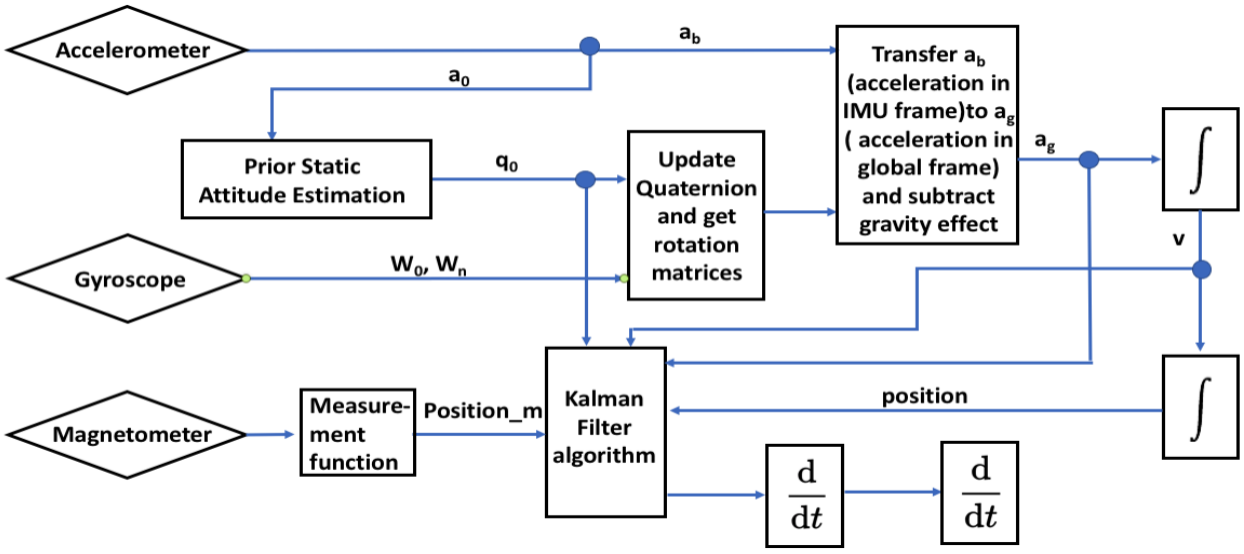

Figure 7.7 The outline of trajectory reconstruction algorithm: a_b is acceleration in the IMU frame; a_0 is acceleration in stable state; q_0 is initial quaternion element; w_0 and w_n are initial angular velocity and motion angular velocity.

7.1.3 Results and discussion

The Kalman filter algorithm validation is carried out by running the three groups of imitation experiments introduced in Chapter 4. The difference from Chapter 4 is that the motion here is only from point A to point B. As the truth reference, the length of total displacement is used. The coordinates of the start and end points are [0, 0, 0] and [-1.250, 0, 0], respectively. After the trajectory result is compensated, first-order differentiation is applied to find velocity and second-order differentiation is applied to find acceleration. The accelerations derived from Chapter 4 are used to compare with the accelerations we derived in this chapter by second-order differential.

7.1.3.1 Experiment 1

The trajectory result is shown in Figure 7.8. The trajectory without Kalman filter shows large error at the end point, which is [-1.070m, -0.045m, -0.502m]. The end point with Kalman filter is [-1.208m, 0.010m, -0.086m], which almost matches [-1.250m, 0,0]. The error with Kalman filter is [0.008m, 0.010m, 0.086m], while without Kalman filter is [0.180m, 0.045m, 0.502m].

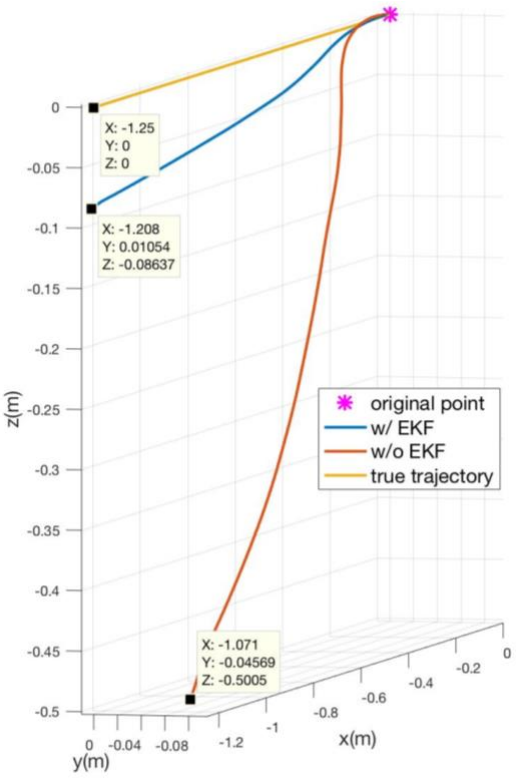

Figure 7.8 Trajectory comparison between Kalman filtered and base trajectory algorithm.

Figure 7.9 shows the global acceleration with and without Kalman filter. It shows that without Kalman filter, the signal is noisier. In the X axis data, there are two inverse peaks as shown in the plot. After applying Kalman filter, those two inverse peaks largely disappear, which is more accurate. In addition, it is notable that the end portion of acceleration in the Y axis almost becomes zero when the Kalman filter is applied.

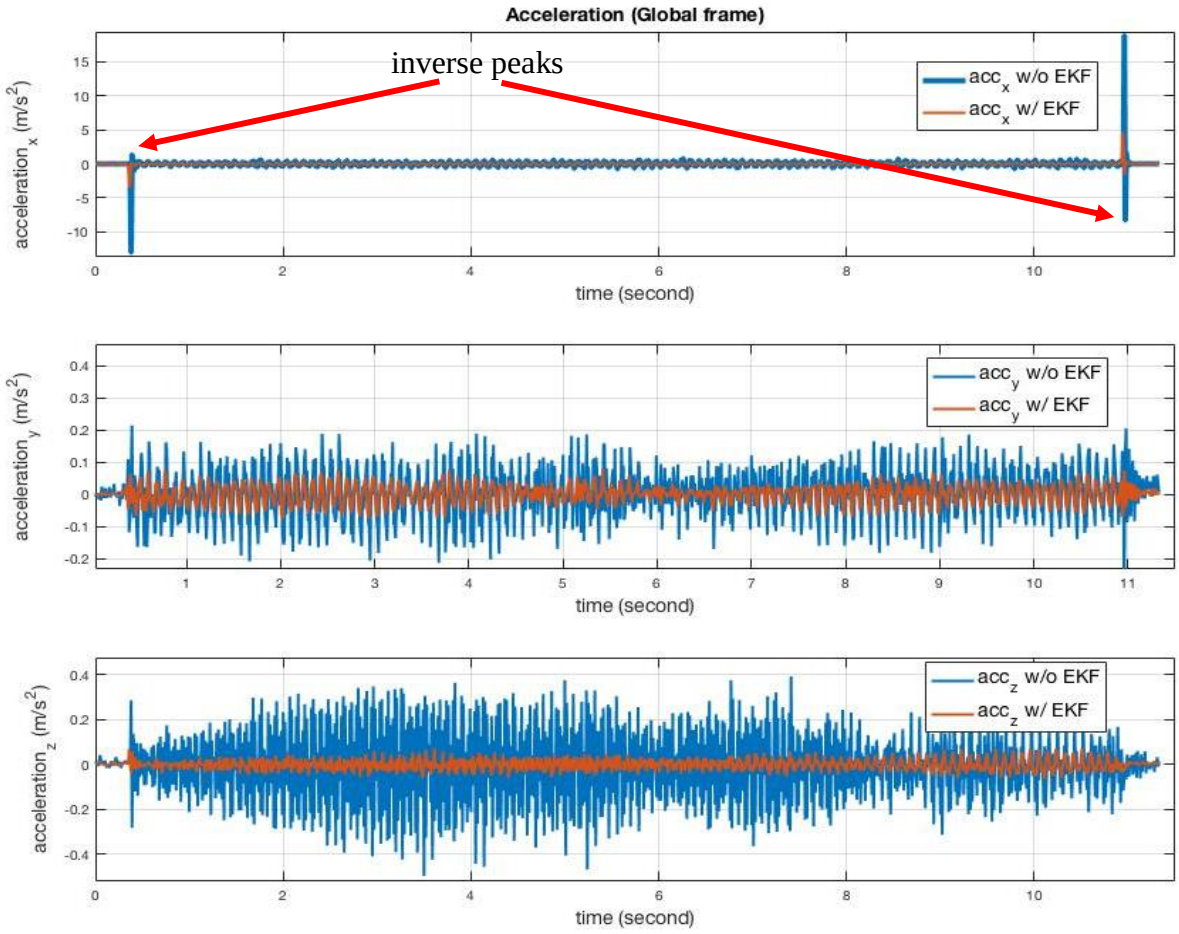

Figure 7.9 Comparison of global frame acceleration comparison between w/ and w/o Kalman filter.

7.1.3.2 Experiment 2

Similar to the results for Experiment 1, the trajectory results for Experiment 2 are shown in Figure 7.10. The trajectory without Kalman filter shows large error at the end point, with coordinates at [-2.482m, -0.279m, -0.050m]. The end point coordinates with Kalman filter are [-1.375m, -0.007m, -0.013m], which are much closer to [-1.250m, 0,0]. The error with Kalman filter is [0.125m, 0.007m, 0.013m], while without Kalman filter is [1.232m, 0.279m, 0.050m].

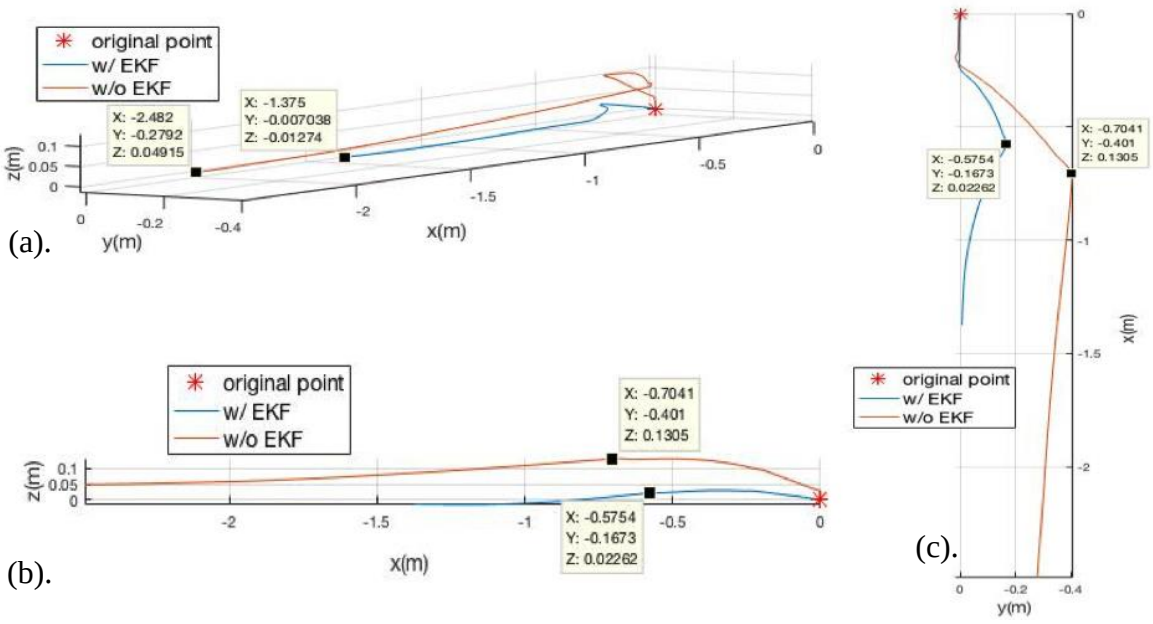

Figure 7.10 Comparison of trajectory w/ and w/o Kalman filter.

(a). oblique drawing; (b). lateral view; (c). top view. The black points in oblique drawing are terminal points of w/ and w/o Kalman filter; the black points in lateral and top views represent the location when maximum roll angle is reached.

Because the linear movement is combined with rotation in Experiment 2, there are displacements in the Y and Z directions. The geometrical sketch of a cross-section of the trajectory is shown in Figure 7.11.

The lengths of b and c are the true values of displacement when the roll angle is 30˚, which in the Y axis should be 0.09m and in the Z axis should be 0.0241m, as shown in expression below. $b = \left(1 - cos\left(\frac{\mu}{6}\right)\right) \cdot a = 2.41cm$, and $c = sin\left(\frac{\mu}{6}\right) \cdot a = 9cm$

The calculated displacement in the Y axis is 0.167m with the Kalman filter while it is 0.401m without the Kalman filter; and the calculated displacement in the Z axis is 0.023m with the Kalman filter while it is 0.131m without the Kalman filter.

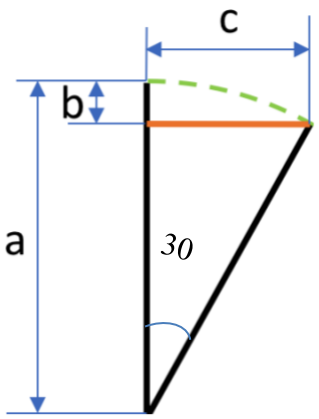

Figure 7.11 Geometrical sketch of cross-section of trajectory for Experiment 2. The black line represents the distance from the IMU to the center of rotation, where a=18cm.

b is calculated by $\mathbf{b} = \left(\mathbf{1} - \mathbf{cos}\left(\frac{\mu}{6}\right)\right) \cdot \mathbf{a} = \mathbf{2.41}\boldsymbol{cm}$,and $\mathbf{c} = \mathbf{sin}\left(\frac{\mu}{6}\right) \cdot \mathbf{a} = \mathbf{9}\boldsymbol{cm}$

Figure 7.12 shows the global acceleration comparison between trajectory calculated using the base algorithm and the trajectory calculated using the Kalman filter. The noisy signal is filtered by the algorithm and the signal is much smoother.

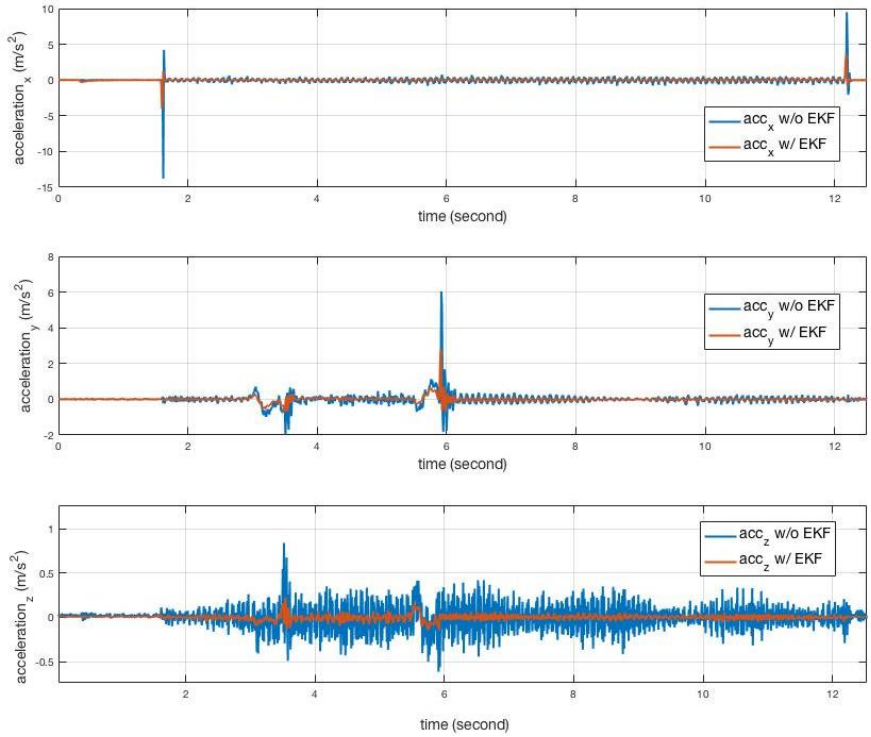

Figure 7.12 The global acceleration comparison between data w/ and w/o Kalman filter

7.1.3.3 Experiment 3

As shown in Figure 7.13, after the Kalman filter is applied, the magnitude of noise in the X direction is attenuated, and the amplitude of oscillation in Y and Z directions are also decreased. As a result, the velocity in Figure 7.14 is more accurate. The trajectory results for Experiment 3 are shown in Figure 7.15. The trajectory without Kalman filter shows large error at the end point, with coordinates at [-10.200m, -9.261m, 2.516m]. The end point coordinates with Kalman filter are [-1.342m, -0.017m, 0.033m], which are much closer to [-1.250m, 0,0]. The error with Kalman filter is [0.092m, 0.017m, 0.033m], while without Kalman filter is [8.950m, 9.261m, 2.516m]. In Figure 7.15, the result of trajectory with the Kalman filter is much better than before. Multiple circles are shown in Figure 7.15c. Those circles support the assumption we made before, the IMU is not rotated about Z axis (global frame) but doing eccentric motion. The peak displacement caused by roll is [0.017m,0.026m]. Comparing with theoretical displacement [0.024m,0.09m], the error is [0.007m,0.017m]. However, the error is relatively small compared to the result without Kalman filter.

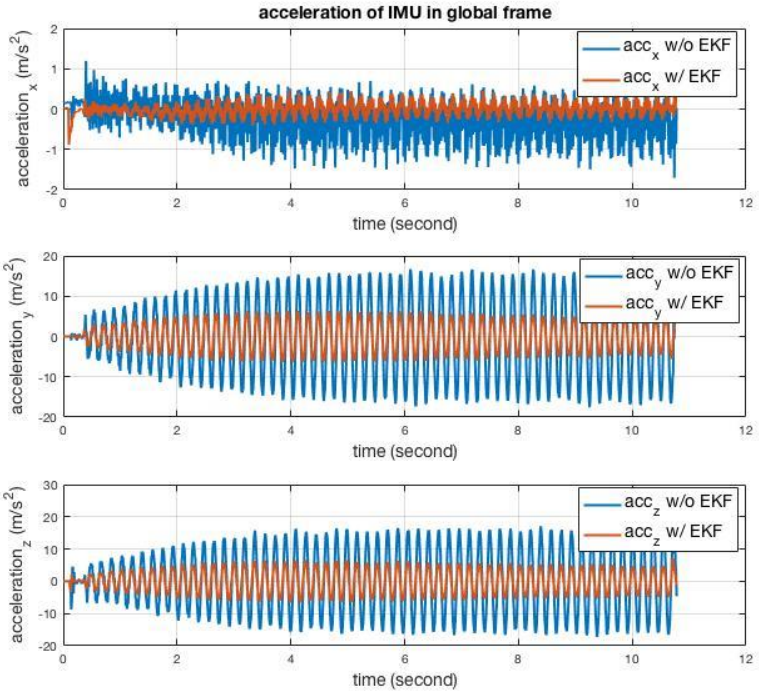

Figure 7.13 Comparison of global frame acceleration comparison between w/ and w/o Kalman filter.

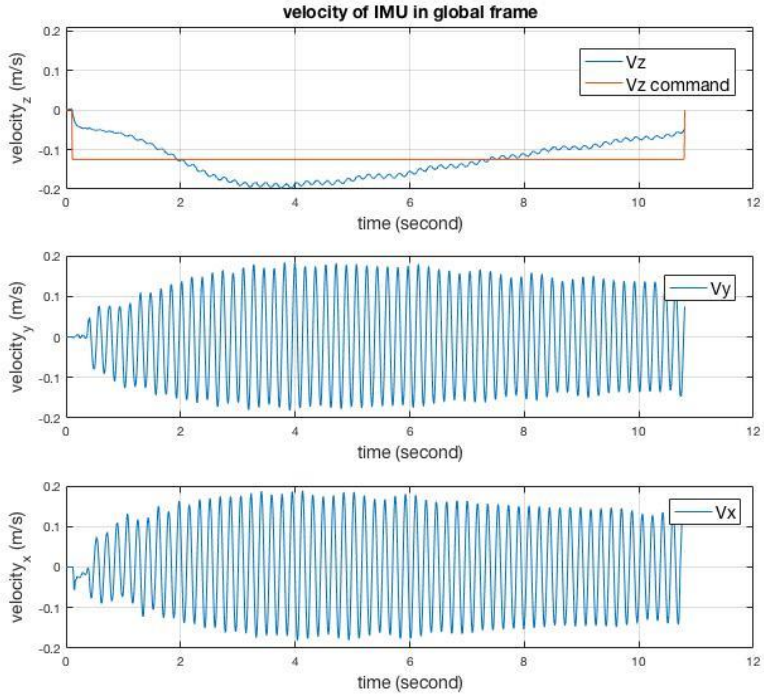

Figure 7.14 velocity in global frame w/ Kalman filter.

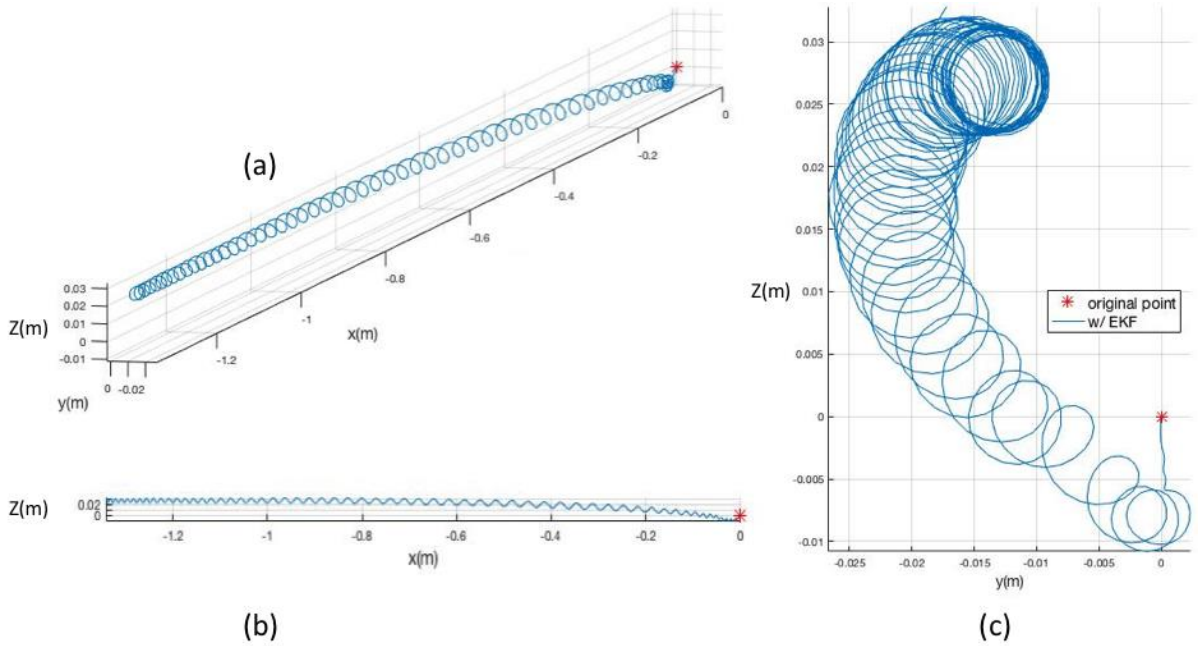

Figure 7.15 Comparison of trajectory w/ Kalman filter.

(a). oblique drawing; (b). top view; (c). lateral view.

7.1.3.4 Overall of Results

Each experiment was conducted ten times and the average error of final position is listed in Table 7.2. The standard deviation of error in each axis is shown in parentheses.

Table 7.2 Final position error comparison

	X axis (m)		Y axis (m)		Z axis (m)	
	w/ KF	w/o KF	w/ KF	w/o KF	w/ KF	w/o KF
Experiment 1	0.002 (0.004)	0.188 (0.015)	0.010 (0.016)	0.044 (0.063)	0.086 (0.096)	0.502 (0.781)
Experiment 2	0.177 (0.087)	1.225 (0.197)	0.007 (0.003)	0.279 (0.099)	0.012 (0.540)	0.050 (0.021)
Experiment 3	0.102 (0.1435)	11.201 (3.183)	0.018 (0.001)	10.895 (2.311)	0.041 (0.011)	2.645 (0.182)

7.2 CONCLUSION OF EKF TEST RESULTS

In this chapter, we studied the use of an extended Kalman filter in the trajectory calculation using IMU data. In particular, a novel application of the Kalman filter was introduced in which external magnets were used along the path and magnetic field magnitude was used as a reference signal. The mathematical model was constructed, and the imitation experiment was used to validate the EKF algorithm.

As shown in Table 7.2, the position error is much smaller when the Kalman filter is applied. As a consequence, the noisy acceleration signal is filtered when Kalman filter is applied. The effect of EKF is significant.

8.0 CONCLUSION AND DISCUSSION

This thesis set out to solve the problem of better understanding particle flow kinematics in pneumatic conveying by using IMUs as a low cost and convenient method compared with other methods. However, the IMU is composed of dead-reckoning sensors, which means that errors will accumulate in their results with time. It is necessary to find a compensation method to mitigate or eliminate the error.

In this paper, we introduced a new trajectory reconstruction algorithm. The new Kalman filter algorithm mitigates the errors that appear in the IMU's trajectory from the base algorithm. Its effect is repeatable, and it shows in the global acceleration plots that the noise of acceleration is diminished. The unrealistic inverse peaks are almost gone. The function of this algorithm is significant in reducing errors.

However, there are some limitations of this study.

1. The size of IMU is much bigger than the particle, and the density of the IMU is higher than that of the particles as well. This will cause inaccuracy when we try to speculate on the particle's motion from IMU.
2. The extended Kalman filter has limitation when the system is highly nonlinear, and the approximation might not be good enough.

The first limitation can be solved only when technology is advanced enough. When the manufacturing level advances to the point where the size of the IMU can be shrunk to the same as

the particles, we can better use the algorithm to detect particle movement during pneumatic conveying.

The second limitation can be solved by using another estimation technique called the unscented Kalman filter (UKF), or another nonlinear state estimator based on a very similar principle called the particle filter (PF). These may be effective, however, their computational cost will grow compared to the Kalman filter method presented here.

APPENDIX

CALIBRATION OF INERTIAL MEASUREMENT UNIT

Although commercial IMUs are calibrated before they leave the factory, it is important for re-calibration to be done before they are used in the lab because the bias of the sensors may change over time, and the environment may influence the result as well. For example, the environmental temperature and moisture may have an effect on the bias and drift of a gyroscope (M. Zhang, 2014).

The calibration method for each sensor in this paper is presented below.

A.1 CALIBRATION OF ACCELEROMETER

As mentioned in previous section, the bias and other effects of accelerometer will cause error in our trajectory reconstruction result. In this work, we provide a novel way to calibrate the accelerometer, which uses gravitational acceleration as a reference. First of all, we define the measurement model.

The accelerometer is a triplet of sensors with perpendicular sensitivity axes. As mentioned in Eq. 4.1, the output can be defined as in the following equation.

$$\begin{bmatrix} a_x^{imu} \\ a_y^{imu} \\ a_z^{imu} \end{bmatrix} = S^a \cdot A^a \cdot \left(\begin{bmatrix} a_x^{true} \\ a_y^{true} \\ a_z^{true} \end{bmatrix} + \begin{bmatrix} b_x^a \\ b_y^a \\ b_z^a \end{bmatrix} + N + D(t) \right) \quad \textbf{(A-1)}$$

where $[a_x^{imu}, a_y^{imu}, a_z^{imu}]^{\mathrm{T}}$ is the raw data obtained from IMU (m/s^2); S^a is the scale matrix, which is used to correct the sensitivity error; A^a is the effect of misalignment; $[a_x^{true}, a_y^{true}, a_z^{true}]^{\mathrm{T}}$ is the true acceleration; $[b_x^a, b_y^a, b_z^a]^{\mathrm{T}}$ is the bias vector; N is the noise vector; $D(t)$ is the drift function for time. The accelerometer calibration involves finding the scale matrix, misalignment effect and bias vector so that true acceleration can be found for any measurement.

We use a spherical motion fit to calibrate the triple-axis accelerometer. The theory behind this method is explained as follows. When the IMU is motionless, the only force applied on the accelerometer is gravity force, and no matter what attitude the IMU is in, the force is the same. That means that rotating the IMU to many different attitudes and plotting all the magnitudes (of the three orthogonal components) will ideally produce a sphere whose radius is the magnitude of gravitational acceleration. In reality, the actual plot of all of the measured vectors is not spherical, so the difference in radius from 1 g is sensitivity error and the offset of the center of the approximate sphere is the bias. The device we use is shown in Fig. A.1. The frame of the structure is designed to obtain rotation about three orthogonal axes by inserting the IMU in three different orientations as shown in Fig. A.1. The stepper motor is connected with a frame, and the IMU can be mounted in the frame. With this device, the IMU can only rotate about three perpendicular axes (i.e. no translation). An example of plotted data is shown in Fig. A.2. The bias $[b_x^a, b_y^a, b_z^a]^{\mathrm{T}} = [0.0345, 0.0528, 0.0301]^{\mathrm{T}}$. The $S^a \cdot A^a$ term is presented as matrix Ψ_a, which is found by an optimization method. Because the IMU is rotated 360° about three mutually perpendicular axes successively, the vector from the center of the sphere to the rotation result (red

dot in Fig. A.2) of each axis is supposed to be perpendicular as well. The cost function is defined as follows:

$$C(\boldsymbol{V}) = \sum_{\mathrm{i=1,j=1}}^{n} V_x(\mathrm{i}) \times V_y(\mathrm{j}) + \sum_{\mathrm{i=1,j=1}} V_x(\mathrm{i}) \times V_z(\mathrm{j}) + \sum_{\mathrm{i=1,j=1}}^{n} V_y(\mathrm{i}) \times V_z(\mathrm{j}) \quad \textbf{(A-2)}$$

where, for example, $V_x(\mathrm{i})$ is the i$^{\mathrm{th}}$ vector, which points from the sphere center to the i$^{\mathrm{th}}$ result as it rotates about X axis; and n is the number of data points. By bounding the cost function $\|C(\boldsymbol{V})\| \leq 0.001$, Ψ_a is solved to be $\begin{bmatrix} 0.9993 & -0.0115 & -0.0037 \\ 0.0122 & 0.9999 & 0.0077 \\ 0.0080 & -0.0008 & 1.0000 \end{bmatrix}$.

The temperature and other environmental factors have little effect on accelerometer, so the accelerometer is only calibrated at the beginning of each day's experiments.

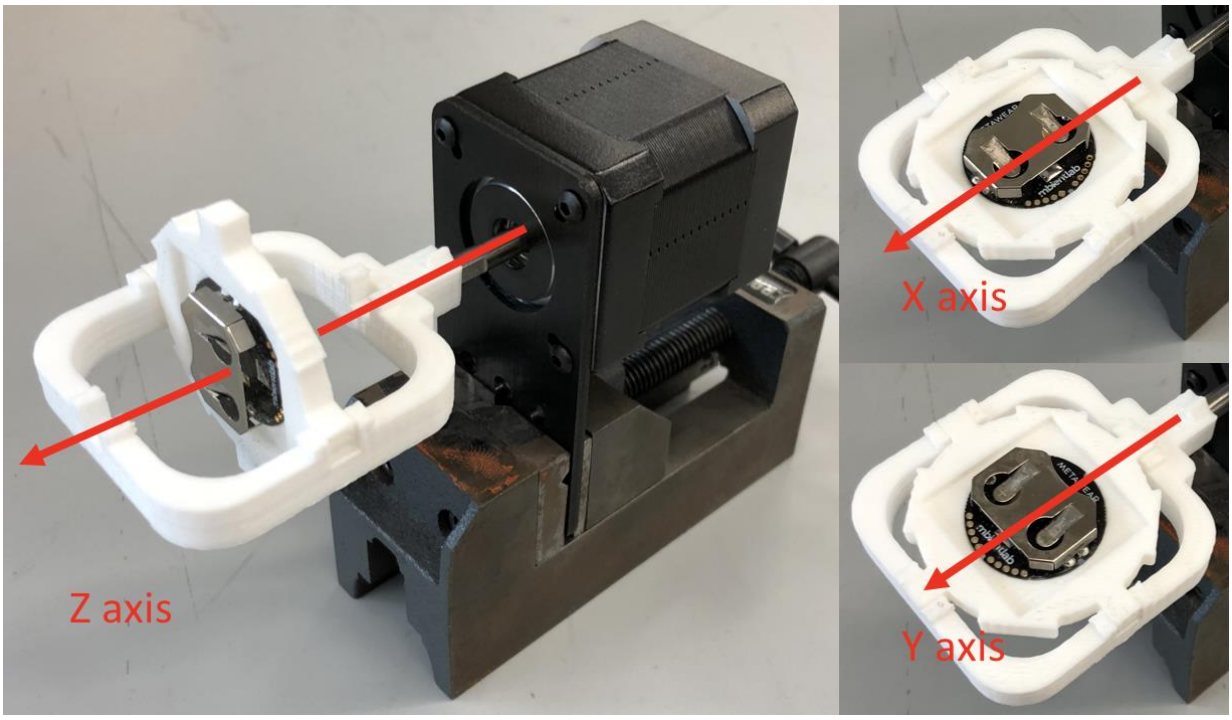

Fig. A.1 The device used to calibrate the accelerometer by inserting the IMU in three different orientations to obtain rotation about orthogonal axes.

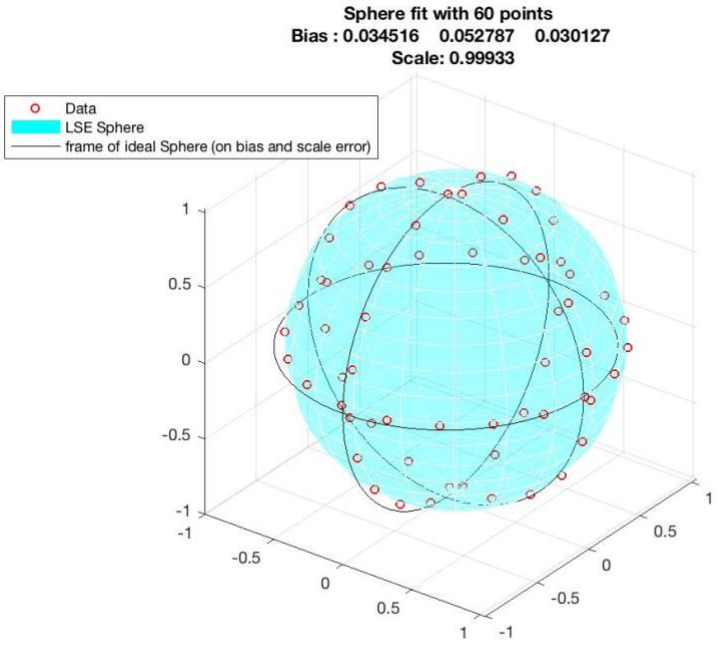

Fig. A.2 The sphere fit. The red dots are raw acceleration data;

the blue surface is fitted sphere surface.

A.2 CALIBRATION OF GYROSCOPE

The gyroscope provides a triplet of sensors with perpendicular sensitivity axes. A mathematical model of the sensor output is defined as in the follow equation, which is an expanded version of Eq. (4-2).

$$\begin{bmatrix} w_x^{imu} \\ w_y^{imu} \\ w_z^{imu} \end{bmatrix} = S^g \cdot A^g \cdot \left(\begin{bmatrix} w_x^{true} \\ w_y^{true} \\ w_z^{true} \end{bmatrix} + \begin{bmatrix} b_x \\ b_z \\ b_z \end{bmatrix} + N + D(t) \right) \tag{A-3}$$

where $[w_x^{imu}, w_y^{imu}, w_z^{imu}]^{\mathrm{T}}$ is the raw data obtained from the IMU (deg/s); S^g is the scale matrix; A^g is the effect of misalignment; $[w_x^{true}, w_y^{true}, w_z^{true}]^{\mathrm{T}}$ is the true angular velocity; $[b_x^g, b_y^g, b_z^g]^{\mathrm{T}}$

is the bias vector; N is the noise vector; $D(t)$ is the drift function for time. For the commercial IMUs that we are using, after the bias of the gyroscope is calibrated, the result of higher speed rotation is found to have almost no error, as shown in Fig. A.3. The IMU is mounted on the same device shown in Fig. A.1, and is rotated about three orthogonal axes, creating 20 circles at constant speed of 682 deg/s. As shown in Fig A.3a, Fig A.3c and Fig A.3d, the angular velocities are close to 682 deg/s. The total rotation angle is about 7,200 deg for each test (360 deg x 20 rotations). This suggests that the product of $S^g \cdot A^g$ is close to the identity matrix, the Eq. A.2 can be simplified as Eq. A.3. The calibration focuses on finding the bias vector.

$$\begin{bmatrix} w_x^{imu} \\ w_y^{imu} \\ w_z^{imu} \end{bmatrix} = \begin{bmatrix} w_x^{true} \\ w_y^{true} \\ w_z^{true} \end{bmatrix} + \begin{bmatrix} b_x \\ b_z \\ b_z \end{bmatrix} + N + D(t) \quad \textbf{(A-4)}$$

When an IMU is motionless, the angular velocity on each axis is zero, so the measured values should be zero as well. The bias is defined as the mean value of motionless raw gyroscope data.

The gyroscope is calibrated before every experiment.

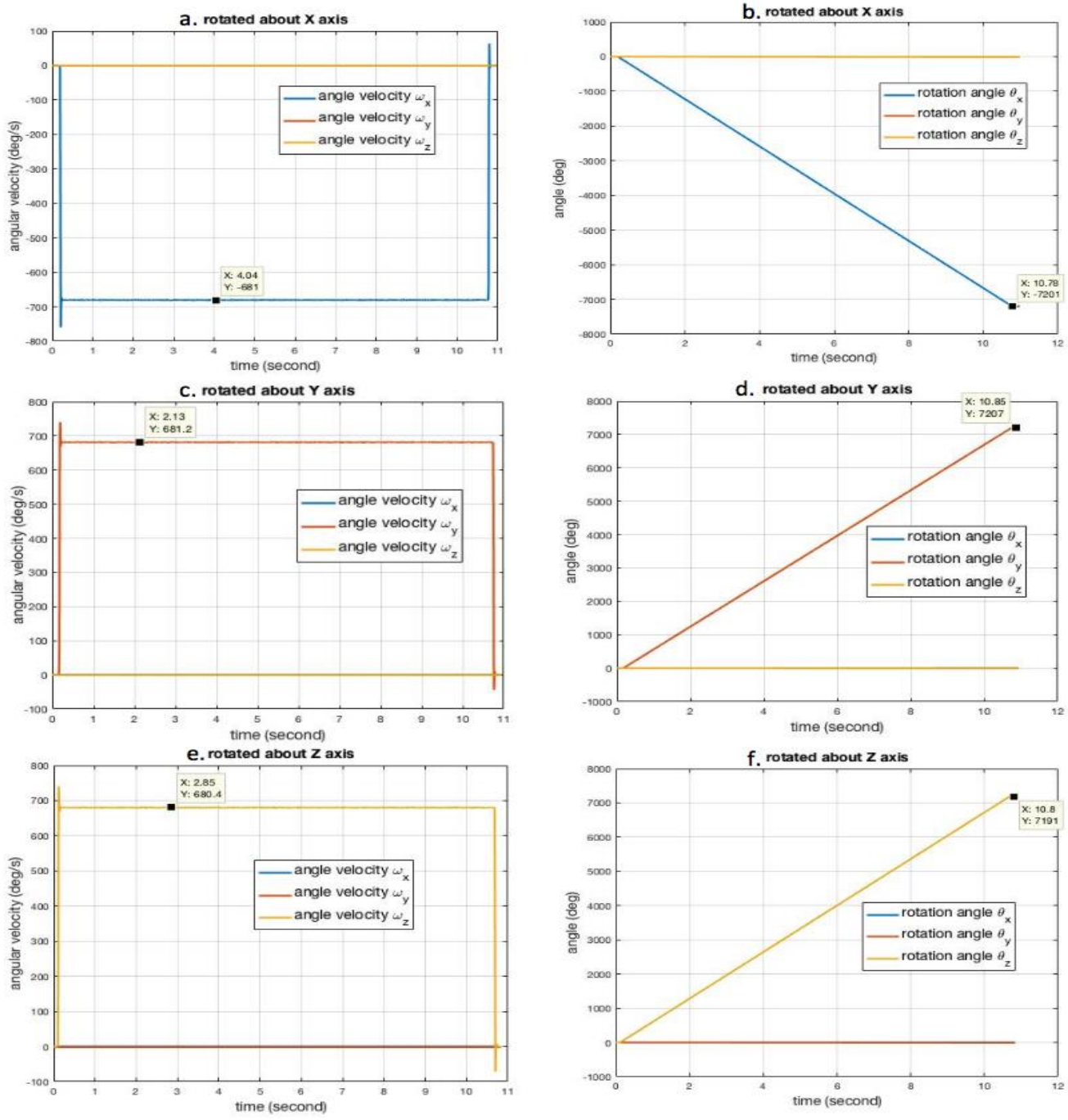

Fig. A.3 The result of angular velocities and rotation angles about each axis during individual axes rotations.

a. Angular velocities when rotated about X axis; b. Rotation angles when rotated about X axis;

c. Angular velocities when rotated about Y axis; d. Rotation angles when rotated about Y axis;

e. Angular velocities when rotated about Z axis; f. Rotation angles when rotated about Z axis.

A.3 CALIBRATION OF MAGNETOMETER

The way we use the magnetometer dictates the way we calibrate it. The function of the magnetometer in this study is to find the strength of magnetic field instead its direction (that is, the magnitude of the magnetometer vector is important and not necessarily the values of any given axis). The model is defined as shown in the following equation.

$$\begin{bmatrix} h_x^{imu} \\ h_y^{imu} \\ h_z^{imu} \end{bmatrix} = S^h \cdot \left(\begin{bmatrix} h_x^{true} \\ h_y^{true} \\ h_z^{true} \end{bmatrix} + \begin{bmatrix} b_x \\ b_z \\ b_z \end{bmatrix} + N \right) \quad \textbf{(A-5)}$$

where $[h_x^{imu}, h_y^{imu}, h_z^{imu}]^{\mathrm{T}}$ is the raw data obtained from the magnetometer in the IMU (T); S^h is the scale matrix, which is used to correct the sensitivity error; $[h_x^{true}, h_y^{true}, h_z^{true}]^{\mathrm{T}}$ is the true angular velocity; $[b_x^h, b_y^h, b_z^h]^{\mathrm{T}}$ is the bias vector; and N is the noise vector.

The calibration method for the magnetometer is similar to that for the accelerometer. However, because the magnetometer is not working by inertial effects, the calibration is simpler. Before the experiment, the magnetometer is calibrated. The IMU is rotated arbitrarily by hand at the starting point. In order to get the best calibration result, there are two critical things that should be noticed. First, the duration of the manual rotation should be more than 40 seconds to collect 1,000 sample points for statistical purpose; second, the IMU is rotated about the start point and each magnetometer axis should cover as much orientation as possible. During the calibration procedure, an iterative batch Least Squares Error (LSE) calculation is used to estimate the deviation and the combined scale factors of the sensor. An example result is shown in Fig. A.4. The bias is the offset of the center of the sphere from the origin; and the diameter of the sphere is the strength of magnetic field, which will be normalized to 1 eventually.

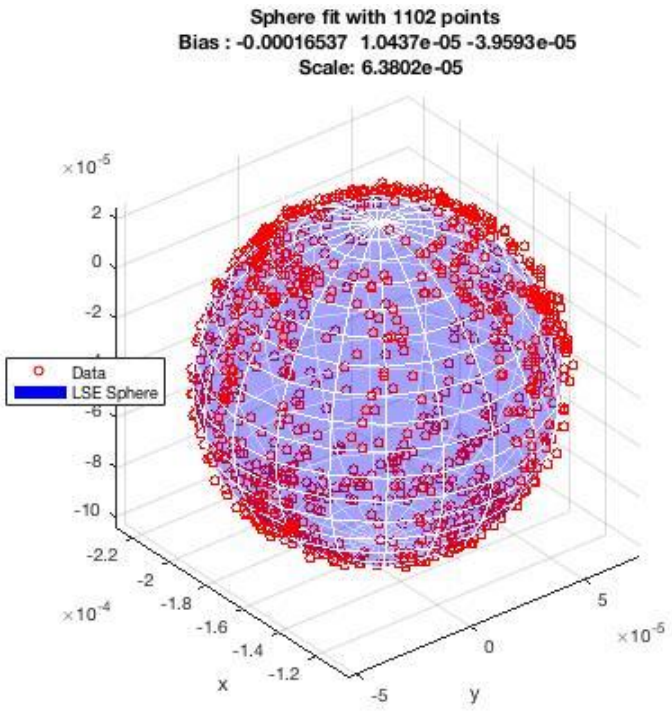

Fig. A.4 The sphere fit result. Each red dot is the raw data from the magnetometer; the blue surface is LSE sphere surface.

Summary

This chapter introduced the calibration method of each sensor used in this paper. Based on the role of each sensor, dominant parameters are taken into account for the sake of simplifying the calibration procedure. Before calibration, sensors are turned on for 10 minutes to pre-heat. The accelerometer and magnetometer were calibrated before the first trial of the day when experiments are planned to conduct; and the gyroscope was calibrated before every trial.

REFERENCE

Acar, C., & Shkel, A. M. (2003). Experimental evaluation and comparative analysis of commercial variable-capacitance {MEMS} accelerometers. *J Micromech Microengineering*, *13*(5), 634–645. https://doi.org/10.1088/0960-1317/13/5/315

Achtelik, M., Kuhnlenz, K., & Buss, M. (2009). Visual tracking and control of a quadcopter using a stereo camera system and inertial sensors. *2009 International Conference on Mechatronics and Automation*, (May 2014), 2863–2869. https://doi.org/10.1109/ICMA.2009.5246421

Caron, F., Duflos, E., Pomorski, D., & Vanheeghe, P. (2006). GPS/IMU data fusion using multisensor Kalman filtering: Introduction of contextual aspects. *Information Fusion*, *7*(2), 221–230. https://doi.org/10.1016/j.inffus.2004.07.002

Chong, S., Rui, S., Jie, L., Xiaoming, Z., Jun, T., Yunbo, S., … Huiliang, C. (2016). Temperature drift modeling of MEMS gyroscope based on genetic-Elman neural network. *Mechanical Systems and Signal Processing*, *72–73*, 897–905. https://doi.org/10.1016/j.ymssp.2015.11.004

Dam, E. B., Koch, M., & Lillholm, M. (1998). Quaternions , Interpolation and Animation. *Technical Report DIKU-TR-98/5*, 103. https://doi.org/Technical Report DIKU-TR-98/5

Fakharian, A., Gustafsson, T., & Mehrfam, M. (2011). Adaptive Kalman filtering based navigation: an IMU/GPS integration approach. *Networking, Sensing and …*, (April), 11–13. https://doi.org/10.1109/ICNSC.2011.5874871

Hou, H., & El-Sheimy, N. (2004). Modeling Inertial Sensors Errors Using Allan Variance. *Department of Geomatics Engineering*, *MSc*(UCGE Reports Number 20201), 147.

Klinzing, G. E. (2018). Historical Review of Pneumatic Conveying. *KONA Powder and Particle Journal*, (July), 1–10. https://doi.org/10.14356/kona.2018010

Klinzing, G. E., Rizk, F., Marcus, R., & Leung, L. S. (2010). *Pneumatic Conveying of Solids* (Vol. 8). https://doi.org/10.1007/978-90-481-3609-4

Krishnaswami, G. S., & Sachdev, S. (2016). Algebra and geometry of Hamilton's quaternions, *1*, 1–11. Retrieved from http://arxiv.org/abs/1606.03315

Kuipers, J. B. (1999). *Quaternions and rotation sequences : a primer with applications to orbits, aerospace, and virtual reality*. Princeton, N.J: Princeton University Press.

Leland, R. P. (2005). Mechanical-thermal noise in MEMS gyroscopes. *IEEE Sensors Journal*, *5*(3), 493–500. https://doi.org/10.1109/JSEN.2005.844538

Lemkin, M., & Boser, B. E. (1999). Three-axis micromachined accelerometer with a CMOS position-sense interface and digital offset-trim electronics. *IEEE Journal of Solid-State Circuits*, *34*(4), 456–468. https://doi.org/10.1109/4.753678

Lotters, J. C., Schipper, J., Veltink, P. H., Olthuis, W., & Bergveld, P. (1998). Procedure for in-use calibration of triaxial accelerometers in medical applications. *Sensors and Actuators, A: Physical*, *68*(1–3 pt 2), 221–228. https://doi.org/10.1016/S0924-4247(98)00049-1

Luding, S. (2008). Introduction to discrete element methods: Basic of contact force models and how to perform the micro-macro transition to continuum theory. *European Journal of Environmental and Civil Engineering*, *12*(7–8), 785–826. https://doi.org/10.1080/19648189.2008.9693050

Matsumoto, S., & Saito, S. (1970). On the mechanism of suspension of particles in horizontal pneumatic conveying: Monte carlo simulation based on the irregular bouncing model. *JOURNAL of CHEMICAL ENGINEERING of JAPAN*, *3*(1), 83–92. https://doi.org/10.1252/jcej.3.83

Miller, D., Baimbridge, P., & Eyre, D. (2000). *TECHNOLOGY STATUS REVIEW OF PF FLOW MEASUREMENT AND CONTROL METHODS FOR UTILITY BOILERS*.

Mills, D., Jones, M. G., & Agarwal, V. K. (2004). *Handbook of pneumatic conveying engineering*. *Mechanical Engineering*. https://doi.org/10.1201/9780203021989

Mirzaei, F. M., & Roumeliotis, S. I. (2008). A Kalman-filter-based algorithm for IMU-camera calibration: observability analysis and performance evaluation. . *IEEE Trans. Robot.* , *24*(5), 1143–1156. https://doi.org/10.1109/TRO.2008.2004486

Patterson, J. (2007). The effects of nurse to patient ratios. *Nursing Times*, *107*(2), 22–25. https://doi.org/10.1111/jan.12325

Renaudin, V., Afzal, M. H., & Lachapelle, G. (2010). Complete triaxis magnetometer calibration in the magnetic domain. *Journal of Sensors*, *2010*. https://doi.org/10.1155/2010/967245

Sa, I., & Corke, P. (2012). System identification, estimation and control for a cost effective open-source quadcopter. *Proceedings - IEEE International Conference on Robotics and Automation*, 2202–2209. https://doi.org/10.1109/ICRA.2012.6224896

Sabatini, A. M., & Member, S. (2006). Quaternion-based extended kalman filter for determination orientation by inertial and magnetic sensing - Google Search, *53*(7), 1346–1356. Retrieved from https://www.google.ch/webhp?sourceid=chrome-instant&ion=1&espv=2&ie=UTF-8#q=Quaternion-based+extended+kalman+filter+for+determination+orientation+by+inertial+and+magnetic+sensing

Touil, K., Zribi, M., Choquel, J. B., & Benjelloun, M. (2007). Bayesian bootstrap filter for integrated GPS and dead reckoning positioning. *IEEE International Symposium on Industrial Electronics*, (1), 1520–1524. https://doi.org/10.1109/ISIE.2007.4374828

Tsai, M., Liu, Y., & Fang, W. (2012). A Three-Axis CMOS-MEMS Accelerometer StructureWith Vertically Integrated Fully Differential Sensing Electrodes, *21*(6), 1329–1337.

Tsuji, Y., Tanaka, T., & Ishida, T. (1992). Lagrangian simulation of plug flow of collisionless particles in a horizontal pipe. *Powder Tech.*, *71*, 239–250.

Variance, A., El-sheimy, N., Hou, H., & Niu, X. (2015). Analysis and Modeling of Inertial Sensors Using Analysis and Modeling of Inertial Sensors Using Allan Variance, *57*(August), 140–149. https://doi.org/10.1109/TIM.2007.908635

Wang, C., Zhang, J., Zheng, W., Gao, W., & Jia, L. (2017). Signal decoupling and analysis from inner flush-mounted electrostatic sensor for detecting pneumatic conveying particles. *Powder Technology*, *305*, 197–205. https://doi.org/10.1016/j.powtec.2016.09.081

Wang, J. S., Hsu, Y. L., & Liu, J. N. (2010). An inertial-measurement-unit-based pen with a trajectory reconstruction algorithm and its applications. *IEEE Transactions on Industrial Electronics*, *57*(10), 3508–3521. https://doi.org/10.1109/TIE.2009.2038339

Welch, G., & Bishop, G. (2006). An Introduction to the Kalman Filter. *In Practice*, *7*(1), 1–16. https://doi.org/10.1.1.117.6808

Won, S. H. P., Golnaraghi, F., & Melek, W. W. (2009). A fastening tool tracking system using an IMU and a position sensor with Kalman filters and a fuzzy expert system. *IEEE Transactions on Industrial Electronics*, *56*(5), 1782–1792. https://doi.org/10.1109/TIE.2008.2010166

Won, S., Melek, W., & Golnaraghi, F. (2010). A Kalmanparticle filter-based position and orientation estimation method using a position sensor inertial Measurement unit Hybrid System. *IEEE Transaction on Industrial Electronics*, *57*(5), 1787–1798.

Xiang, J., & McGlinchey, D. (2004). Numerical simulation of particle motion in dense phase pneumatic conveying. *Granular Matter*, *6*(2–3), 167–172. https://doi.org/10.1007/s10035-004-0161-2

Xie, H., & Fedder, G. K. (2002). Fabrication, Characterization, and Analysis of a DRIE CMOS-MEMS Gyroscope. *Proceedings of IEEE Sensors*, *1*(2), 1413–1418. Retrieved from http://www.scopus.com/inward/record.url?eid=2-s2.0-1542271323&partnerID=tZOtx3y1

Yan, F., & Rinoshika, A. (2011). Application of high-speed PIV and image processing to measuring particle velocity and concentration in a horizontal pneumatic conveying with dune model. *Powder Technology*, *208*(1), 158–165. https://doi.org/10.1016/j.powtec.2010.12.014

Yan, Y. (1996). Mass flow measurement of bulk solids in pneumatic pipelines. *Measurement Science and Technology*, *7*(12), 1687–1706. https://doi.org/10.1088/0957-0233/7/12/002

Yang, H. H., Myung, N. V., Yee, J., Park, D. Y., Yoo, B. Y., Schwartz, M., … Judy, J. W. (2002). Ferromagnetic micromechanical magnetometer. *Sensors and Actuators, A: Physical*, *97–98*, 88–97. https://doi.org/10.1016/S0924-4247(01)00809-3

Zhang, M. (2014). *MULTI-SENSOR INERTIAL MEASUREMENT SYSTEM FOR ANALYSIS OF SPORTS MOTION*. University of Pittsburgh.

Zhang, M. (2015). Multi-Sensor Inertial Measurements System for Analysis of Sports Motion, 121. Retrieved from http://d-scholarship.pitt.edu/id/eprint/22664

Zhang, P., Gu, J., Milios, E. E., & Huynh, P. (2005). Navigation with IMU/GPS/digital compass with unscented Kalman filter. *IEEE International Conference Mechatronics and Automation, 2005*, *3*(July), 1497–1502. https://doi.org/10.1109/ICMA.2005.1626777

Zheng, Y., & Rinoshika, A. (2017). Analysis of particle dynamics in a horizontal pneumatic conveying of the minimum pressure drop based on POD and wavelet transform. *Powder Technology*, *320*, 726–738. https://doi.org/10.1016/j.powtec.2017.07.092

Acar, C., & Shkel, A. M. (2003). Experimental evaluation and comparative analysis of commercial variable-capacitance {MEMS} accelerometers. *J Micromech Microengineering*, *13*(5), 634–645. https://doi.org/10.1088/0960-1317/13/5/315

Achtelik, M., Kuhnlenz, K., & Buss, M. (2009). Visual tracking and control of a quadcopter using a stereo camera system and inertial sensors. *2009 International Conference on Mechatronics and Automation*, (May 2014), 2863–2869. https://doi.org/10.1109/ICMA.2009.5246421

Caron, F., Duflos, E., Pomorski, D., & Vanheeghe, P. (2006). GPS/IMU data fusion using multisensor Kalman filtering: Introduction of contextual aspects. *Information Fusion*, *7*(2), 221–230. https://doi.org/10.1016/j.inffus.2004.07.002

Chong, S., Rui, S., Jie, L., Xiaoming, Z., Jun, T., Yunbo, S., … Huiliang, C. (2016). Temperature drift modeling of MEMS gyroscope based on genetic-Elman neural network. *Mechanical Systems and Signal Processing*, *72–73*, 897–905. https://doi.org/10.1016/j.ymssp.2015.11.004

Dam, E. B., Koch, M., & Lillholm, M. (1998). Quaternions , Interpolation and Animation. *Technical Report DIKU-TR-98/5*, 103. https://doi.org/Technical Report DIKU-TR-98/5

Fakharian, A., Gustafsson, T., & Mehrfam, M. (2011). Adaptive Kalman filtering based navigation: an IMU/GPS integration approach. *Networking, Sensing and …*, (April), 11–13. https://doi.org/10.1109/ICNSC.2011.5874871

Hou, H., & El-Sheimy, N. (2004). Modeling Inertial Sensors Errors Using Allan Variance. *Department of Geomatics Engineering*, *MSc*(UCGE Reports Number 20201), 147.

Klinzing, G. E. (2018). Historical Review of Pneumatic Conveying. *KONA Powder and Particle Journal*, (July), 1–10. https://doi.org/10.14356/kona.2018010

Klinzing, G. E., Rizk, F., Marcus, R., & Leung, L. S. (2010). *Pneumatic Conveying of Solids* (Vol. 8). https://doi.org/10.1007/978-90-481-3609-4

Krishnaswami, G. S., & Sachdev, S. (2016). Algebra and geometry of Hamilton's quaternions, *1*, 1–11. Retrieved from http://arxiv.org/abs/1606.03315

Kuipers, J. B. (1999). *Quaternions and rotation sequences : a primer with applications to orbits, aerospace, and virtual reality*. Princeton, N.J: Princeton University Press.

Leland, R. P. (2005). Mechanical-thermal noise in MEMS gyroscopes. *IEEE Sensors Journal*, *5*(3), 493–500. https://doi.org/10.1109/JSEN.2005.844538

Lemkin, M., & Boser, B. E. (1999). Three-axis micromachined accelerometer with a CMOS position-sense interface and digital offset-trim electronics. *IEEE Journal of Solid-State Circuits*, *34*(4), 456–468. https://doi.org/10.1109/4.753678

Lotters, J. C., Schipper, J., Veltink, P. H., Olthuis, W., & Bergveld, P. (1998). Procedure for in-use calibration of triaxial accelerometers in medical applications. *Sensors and Actuators, A: Physical*, *68*(1–3 pt 2), 221–228. https://doi.org/10.1016/S0924-4247(98)00049-1

Luding, S. (2008). Introduction to discrete element methods: Basic of contact force models and how to perform the micro-macro transition to continuum theory. *European Journal of Environmental and Civil Engineering*, *12*(7–8), 785–826. https://doi.org/10.1080/19648189.2008.9693050

Matsumoto, S., & Saito, S. (1970). On the mechanism of suspension of particles in horizontal pneumatic conveying: Monte carlo simulation based on the irregular bouncing model. *JOURNAL of CHEMICAL ENGINEERING of JAPAN*, *3*(1), 83–92. https://doi.org/10.1252/jcej.3.83

Miller, D., Baimbridge, P., & Eyre, D. (2000). *TECHNOLOGY STATUS REVIEW OF PF FLOW MEASUREMENT AND CONTROL METHODS FOR UTILITY BOILERS*.

Mills, D., Jones, M. G., & Agarwal, V. K. (2004). *Handbook of pneumatic conveying engineering*. *Mechanical Engineering*. https://doi.org/10.1201/9780203021989

Mirzaei, F. M., & Roumeliotis, S. I. (2008). A Kalman-filter-based algorithm for IMU-camera calibration: observability analysis and performance evaluation. . *IEEE Trans. Robot.* , *24*(5), 1143–1156. https://doi.org/10.1109/TRO.2008.2004486

Patterson, J. (2007). The effects of nurse to patient ratios. *Nursing Times*, *107*(2), 22–25. https://doi.org/10.1111/jan.12325

Renaudin, V., Afzal, M. H., & Lachapelle, G. (2010). Complete triaxis magnetometer calibration in the magnetic domain. *Journal of Sensors*, *2010*. https://doi.org/10.1155/2010/967245

Sa, I., & Corke, P. (2012). System identification, estimation and control for a cost effective open-source quadcopter. *Proceedings - IEEE International Conference on Robotics and Automation*, 2202–2209. https://doi.org/10.1109/ICRA.2012.6224896

Sabatini, A. M., & Member, S. (2006). Quaternion-based extended kalman filter for determination orientation by inertial and magnetic sensing - Google Search, *53*(7), 1346–1356. Retrieved from https://www.google.ch/webhp?sourceid=chrome-instant&ion=1&espv=2&ie=UTF-8#q=Quaternion-based+extended+kalman+filter+for+determination+orientation+by+inertial+and+magnetic+sensing

Touil, K., Zribi, M., Choquel, J. B., & Benjelloun, M. (2007). Bayesian bootstrap filter for integrated GPS and dead reckoning positioning. *IEEE International Symposium on Industrial Electronics*, (1), 1520–1524. https://doi.org/10.1109/ISIE.2007.4374828

Tsai, M., Liu, Y., & Fang, W. (2012). A Three-Axis CMOS-MEMS Accelerometer StructureWith Vertically Integrated Fully Differential Sensing Electrodes, *21*(6), 1329–1337.

Tsuji, Y., Tanaka, T., & Ishida, T. (1992). Lagrangian simulation of plug flow of collisionless particles in a horizontal pipe. *Powder Tech.*, *71*, 239–250.

Variance, A., El-sheimy, N., Hou, H., & Niu, X. (2015). Analysis and Modeling of Inertial Sensors Using Analysis and Modeling of Inertial Sensors Using Allan Variance, *57*(August), 140–149. https://doi.org/10.1109/TIM.2007.908635

Wang, C., Zhang, J., Zheng, W., Gao, W., & Jia, L. (2017). Signal decoupling and analysis from inner flush-mounted electrostatic sensor for detecting pneumatic conveying particles. *Powder Technology*, *305*, 197–205. https://doi.org/10.1016/j.powtec.2016.09.081

Wang, J. S., Hsu, Y. L., & Liu, J. N. (2010). An inertial-measurement-unit-based pen with a trajectory reconstruction algorithm and its applications. *IEEE Transactions on Industrial Electronics*, *57*(10), 3508–3521. https://doi.org/10.1109/TIE.2009.2038339

Welch, G., & Bishop, G. (2006). An Introduction to the Kalman Filter. *In Practice*, *7*(1), 1–16. https://doi.org/10.1.1.117.6808

Won, S. H. P., Golnaraghi, F., & Melek, W. W. (2009). A fastening tool tracking system using an IMU and a position sensor with Kalman filters and a fuzzy expert system. *IEEE Transactions on Industrial Electronics*, *56*(5), 1782–1792. https://doi.org/10.1109/TIE.2008.2010166

Won, S., Melek, W., & Golnaraghi, F. (2010). A Kalmanparticle filter-based position and orientation estimation method using a position sensor inertial Measurement unit Hybrid System. *IEEE Transaction on Industrial Electronics*, *57*(5), 1787–1798.

Xiang, J., & McGlinchey, D. (2004). Numerical simulation of particle motion in dense phase pneumatic conveying. *Granular Matter*, *6*(2–3), 167–172. https://doi.org/10.1007/s10035-004-0161-2

Xie, H., & Fedder, G. K. (2002). Fabrication, Characterization, and Analysis of a DRIE CMOS-MEMS Gyroscope. *Proceedings of IEEE Sensors*, *1*(2), 1413–1418. Retrieved from http://www.scopus.com/inward/record.url?eid=2-s2.0-1542271323&partnerID=tZOtx3y1

Yan, F., & Rinoshika, A. (2011). Application of high-speed PIV and image processing to measuring particle velocity and concentration in a horizontal pneumatic conveying with dune model. *Powder Technology*, *208*(1), 158–165. https://doi.org/10.1016/j.powtec.2010.12.014

Yan, Y. (1996). Mass flow measurement of bulk solids in pneumatic pipelines. *Measurement Science and Technology*, *7*(12), 1687–1706. https://doi.org/10.1088/0957-0233/7/12/002

Yang, H. H., Myung, N. V., Yee, J., Park, D. Y., Yoo, B. Y., Schwartz, M., … Judy, J. W. (2002). Ferromagnetic micromechanical magnetometer. *Sensors and Actuators, A: Physical*, *97–98*, 88–97. https://doi.org/10.1016/S0924-4247(01)00809-3

Zhang, M. (2014). *MULTI-SENSOR INERTIAL MEASUREMENT SYSTEM FOR ANALYSIS OF SPORTS MOTION*. University of Pittsburgh.

Zhang, M. (2015). Multi-Sensor Inertial Measurements System for Analysis of Sports Motion, 121. Retrieved from http://d-scholarship.pitt.edu/id/eprint/22664

Zhang, P., Gu, J., Milios, E. E., & Huynh, P. (2005). Navigation with IMU/GPS/digital compass with unscented Kalman filter. *IEEE International Conference Mechatronics and Automation, 2005*, *3*(July), 1497–1502. https://doi.org/10.1109/ICMA.2005.1626777

Zheng, Y., & Rinoshika, A. (2017). Analysis of particle dynamics in a horizontal pneumatic conveying of the minimum pressure drop based on POD and wavelet transform. *Powder Technology*, *320*, 726–738. https://doi.org/10.1016/j.powtec.2017.07.092